IN-SITU X-RAY MEASUREMENTS DURING PULSED LASER DEPOSITION OF COMPLEX OXIDE MATERIALS

by John David Ferguson Jr

IN-SITU X-RAY MEASUREMENTS DURING PULSED LASER DEPOSITION OF COMPLEX OXIDE MATERIALS

A Dissertation

Presented to the Faculty of the Graduate School

of Cornell University

in Partial Fulfillment of the Requirements for the Degree of

Doctor of Philosophy

by

John David Ferguson, Jr.

August 2010

IN-SITU X-RAY MEASUREMENTS DURING PULSED LASER DEPOSITION OF COMPLEX OXIDE MATERIALS

John David Ferguson, Jr., Ph.D.

Cornell University 2010

Complex Oxides possess a vast range of materials properties that will allow them to have a lasting impact on device architecture. To incorporated thin films of complex oxides into devices, a fundamental understanding of the mechanisms involved with thin film nucleation, growth, and interface formation must be achieved. For many complex oxide researchers, the deposition technique of choice is pulsed laser deposition (PLD). Our PLD chamber, installed at the G3 hutch in the Cornell High Energy Synchrotron Source, was specifically designed to study the growth kinetics during deposition. Chapter 1 of this thesis provides an introduction to complex oxide materials and pulsed laser deposition. Chapter 2 describes the x-ray scattering techniques used to study the thin film surface kinetics throughout this thesis.

Chapter 3 presents a novel, in situ, x-ray scattering study of the PLD of the prototypic system: homoepitaxial $SrTiO_3\langle 001\rangle$. The data provides a direct measurement of island nucleation, aggregation, and coarsening during PLD. Detailed analysis of these data lead to quantitative measurements of both in-plane and downhill diffusion. The same diffusion rate is found for these two processes, suggesting that the Ehrlich-Schwoebel barrier for downhill diffusion is negligible. This technique significantly increases the time resolution over other methods of

measuring surface diffusion, such as scanning tunneling microscopy.

In Chapter 4, we apply the methodology of Chapter 3 to a heteroepitaxial system: $LaAlO_3$ on $SrTiO_3\langle 001\rangle$. This materials system has received considerable attention in the literature due to the formation of a quasi-two-dimensional electron gas at the interface [1]. Conceptually, one might expect diffusion processes of the first monolayer, i.e. $LaAlO_3$ on $SrTiO_3$, to differ from those of subsequent monolayers that involve diffusion of $LaAlO_3$ constituents on the $LaAlO_3$ film. We therefore measure the activation energy for diffusion as a function of the number of heteroepitaxial monolayers deposited. We find that the activation barrier for in-plane diffusion of $LaAlO_3$ on $SrTiO_3$ is larger than that for downhill diffusion of $LaAlO_3$ to the $SrTiO_3$ substrate. Additionally, we show that the downhill diffusion barrier is further decreased after the second $LaAlO_3$ monolayer.

In Chapter 5 we use in situ x-ray diffraction in a different configuration: as a probe to detect phase transformations at burred films. This chapter reports on the discovery of a new method to form brownmillerite structures in thin films of four different manganite materials: $La_{0.7}Sr_{0.3}MnO_3$, $Pr_{0.7}Ca_{0.3}MnO_3$, $La_{0.7}Ca_{0.3}MnO_3$, and $LaMnO_3$. These pseudomorphic, single crystal brownmillerite films form epitaxially on the most commonly used complex oxide substrate, $SrTiO_3\langle 001\rangle$. The method involves the epitaxial deposition of an oxygen getter material ($SrTiO_{3-\delta}$ or $LaAlO_{3-\delta}$) on the manganite film. The getter layer removes oxygen from the buried manganite film, and when a critical thickness is reached, the buried manganite film phase transforms into an ordered brownmillerite structure. A provisional patent was provided for this technique[1]. Chapter 6 provides the closing remarks, as well as suggesting future directions for the PLD/ x-ray diffraction experiment.

[1] "Epitaxial Getter Layer for a Complex Oxide Brownmillerite Phase Transformation in Maganite Films." U.S. Patent Application #6129690 (2010)

BIOGRAPHICAL SKETCH

John David Ferguson, Jr. was born on October 17, 1980 to JoAnne and John Ferguson. He spent most of his childhood in Raleigh, NC. As an elementary school student, he showed interest in science by competing in multiple science fairs at Lynn Road Elementary. In fourth grade he won second place in this competition with his project on soil erosion. In high school, John showed little motivation for academic success, except in the field of mathematics. The majority of his interest was in cooking, where he believed his career would lead him. Without having sufficient grades to apply to college, John enrolled in a co-op program at Leesville High School. In this program, he spent his mornings at high school and left early to work at a restaurant in downtown Raleigh. After about a year of this, John realized that he no longer desired to be a chef, and decided to move to the beautiful mountain town of Boone, NC.

In Boone, John enrolled at Caldwell Community College and began taking standard classes to transfer to a four year university. He quickly remembered why he did not enjoy academics and, in his third semester, he enrolled in only two classes: World History and Calculus. In his calculus class, John recognized his passion for mathematics, and decided to transfer to Appalachian State University as a mathematics major. At Appalachian State, where he enrolled in up to three math classes at once, his academic advisor recommended that he take a course in physics. The next semester he enrolled in non-calculus physics and quickly discovered that everything he loved about math could readily be applied to explain the world around him. He immediately decided to double major in math and physics, without much regard for what he would do after college.

During his third year, John took two materials science and engineering courses and found that he had a great interest in that field. The professor of these two classes convinced him to apply to graduate school, and in the fall of 2005, John enrolled in the Department of Materials Science and Engineering at Cornell University as a Ph.D. graduate student. At Cornell, John joined the research group of Professor Joel Brock. John's research at Cornell was highly centralized at the Cornell High Energy Synchrotron Source, where he was responsible for the maintenance of, experimental upgrades to, and performing experiments in the G3 hutch.

For my mother and father who believed in me

through all of the tough times.

Your love and dedication made me who I am.

ACKNOWLEDGEMENTS

The research shown throughout this thesis is a direct result of the collaboration between many individuals. First, I would like to thank my advisor, Professor Joel Brock, for offering me a position in his research group and providing any financial support. Over the years he has taught me many invaluable lessons about how to perform research. Additionally, he gave me a research project that allowed me to exploit my passion for designing, building, maintaining, and implementing the various types of the equipment in the G3 hutch at the Cornell High Energy Synchrotron Source (CHESS). In particular, I am grateful for his encouragement and support for me to attend and present my work at many scientific conferences.

I cannot adequately express the gratitude that I have towards Gline staff scientist, Dr. Arthur Woll. His ability to be patient with me while I was learning the physics of x-ray scattering, thin film growth, and instrumentation was unmeasurably helpful. This research project would not be where it is today without his collaboration. I would also like to thank CHESS staff scientist, Dr. Darren Dale. Darren was my graduate student advisor when I was a summer undergraduate researcher at Cornell. He is one of the main reasons I came to Cornell, and his help over the years is greatly appreciated.

The unique ability of having access to all of the expertise available at CHESS contributed greatly to the success of this project. Over the years, I have developed an excellent relationship with the majority of the CHESS staff. Specifically, I would like to thank all of the CHESS machinists: Jerry Houghton, John Kopsa, and Walt Protas. Additionally, the expertise of Bob Seeley in the area of ultra-high vacuum systems is greatly appreciated. I would also like to thank Ted Luddy for giving me help with all of the electronics I have had to design and build over

the years. Next, I would like to thank CHESS Director, Professor Sol Gruner and Assistant Director, Dr. Ernie Fontes for all of their help and support over the years. Specifically, I am thankful for their numerous invitations to present my work in front of visiting officers from the National Science Foundation. These opportunities boosted my confidence in both my research project and presentation skills.

I would also like to thank Mark Tate for technical assistance involving the setup of x-ray detectors, Aaron Vodnick for making the insane hours we worked at CHESS bearable, Gökhan Arikan for help when I was getting started, as well as every other Gline graduate student.

This work was supported in part by the National Science Foundation and in part by the Cornell Center for Materials Research (CCMR) with funding from the Materials Research Science and Engineering Center program of the National Science Foundation (cooperative agreement DMR-0520404) and is based upon research conducted at the Cornell High Energy Synchrotron Source (CHESS) which is supported by the National Science Foundation and the National Institutes of Health/National Institute of General Medical Sciences under National Science Foundation award DMR-0225180.

TABLE OF CONTENTS

LIST OF FIGURES

CHAPTER 1

INTRODUCTION

1.1 Complex Oxides and their Applications

Complex oxide materials possess a large range of physical properties making them ideal candidates for new device architecture. These materials adopt many crystal structures, but most oxide compounds with the chemical formula ABO_3 may be described by the perovskite unit cell [2]. In the ABO_3 formula, A is a di- or tri-valent cation, B is a tri- or quad-valent cation, and O is an oxygen anion. The idealized cubic perovskite unit cell is shown in Fig 1.1. The perovskite structure was originally named after the perovskite mineral ($CaTiO_3$). While it is now known that $CaTiO_3$ is orthorhombic, the structure in Fig. 1.1 is still referred to as a perovskite unit cell [2, 3]. A few examples of A site cations are Ca^{2+}, Sr^{2+}, Ba^{2+}, Pb^{2+}, and La^{3+}. The tri- or quad-valent B site may include Ti^{4+}, Mn^{3+}, Al^{3+}, Ga^{3+}, as well as many others. The list of complex oxide perovskites can be further expanded by doping the A or B site with a cation of a different oxidation state, thereby changing the properties of the system. For example, substituting a Sr^{2+} for La^{3+} in $LaMnO_3$ causes the average oxidation state of manganese to shift from Mn^{3+} towards Mn^{4+}, increasing the electronic conducivity. In particular, the $La_{1-x}Sr_xMnO_3$ ($0 \leq x \leq 1$) compound has a very rich phase diagram with regions where the material is a ferromagnetic metal, a ferromagnetic insulator, a paramagnetic metal, or a paramagnetic insulator [4].

The high number of elemental combinations in perovskite compounds leads to an enormous range of materials properties, including high-T_c superconductivity [5, 6], colossal magnetoresistance [7–9], ferroelectrics [10, 11], ferromagnetics [12,

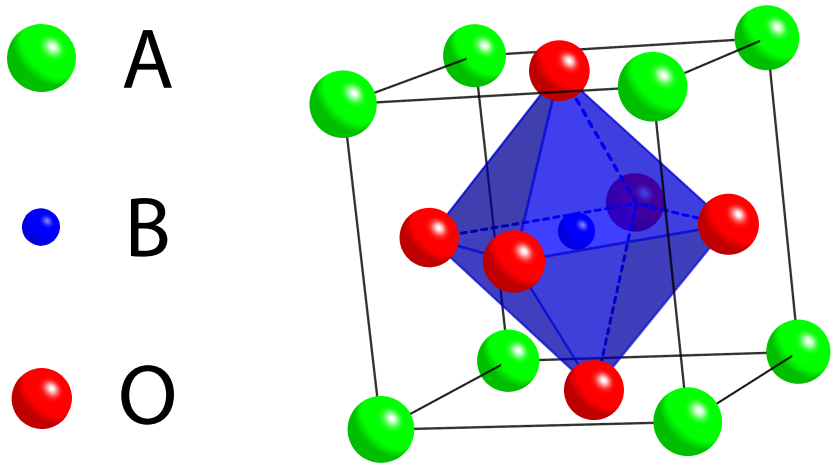

Figure 1.1: The perovskite unit cell. The B cation is at the body centered position, the A cation is at the cell corners, the oxygen anion is at the face centers. The unit cell may be viewed as an oxygen octhedra surrounding the B site.

13], and multiferroics [14–16]. One extremely interesting complex oxide materials system is the $LaAlO_3$ / $SrTiO_3$ $\langle 001 \rangle$ interface. $SrTiO_3$ and $LaAlO_3$ are both insulators with bandgaps of 3.2 eV and 5.6 eV, respectively. Interestingly, when $LaAlO_3$ is grown epitaxially on $SrTiO_3\langle 001 \rangle$ a conducting, quasi-two-dimensional electron gas (q2-DEG) forms at the interface [1]. Additionally, the interface state is insulating if the $LaAlO_3$ film thickness is three monolayers or less, but when the film thickness exceeds three monolayers, the interface becomes conducting [17]. Since this discovery, the interface has been found to be ferromagnetic [18] and superconducting below 200 millikelvin [19]. By far, the most researched property of the $SrTiO_3/LaAlO_3$ system is the q2-DEG. One exciting possibility for this system is the ability to read and write nanoelectronics on demand by applying an electric field to the heterostructure surface using an atomic force microprobe [20,21]. With

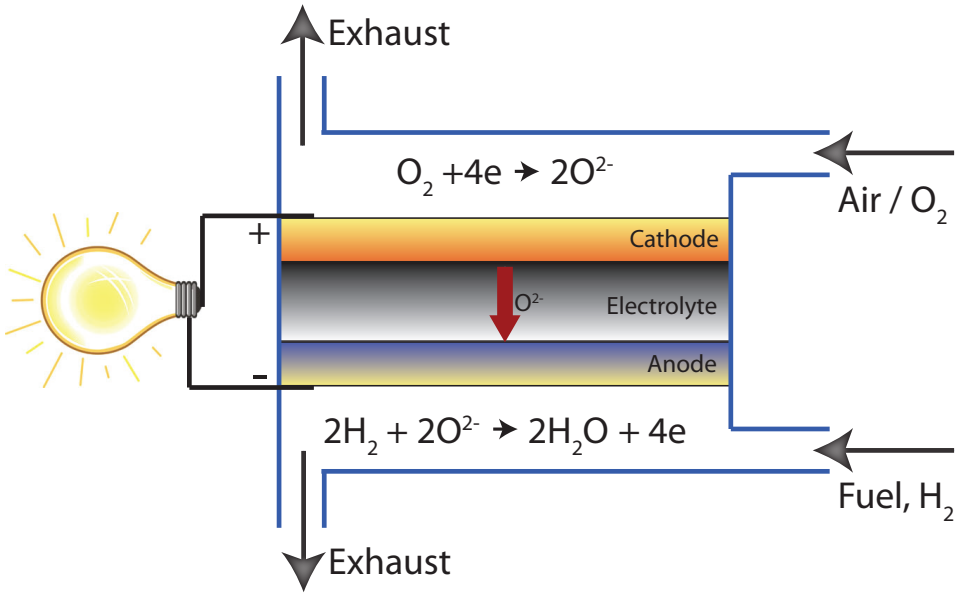

Figure 1.2: A schematic description of a solid oxide fuel cell. Oxygen reduction occurs on the cathode side and fuel oxidation occurs on the anode side.

this technique, field effect devices have been fabricated as small as 2nm [21, 22].

Another application for complex oxides is found in solid oxide fuel cells (SOFC). Fig. 1.2 presents a schematic description of how a SOFC operates. In this device, oxide ions are reduced at the cathode, diffuse through the electrolyte, and react with the fuel on the anode side [23]. During the latter process, the oxide ions give up electrons that may be used in an external circuit. Since the byproduct of generating power with a SOFC is H_2O, these devices are ideal candidates for clean energy production [24]. The complex oxide $La_{1-x}Sr_xMnO_3$ has shown promise as a cathode material [25] due to its high electronic conductivity, high oxygen conductivity, and its compatibility with other SOFC components such as yttria-stabilized zirconia, the most common electrolyte material [23]. The $La_{1-x}Sr_xMnO_3$ compound is currently used in prototype SOFCs by Siemens, AG [25].

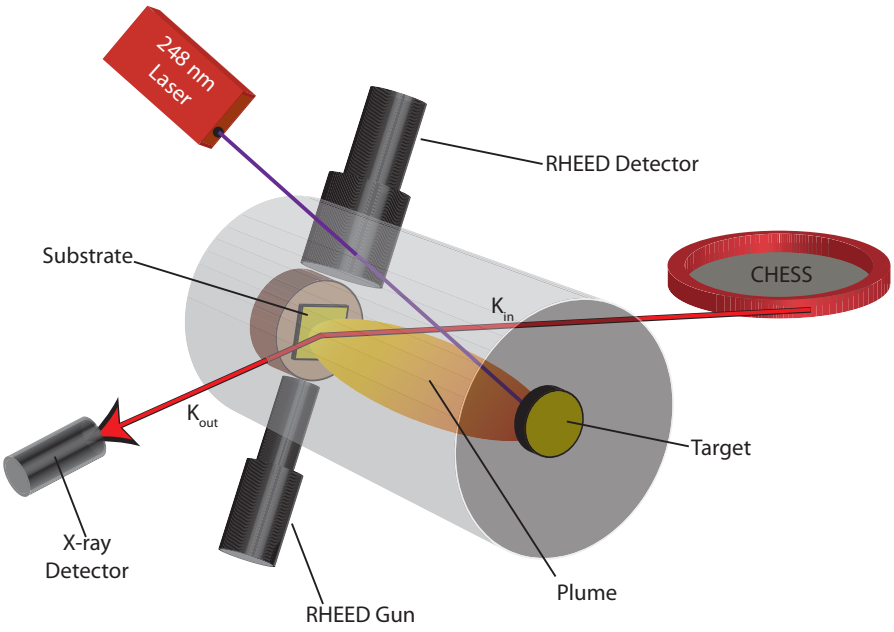

Figure 1.3: A schematic diagram of the pulsed laser deposition chamber in the G3 hutch at the Cornell High Energy Synchrotron Source.

1.2 Pulsed Laser Deposition

Thin films of complex oxides are commonly grown using a physical vapor deposition technique such as molecular beam epitaxy (MBE), sputtering, or pulsed laser deposition (PLD). Of these techniques, MBE and PLD are the most widely used methods to create epitaxial, single crystal films of complex oxides. The main advantage of PLD over MBE is the simplicity with which many different materials may be investigated. Fig 1.3 illustrates the setup for our PLD system. In PLD, an KrF eximer laser (248nm) strikes a target material creating a plume of ionic and neutral species. These species are projected to the substrate at kinetic energies ranging from thermal to 100s of electron volts [26]. The laser is operated at repetition rates ranging from 0.05 Hz to 10 Hz, with each pulse delivering a fraction of

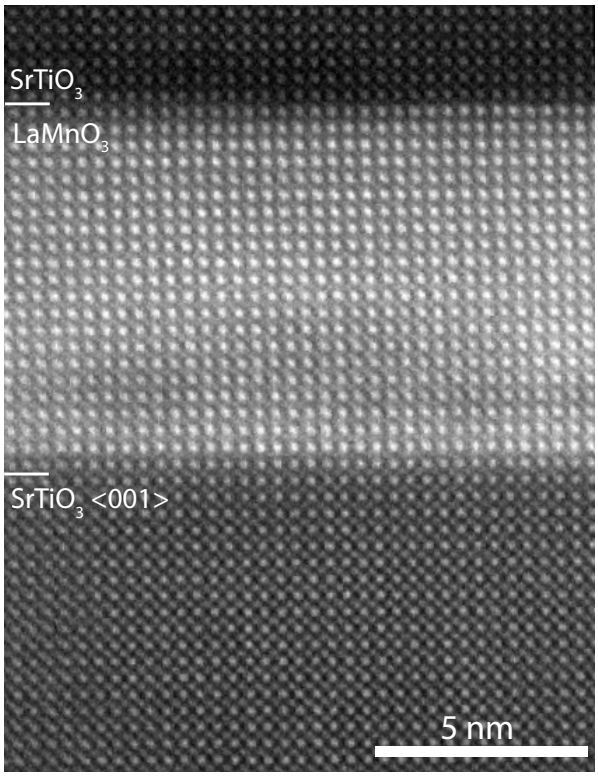

Figure 1.4: A scanning transmission electron microscopy image of a pulsed laser deposited $SrTiO_3\langle 001\rangle/LaMnO_3/SrTiO_3$ heterostructure grown in the G3 hutch at CHESS.

an atomic layer of material. Using this relatively simple technique, extremely high quality epitaxial films with atomically abrupt interfaces may be grown. To illustrate the high quality films produced by PLD, Fig. 1.4 shows a scanning transmission electron microscopy image of a $SrTiO_3\langle 001\rangle/LaMnO_3/SrTiO_3$ heterostructure deposited in our system. This image was taken by Dr. Lena Fitting Kourkoutis of the School of Applied and Engineering Physics at Cornell University. The larger atoms visible in Fig. 1.4 are A-site, while the B-site atoms are seen at the body center of the A-sites. Due to the growth conditions of this heterostructure, the $LaMnO_3$ and $SrTiO_3$ films are most likely oxygen deficient.

Our PLD chamber is located in the G3 hutch at the Cornell High Energy Synchrotron Source (CHESS) and was specifically built to perform in situ x-ray scattering studies during thin film deposition. Because x-ray scattering from surfaces is weak, these studies require synchrotron radiation [27]. In contrast, the majority of research on PLD uses reflected high energy electron diffraction (RHEED) to monitor the deposition process [28, 29]. This is due to the relative simplicity of installing and performing RHEED, and the fact that it allows sub-monolayer sensitivity of the growth rate during layer-by-layer deposition.

While the simplicity of RHEED is appealing, it is limited compared to x-ray scattering in at least two ways. First, the experimental geometry of RHEED limits the penetration depth to the first few atomic layers [30]. Conversely, x-rays will typically penetrate many microns into a material during deposition, making the technique ideal for structural studies at buried layers. A second limitation of RHEED is that, because electrons scatter strongly compared to x-rays, electron diffraction is difficult to model quantitatively. Surface x-ray scattering, in the geometries employed here, can be described by kinematical scattering theory [31]. Lastly, many complex oxides deposited with PLD require a high oxygen pressure in the deposition chamber. The electrons interact strongly with the process gas, requiring a differentially pumped RHEED system. As seen in Fig. 1.3, our chamber is equipped with a differentially pumped RHEED system that can operate simultaneously with x-ray scattering measurement.[1]

The largest distinction between PLD and MBE is the kinetic energy of the impinging particles. MBE is considered a near-equilibrium deposition technique,

[1]There have been some difficulties in getting our RHEED system operational. Specifically, the deposition chamber designed to have beryllium windows as well as ports for the RHEED system has deformed. Work is currently underway to repair the equipment.

while one might expect non-thermal processes to occur during PLD. These non-thermal processes may include transient mobility, downward funneling, insertion, or atom "knockout" [32]. Despite numerous studies to probe the materials physics occurring during PLD [28, 29, 33–39] a consensus, fundamental understanding of the technique has not been obtained. One of these studies used scanning tunneling microscopy (STM) to measure surface coarsening during $SrTiO_3$ homoepitaxy, but the temporal resolution was limited to ≈30 seconds [37]. Alternatively, reflectivity-based studies have given excellent results with temporal resolution down to microseconds [34, 35, 38], but these techniques do not provide a measurement of the lateral length scales during growth.

One success of my research is that it demonstrates how to bridge the gap between the low temporal resolution of (scanning) techniques that probe the lateral length scales and the high temporal resolution (reflectivity based) techniques that probe only surface roughness. This was achieved by performing in-situ simultaneous x-ray diffuse scattering and surface reflectivity during PLD in the G3 hutch at CHESS. This technique allows us to measure the in-plane surface evolution using the diffuse scattering signal, while simultaneously measuring the surface roughness evolution using the specular reflectivity. These measurements have been performed with temporal resolution down to 100 milliseconds. A second outcome of my research is the discovery, thanks to the penetrating power of x-rays, of a phase transition that occurs at a buried layer of an oxide heterostructure. As mentioned above, the extinction depth of conventional RHEED prohibits this type of measurement, and therefore x-ray diffraction was required to observe this process in real time.

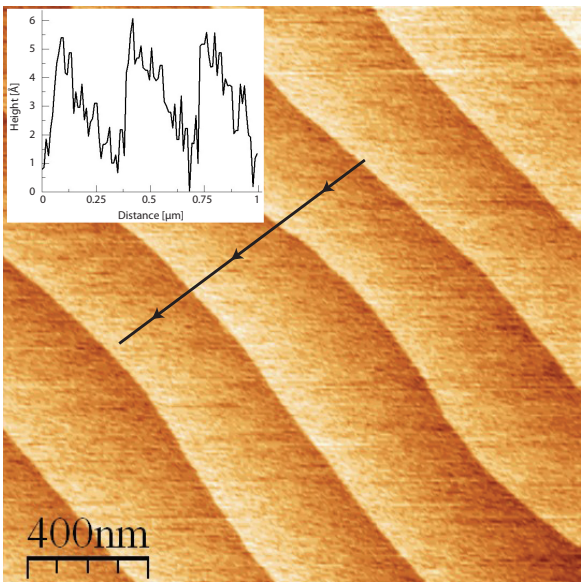

Figure 1.5: An atomic force microscopy image of an $SrTiO_3\langle 001\rangle$ substrate after performing the etching procedure. A real-time plane fit was performed during data acquisition. The atomically flat terraces are TiO_2 terminated. The inset show a linear scan, illustrating that the miscut steps are one unit cell high (a_{STO}=3.905Å).

1.3 Surface Preparation of $SrTiO_3\langle 001\rangle$

The island nucleation density of a film is directly affected by preexisting features on a substrate surface [40]. Therefore, each starting surface must be the same, down to the atomic level, to achieve reproducible results. More specifically, this is necessary so that a measured change in surface length scale can be directly correlated to a change growth parameters, rather than a change in starting surface. We achieve this by performing a buffered oxide etch, followed by a high temperature anneal in flowing oxygen. The procedure is modeled after the standard technique used by the oxide community [41, 42]. The details of the etch procedure are outlined in Appendix A. Figure 1.5 shows a substrate after the surface preparation procedure

has been performed. The substrate is single surface (TiO_2) terminated and has atomically flat terraces separated by unit cell high steps. Each substrate used in these experiments has been etched, annealed, and an AFM image was taken prior to growth.

CHAPTER 2

X-RAY SCATTERING DURING THIN FILM DEPOSITION

By performing in situ x-ray diffuse scattering measurements simultaneously with x-ray specular reflectivity, we are able to monitor the temporal dependence of the in-plane surface length scale and the out-of-plane surface roughness. In this chapter, I briefly review the behavior of the specularly reflected x-ray beam, using the kinematical scattering approximation. Then, I show that the island size and shape distribution is directly related to the diffuse scattering line shape. By monitoring this line shape during deposition, the average distance between surface features is determined. Finally, I describe the experimental scattering geometry at the G3 hutch at the Cornell High Energy Synchrotron Source.

2.1 Specular Scattering During Thin Film Deposition

When monitoring the x-rays reflected from an smooth substrate surface, streaks of intensity form in the direction parallel to the surface normal. The streaks are known as crystal truncation rods (CTR) [43], and their x-ray scattering amplitude in the q_z direction is given by the sum of the scattering from all layers [31]:

$$A_{CTR} = F \sum_{j=0}^{\infty} e^{iq_z\, j\, d}, \tag{2.1}$$

where F is the scattering amplitude for one layer, d is the layer spacing, and $q_z = 2\pi\left(\frac{l}{d}\right)$ [where l is the reciprocal lattice vector]. Material that is deposited on the surface will also contribute to the scattering amplitude, resulting in the equation:

$$A_{CTR} = F_{sub}\frac{1}{1 - e^{-iq_z d_{sub}}} + F_{film} \sum_{k=1}^{K} \theta_k e^{iq_z\, k\, d_{film}}, \tag{2.2}$$

where I have simplified the scattering amplitude of the substrate. The parameter K in Eqn. 2.2 denotes the number of layers grown and θ_k gives the fractional coverage of the k^{th} layer.

Equation 2.2 shows that the specular intensity is directly related to the amount of inter-layer transport that is occurring during deposition [27]. For example, near the completion of the first monolayer, material arriving on the surface will land on both the substrate and the first layer. The material on the first layer will diffuse downhill (inter-layer), filling in the first layer. In this case, the fractional coverage of each layer, θ_k, is time dependent. Therefore, the time dependence of the specular intensity is a direct measurement of the time scale for interlayer transport.

There are two specific scattering geometries used throughout this thesis. In Chapters 3 and 4 the intensity of the CTR is monitored near the quarter-Bragg ($q_z = 1/4$ reciprocal lattice units [r.l.u]) and in Chapter 5 the experiments are performed at the anti-Bragg ($q_z = 1/2$ r.l.u.). The exact behavior of this intensity is dependent upon the specifics of the experiment, and is discussed for each case in its corresponding chapter.

2.2 Diffuse Scattering During Thin Film Deposition

During layer-by-layer growth, unit cell high islands on the surface give rise to diffuse scattering around the specularly reflected beam. The line shape of the diffusively scattered x-rays may be directly correlated to the island size and shape distribution. The mathematical representation of surface diffuse x-ray scattering is well known [32,44,45], however I outline the basic steps and equations here as an aid to the reader. We begin the derivation of the diffuse scattering intensity by writing

the general formula for the scattering amplitude, $A(q_{||})$, of a two dimensional surface partially covered by islands as [31, 32]:

$$\vec{A} = \sum_j f_j(\vec{q}_{||})\; e^{i\vec{q}_{||}\cdot\vec{r}_j}. \tag{2.3}$$

In this equation, $\vec{q}_{||}$ is the in-plane scattering vector, $\vec{r}_j$ is a vector describing the location of the j^{th} island, and $f_j(\vec{q}_{||})$ is the Fourier transform of the j^{th} island. For simplicity, I have not included the substrate contribution to the scattering, which does not affect the diffuse scattering line shape [32, 46]. The scattering intensity, $I = |A|^2$, may be obtained directly from Eqn. 2.3:

$$I = \langle \sum_{j,k} f_j f_k^*\; e^{i\vec{q}_{||}\cdot(\vec{r}_j - \vec{r}_k)} \rangle, \tag{2.4}$$

where the angle brackets, $\langle .. \rangle$, represent an ensemble average. By assuming the island form factor to be independent of position and factoring out the $j = k$ and $j \neq k$ terms, we arrive at:

$$I = N\langle |f|^2 \rangle + |\langle f \rangle|^2 \sum_j \sum_{k \neq j} e^{i\vec{q}_{||}\cdot(\vec{r}_j - \vec{r}_k)}, \tag{2.5}$$

where N is the total number of scattering centers. Referring to the right hand side of Eqn. 2.5, the first term, $N\langle |f|^2 \rangle$, gives the small angle scattering contribution to the intensity. This term represents the island's "self" correlation, and is therefore related to the average of the square of the island form factor. The second term on the right hand side of Eqn. 2.5 is the interference term, representing the correlation between different islands. By introducing the island occupancy parameter, $n(\vec{x})$, defined as $n(\vec{x}) = \sum \delta(\vec{x} - \vec{x_i})$, the interference term may now be written as an integral, leading to:

$$I = N\langle |f|^2 \rangle + |\langle f \rangle|^2 \int\int \langle n(\vec{r}_1)\, n(\vec{r}_2) \rangle\, e^{i\vec{q}_{||}\cdot(\vec{r}_1 - \vec{r}_2)}\, d\vec{r}_1 d\vec{r}_2. \tag{2.6}$$

To aid in discussing the island-island interference term, it is useful to introduce the island pair distribution function [32, 44]:

$$g(\vec{r}) = (N\rho)^{-1} \int \langle n(\vec{R})\, n(\vec{R} - \vec{r}) \rangle \, d\vec{R}, \tag{2.7}$$

which gives the probability of having an island centered at a distance $\vec{r}$ from an island located at $\vec{R}$. In Eqn. 2.7, ρ represents the average density of islands, and we have shifted to a continuum representation n. By letting $\vec{r}_1 \rightarrow \vec{R}$ and $\vec{r}_2 \rightarrow \vec{R} - \vec{r}$, substituting Eqn. 2.7 into Eqn. 2.6, and assuming translational invarance, we arrive at:

$$I = N\langle |f|^2 \rangle + N\rho \, |\langle f \rangle|^2 \int g(\vec{r}) e^{i\vec{q}_{||} \cdot \vec{r}} \, d\vec{r}. \tag{2.8}$$

The island pair distribution function approaches a unity as $\vec{r} \rightarrow \infty$, giving rise to a specular component. Therefore by adding and subtracting unity from $g(\vec{r})$, we can split the the interference term into a specular and diffuse component. Grouping the specular term and the diffuse terms yields the equation $I = \Delta I_{spec} + I_{diff}$ where:

$$\Delta I_{spec} = 4\,\pi^2 N \rho \, \delta(\vec{q}_{||}) \, |\langle f \rangle|^2, \tag{2.9}$$

and

$$I_{diff} = N\langle |f|^2 \rangle + N\rho |\langle f \rangle|^2 \int [g(\vec{r}) - 1] e^{i\vec{q}_{||} \cdot \vec{r}} \, d\vec{r}. \tag{2.10}$$

Equation 2.9 states the specular intensity component resulting from the positional correlations of islands on the surface. The diffuse scattering intensity, Eqn. 2.10, states the direct relationship between the island distribution on the surface, $g(\vec{r})$, and the observed diffuse scattering line shape. More specifically, the interference term in Eqn. 2.10 is the two-dimensional Fourier transform of the pair distribution function.

It is useful to describe two different island distributions: (1) randomly distributed islands and (2) correlated islands that do not overlap. These cases have

been discussed in detail by Evans, et al. [32]. The first case is trivial, since $g(\vec{r}) = 1, \forall\, r \neq 0$. Therefore the diffuse scattering, I_{diff}, is sensitive to the island form factor. Specifically, correlations between atoms within each island produce a maximum in I_{diff} at $q_{||} = 0$ and the intensity decreases monotonically as $q_{||}$ increases. The full width half maximum of the resulting lineshape is inversely proportional to the average island radius. For case (2), the island positions are correlated and each island is surrounded by a finite depletion region, i.e. two islands may not occupy the same space. The pair distribution function is zero in the depletion region and has a finite value at large distances, producing a maximum in the diffuse scattering line shape at $q_{||} \neq 0$. This ring of diffuse scattering is referred to as a Henzler ring [47]. Empirically, its radius q_0, is inversely proportional to the distance between island centers, L_{isl}. The equation $L_{isl} \approx 2\pi/q_0$ gives an excellent approximation for the relationship between the diffuse scattering peak position and characteristic surface length scale [32, 48].

The diffuse scattering line shape can be directly correlated to the island size/shape distribution using Eqn. 2.10. Therefore, by performing in situ surface diffuse x-ray scattering, the temporal dependence of the average island separation may be measured at time scales much smaller than those attainable using STM. Additionally, x-ray scattering has the advantage of statistical averaging a large surface area, as discussed in the preceding chapter.

2.3 Diffuse Scattering Experimental Setup

All x-ray measurements were performed using a custom PLD/x-ray diffraction system installed in the G3 hutch at the Cornell High Energy Synchrotron Source.

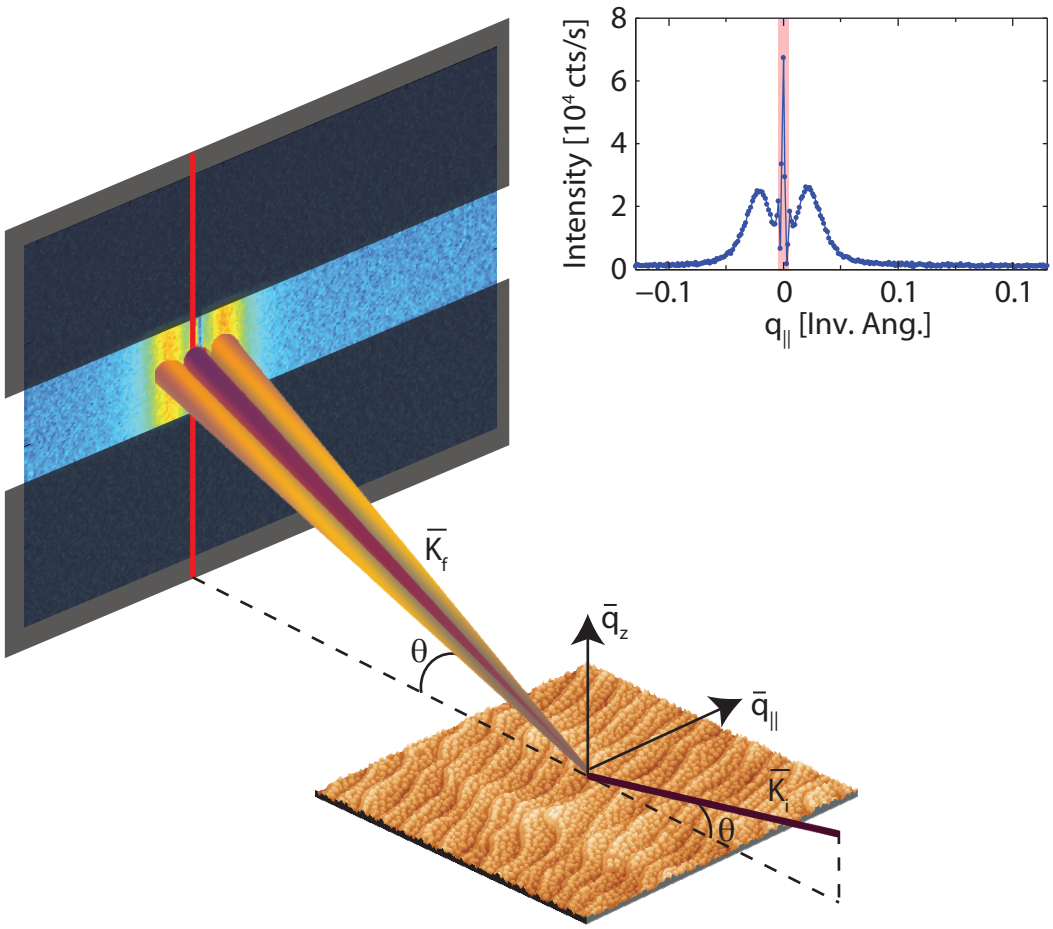

Figure 2.1: Experimental setup for diffuse scattering. A monochromatic x-ray beam reflects off the surface with a specular component (purple) and diffuse component (gold). The inset is a plot of the intensity measured at the detector as a function of $q_{||}$. The red (or grey) box shows the range of $q_{||}$ that was attenuated.

Figure 2.1 illustrates the experimental geometry. The surface shown is an atomic force microscopy (AFM) image taken after the deposition of homoepitaxial $SrTiO_3$. As suggested by the figure, surface steps are always aligned perpendicular to the incident beam. The incident x-ray beam scatters in the $\vec{q}_{||}$ direction and the intensity profile is directly related to the island correlations on the surface via Eqn. 2.10.

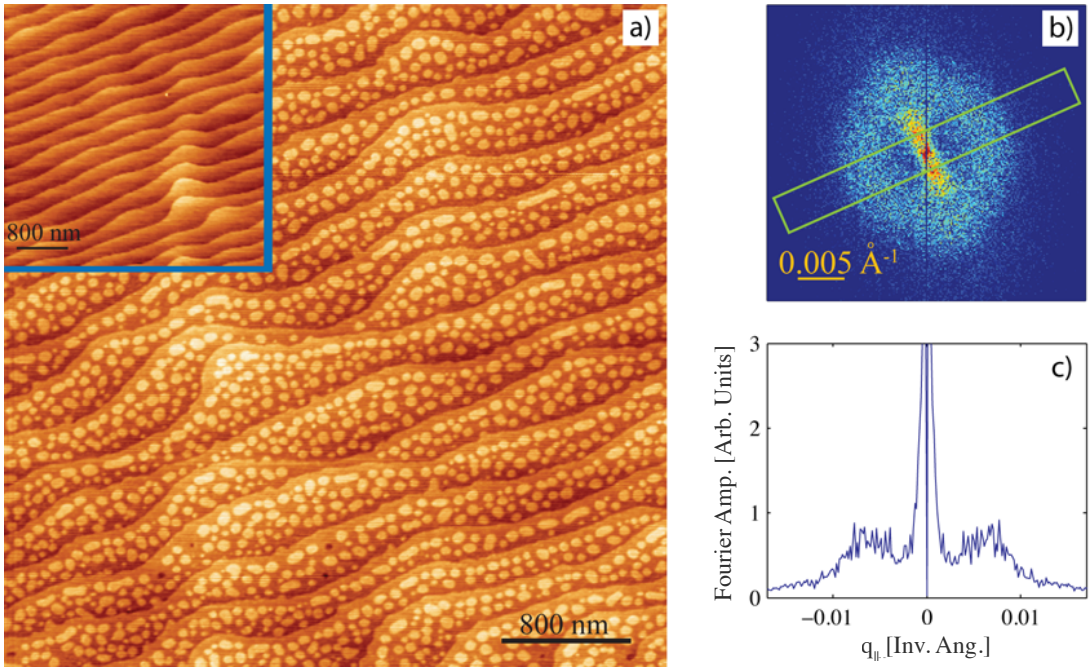

Figure 2.2: Post Deposition Atomic Force Microscopy: (a) The ex situ AFM reveals unit cell high islands on the surface. The inset shows an AFM of the etched and annealed same sample prior to deposition. (b) The fast Fourier transform (FFT) of the AFM image shows the distinctive Henzler ring, confirming that the islands are correlated. (c) The cross-section of the FFT.

The specular component of the reflected signal is attenuated to prevent detector saturation. To optimize the signal-to-background ratio of the diffuse scattering, the experiment is performed near the quarter-Bragg position on the crystal truncation rod. The inset to Fig. 2.1 is a plot of the measured intensity as a function of $q_{||}$ after the deposition of 0.5 monolayers of homoepitaxial $SrTiO_3$. The diffuse scattering shows a clear maximum with a peak position of $q_0 = 0.0213$ Å^{-1}, suggesting that the islands on the surface are correlated with an average island spacing of $L_{isl} = 2\pi/q_0 = 29.5$ nm.

To confirm that the diffuse scattering peaks are the direct result of single unit cell high islands, ex-situ atomic force microscopy (AFM) was performed on the sample grown in Fig. 3.1(a) in Chapter 3. Fig. 2.2(a), shows the AFM image revealing the presence of unit cell high islands between terraces. As a reference, the inset shows the AFM image of the substrate taken prior to growth. The fast Fourier transform (FFT) of the post deposition AFM is shown in Fig. 2.2(b). Many interesting features are realized in the FFT. First, the step edge periodicity is seen in the direction perpendicular to the step edges, exemplifying the need to orient the step edges perpendicular to the incident beam, as previously discussed. The second interesting feature is the presence of the diffuse Henzler ring [47]. As discussed in Section 2.2, the presence of this ring is a direct result of the correlated islands on the surface. Figure 2.2(c) shows the Fourier amplitude as a function of $q_{||}$ for the boxed region. Our experimentally detected diffuse x-ray intensity (Fig. 2.1(inset)) is a cut through the Henzler rings, roughly analogous to the cross-section show in Fig. 2.2(c). While there are subtile differences between these two data sets, the significant reduction in noise is a key feature of the x-ray data. Additionally, the AFM image was acquired over a 1 hour scan, while the x-ray data was acquired in 1 second exposure. While the x-ray measurement does not produce a real-space image, the reciprocal space data represents a drastic increase in temporal resolution.

CHAPTER 3

MEASUREMENTS OF SURFACE DIFFUSIVITY AND COARSENING DURING PULSED LASER DEPOSITION

We now present the results of applying time resolved simultaneous specular and diffuse x-ray scattering to the pulsed laser deposition of homoepitaxial $SrTiO_3$. These results were reported in *Physical Review Letters*.[1] We reproduce the published article below, beginning in the first paragraph with the article abstract.

Pulsed Laser Deposition of homoepitaxial $SrTiO_3\langle 001\rangle$ was studied with *in-situ* x-ray specular reflectivity and surface diffuse x-ray scattering. Unlike prior reflecivity-based studies, these measurements access both the time- and the length-scales of the evolution of the surface morphology during growth. In particular, we show that this technique allows direct measurements of the diffusivity for both inter- and intra-layer transport. Our results explicitly limit the possible role of island break-up, demonstrate the key roles played by nucleation and coarsening in PLD, and place an upper bound on the Ehrlich-Schwoebel barrier for downhill interlayer diffusion.

Pulsed Laser Deposition (PLD) presents an exceptional challenge for experimental and theoretical study due to its highly non-equilibrium nature, the vast range of time- and length-scales involved, and the complex stoichiometry of the materials system studied. Consequently, fundamental issues, such as the roles played by the pulsed nature and the kinetic energy of the deposit, remain unresolved [28, 33, 34, 38, 39]. System-specific kinetic properties are also difficult to

[1]Reprinted article with permission from: J.D. Ferguson, G. Arikan, D. S. Dale, A. R. Woll, and J.D. Brock, "Measurements of Surface Diffusivity and Coarsening During Pulsed Laser Deposition," Physical Review Letters **103**(25), 256103 (2009).

obtain. For example, scanning tunneling microscopy has revealed a rich variety of phenomena on $SrTiO_3$ surfaces [37, 49], but at time scales longer than those relevant to growth. In contrast, fast studies of PLD have typically employed electron [28, 29] or x-ray [34, 35, 38, 39, 50] specular reflectivity. These studies have excellent time resolution, but are sensitive only to the average atomic-scale surface roughness [51, 52], and therefore provide an incomplete description of surface kinetics.

In this Letter, we show that *in-situ* x-ray diffuse scattering provides critical length scale information absent from x-ray reflectivity alone, at time scales appropriate to study PLD. The general x-ray scattering experimental details are given in Section 2.3, and the details specific to this chapter are given in the Experimental Details section below. Figs. 3.1(a-c) show false color images of the intensity of both the specular ($q_{||} = 0$) and the surface diffuse scattering as a function of time and $q_{||}$, during the deposition of approximately 11 monolayers (ML) of unit cell step height of $SrTiO_3$ at 3 temperatures. As material is deposited on the surface, the specular intensity drops while diffuse lobes of scattering appear on both sides of the specular rod. These lobes are cuts through "Henzler rings" arising from 2D islands on the surface [47, 53], as verified by *ex-situ* atomic force microscopy (See Fig. 2.2).

At low layer coverage, θ ($0 < \theta < 0.4$ ML), the radius of these rings, q_0, is inversely proportional to the average island separation, $L_{isl} \approx 2\pi/q_0$ [48]. As more material is deposited, the intensity of the specular rod and the diffuse lobes oscillate out of phase with a period of 1 ML. Near layer completion ($0.7 < \theta < 1$ ML), q_0 is a measure of the separation between holes rather than islands.

A conspicuous feature of Figs. 3.1(a-c) is that increasing the substrate temper-

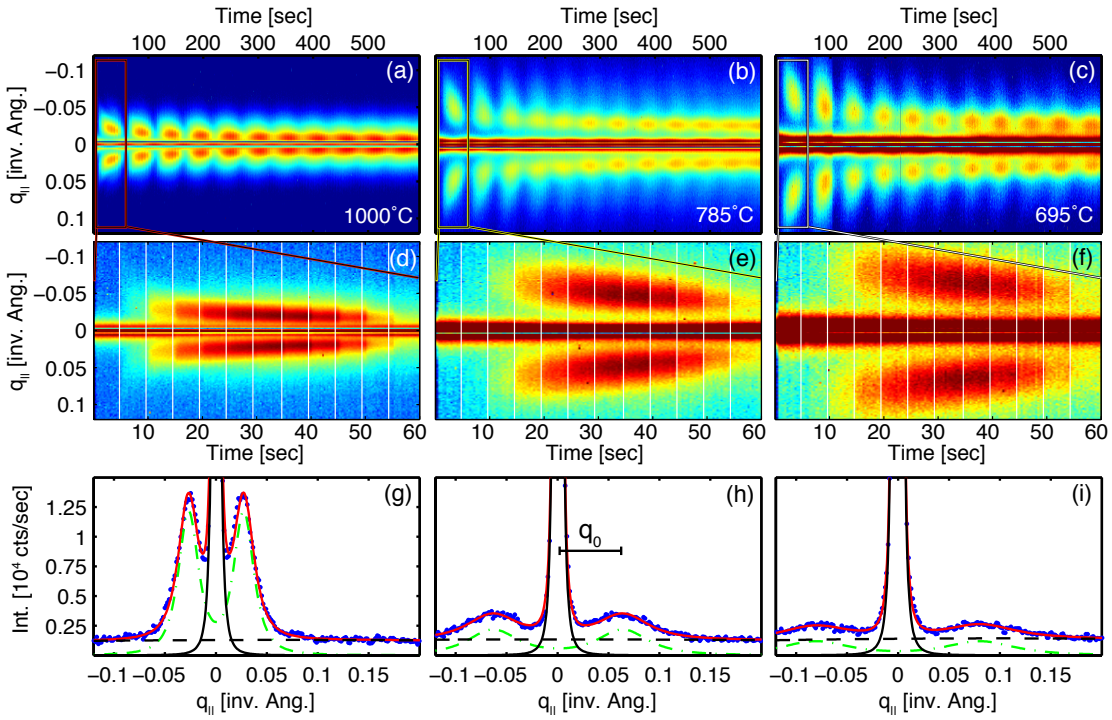

Figure 3.1: Diffuse x-ray scattering for the PLD of $SrTiO_3\langle 001\rangle$. (a-c) Depositions of ∼11 ML at 1000°C, 790°C, 695°C, respectively. (d-f) The corresponding first ML. Vertical lines represent the laser pulses (first pulse at 5 s). (g-i) Scattering line shape at $t = 16.5$ s for each temperature. I_{fit} (red, solid) consists of I_{diff} (green, dash-dot), I_{spec} (black, solid) and I_{bg} (black, dashed).

ature results in a decrease in q_0, corresponding to a decrease in island density, as expected from classical nucleation theory [54]. A second feature of the data is that q_0 decreases with increasing layer number. This is a general feature of every data set we obtained, and reflects the growth surface's "memory" of underlying layers. If a new layer nucleates before layer completion, the remaining holes function as adatom sinks, reducing the adatom density, thereby producing a smaller nucleation density.

Figs. 3.1(d-f) show an enlarged view of the 1st ML of growth from Figs. 3.1(a-

c). At 1000°C, diffuse scattering appears between the first and second pulses. At sufficiently lower temperatures ($\leq$ 785°C), diffuse scattering is not visible until after the second pulse, indicating either delayed nucleation or intensity below our detection limit, as discussed below.

To extract quantitative information, the x-ray data were fit to the sum of three independent components,

$$I_{fit}(q_{||}) = I_{bg} + I_{spec}(q_{||}) + I_{diff}(q_{||} + q_0) + I_{diff}(q_{||} - q_0). \tag{3.1}$$

In this equation, I_{bg} is a constant background, and $I_{spec}(q_{||})$, $I_{diff}(q_{||} + q_0)$, and $I_{diff}(q_{||} - q_0)$ take the form:

$$f(x) = I_0/[1 + \xi^2 x^2]^{3/2}, \tag{3.2}$$

where ξ is the correlation length. The parameters I_0 and ξ each take on two values, associated with I_{spec} and I_{diff}. Eq. (3.2) with $q_0 = 0$ corresponds to the scattering profile of a random distribution of islands [55, 56]. Figs. 3.1(g-i) show the single frames from Figs. 3.1(d-f) corresponding to $t = 16.5$ s: the frame immediately following the third laser pulse. Also shown are the best fit to Eq. (3.1) and its components. The agreement between the fitting function and the data is excellent, with a typical $\chi^2 \approx 1.3$.

Fig. 3.2a shows the evolution of q_0 and ξ for the first monolayer at 850°C. Immediately following the first pulse, a diffuse peak is observed at $q_0 = 0.066 \pm 0.005$ Å, indicating that some islands have nucleated. This value of q_0 corresponds to an island density of $n_x = (1.0 \pm 0.1) \times 10^{12}$ cm^{-2} if a triangular lattice is assumed. A rising q_0 immediately following the first pulse would signify nucleation of new islands from a supersaturation of adatoms. Instead, q_0 decreases monotonically and continuously, indicating a steadily decreasing island density. This shows that

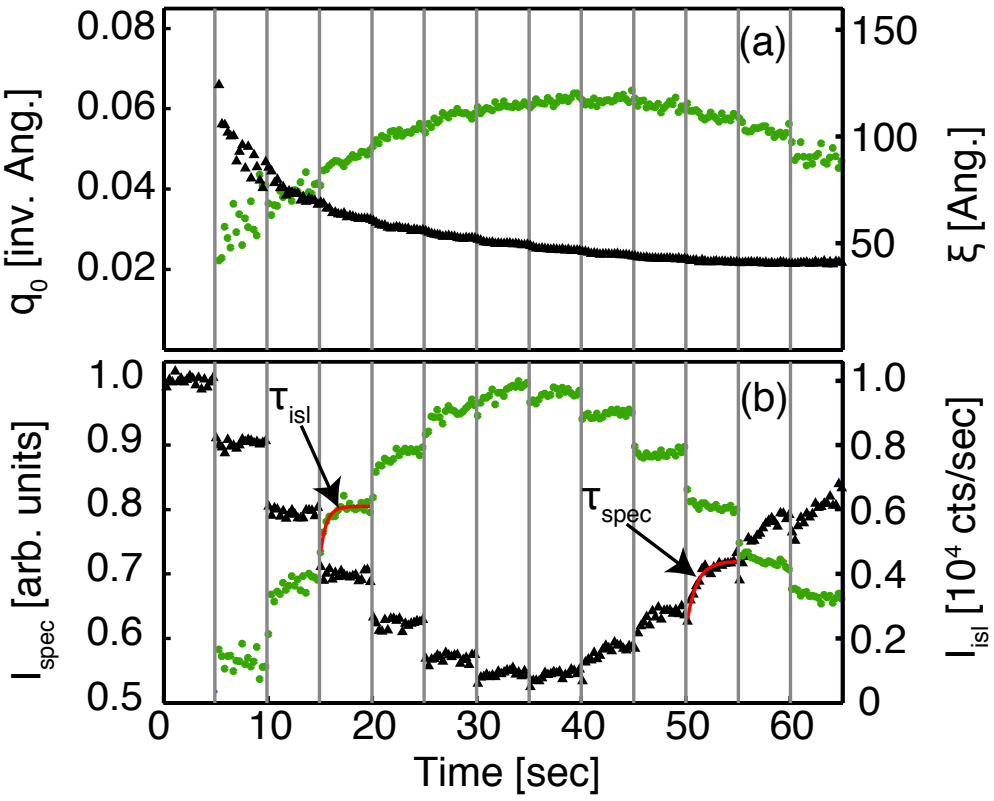

Figure 3.2: (a) The peak position of the diffuse lobes, q_0 (black) and the correlation length, ξ (green, grey) at 850°C are shown for the 1^{st} ML. Vertical lines represent laser pulses(1^{st} pulse at 5 s). (b) I_{spec} (black) and I_{isl} (green) are shown. The characteristic diffusion times, τ_{isl} and τ_{spec} are determined by fitting I_{spec} and I_{isl}.

some of the newly formed islands are disappearing, and thus that island coarsening [57, 58], rather than nucleation, drives the evolution of q_0 during this time. We observe similar coarsening for substrate temperatures as low as 695°C.

A key parameter in PLD growth is the decay time of the adatom supersaturation resulting from the pulse [36]. Our diffuse scattering measurements are not directly sensitive to adatom supersaturation. Specifically, since they only extend to $q_{max} = 0.2$ Å^{-1} (see Figs. 3.1(g-i)), they are insensitive to lateral correlations

smaller than $\approx 2\pi/q_{max} \approx 31$ Å, such as adatoms or very small islands. However, it is easily shown that, if the coverage and specular intensity are both constant, the total diffuse scattering intensity is also constant[2]. We therefore write the total in-plane surface scattering as $I_{tot} = I_{spec} + I_{isl} + I_{sm}$, where I_{sm} is the scattered intensity from small features not captured by our measurement. I_{isl} is equal to I_{diff} from Eq. (3.1), integrated over the q_z plane:

$$I_{isl} = 2\pi I_0(q_0/\xi)[1 + \sqrt{1 + (\xi q_0)^{-2}}], \tag{3.3}$$

and is associated with the total diffuse scattering due to large islands, i.e. the islands separated by $> 2\pi/q_{max}$. When the specular intensity between pulses is constant, a time-dependent I_{isl} corresponds to mass transfer between small features and the characteristic large islands that give rise to I_{isl}.

The specular intensity, I_{spec}, and total diffuse intensity I_{isl} for an 850°C deposition are shown in Fig. 3.2b. Apart from the jumps in I_{spec} associated with each deposition pulse, we observe two, distinct slower changes occurring between pulses. The first is a change in I_{spec} that occurs near monolayer completion and has been studied previously [28, 29, 34, 38, 39]. The second slow change, which manifests in I_{isl} and has not previously been reported, occurs at low coverage. After the third laser pulse, the rise in I_{isl} lags behind the fast drop in I_{spec}. As discussed above, this delay indicates an increase in the amount of material in large islands. Moreover, since I_{spec} is constant during this time, this mass transfer corresponds solely to intralayer transport.

The relaxation kinetics described above can be quantified by fitting I_{spec} at high θ, and I_{isl} at low θ to a simple exponential with characteristic relaxation

[2]By integrating Eq. (6) in Ref. [59] over $q_{||}$, it is seen that both I_{spec} and I_{diff} depend only on $h(q_z)$, the Fourier transform of the vertical height distribution.

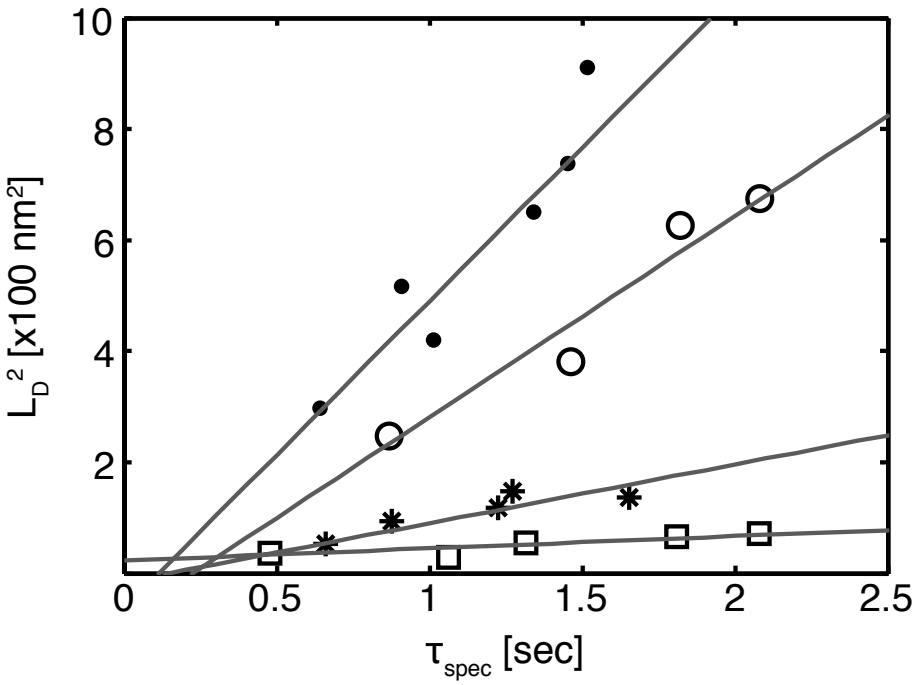

Figure 3.3: Length scale for diffusion, L_D^2 vs. τ_{spec} for 1000°C (•), 850°C (◦), 785°, (∗), and 695°C (□). The linear relationship shows that diffusion is the rate limiting process.

times τ_{spec} and τ_{isl}. However, the physical process or processes giving rise to these time constants cannot be determined from Fig. 3.2 alone. For example, the diffusing species may come from pre-existing islands; therefore, both τ_{spec} and τ_{isl} may be determined by either the rate of adatom detachment or the rate of surface diffusion. If present, an Ehrlich-Schwoebel (ES) barrier for downhill diffusion would also contribute to τ_{spec}. We are able to resolve this ambiguity by examining the relationship between τ_{spec} and q_0 obtained for different layers in a single growth, exploiting the fact that q_0 decreases with increasing layer number. If diffusion is indeed the rate-limiting process determining τ_{spec} and if the average diffusion

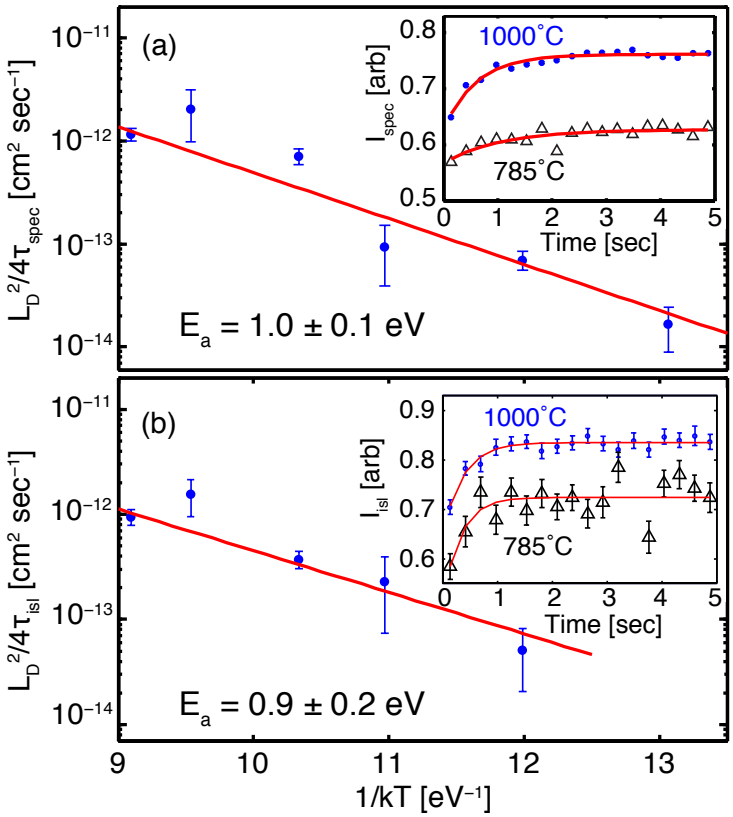

Figure 3.4: (a) Arrhenius behavior of the diffusivity at $\theta \approx 0.8$ML. (inset) τ_{spec} is obtained from the specular relaxation at high coverage, during inter-layer transport. (b). Diffusivity at $\theta \approx 0.25$ ML. (inset) τ_{isl} is determined by fitting the time evolution of I_{isl}.

length, L_D, is determined by q_0 then the Einstein relation, $L_D^2 = 4D\tau$ applies [60]. We associate each q_0 with an approximate diffusion length $L_D = L_{isl}/2 = \pi/q_0$, (approximately half the distance between hole centers), and plot L_D^2 vs. τ_{spec} in Fig 3.3. The values used were obtained from approximately the same exposed coverage, $\theta \approx 0.8 \pm 0.04$, at several different thicknesses for each film. A clear linear relationship is observed, so that we may associate the slope in Fig. 3.3 with the diffusivity, D. We also assign τ_{isl} to diffusion-limited transport, since only a

subset of the processes responsible for τ_{spec} are involved.

Figs. 3.4(a,b) show Arrhenius plots of D obtained from the analysis of τ_{spec} and τ_{isl} for the first ML. The best-fit lines are shown, corresponding to activation energies of $E_a = 1.0 \pm 0.1$ eV and $E_a = 0.9 \pm 0.2$ eV for inter- and intra-layer transport, respectively. The difference in these energies, 0.1 ± 0.22 eV, is a direct measure of the ES barrier. Remarkably, these data sets yield not only the same slopes (within experimental error) but also the same values of diffusivity throughout the temperature range studied, suggesting that the ES barrier is negligible. We thus combine the data in Figs. 3.4(a-b) to give the single result $D = D_0 \exp(-E_a/k_B T)$, with $D_0 = 10^{-8\pm1}\text{cm}^2\ \text{s}^{-1}$ and $E_a = 0.97 \pm 0.07$ eV. The determination of both D_0 and E_a through diffraction-based measurements alone represents a principle result of this work.

The value of E_a reported here is larger than two values, 0.48 ± 0.05 eV and 0.6 ± 0.2 eV, previously reported in the literature [28,35]. In these reports, E_a was obtained from the temperature dependence of τ_{spec} implicitly assuming a constant length scale. The effect of this assumption on the determination of E_a is made explicit by writing the temperature dependence of the length scale in Arrhenius form, $L_D = L_0 \exp(-E_L/k_B T)$, and rewriting the Einstein relation:

$$\tau_{spec} = (L_0^2/4D_0) \exp[(E_a - 2E_L)/k_B T] \tag{3.4}$$

Eq. (3.4) shows that the activation energy measured from τ_{spec} alone underestimates the activation barrier for diffusion, E_a, by $2E_L$. We note that our value of $E_a = 0.97 \pm 0.07$ eV is very close to that of 1.2 ± 0.1 eV measured for diffusion of TiO_x "diline" units on a reconstructed $SrTiO_3$ surface [49].

Our results provide new insight into the possibility of energetic mechanisms

promoting smooth growth in complex oxide PLD. One such proposed mechanism is island breakup, in which energetic impinging material breaks up existing islands, delaying second-layer nucleation. Island-breakup has previously been observed in simulations of metal/metal epitaxy [61,62] and was recently invoked [39] to explain experimental results of PLD of $La_{1-x}Sr_xMnO_3$ on $SrTiO_3$. Specifically, Ref. [39] suggests that island break-up produces an increasing island density when $\theta < 0.5$ ML. Although the system studied here is not precisely the same as in Ref. [39], Fig. 3.2a demonstrates that the island density monotonically decreases with θ from the earliest moments after nucleation. Island breakup could also manifest in our measurement as a decrease in I_{isl} as mass is transferred from large islands to smaller species without changing q_0. However, we do not observe such a decrease. Thus, the possible manifestations of island break-up in our data are obscured by island coarsening.

A second proposed non-thermal smoothing mechanism suggested by prior experimental work on complex-oxide PLD, is enhanced downhill transport [28, 34, 38, 39]. The experimental basis for this suggestion is the observation, based on specular reflectivity, that downhill transport occurs on two widely separated time scales [34, 38]. Our observation, that island nucleation occurs quickly, followed by coarsening, suggests an alternate origin of these two time scales. Specifically, it is possible that the mobile species responsible for slow downhill transport consists of material that detaches from islands. This material need not be chemically identical with the species arriving from the plume. Interestingly, we note that the prefactor reported here, $D_0 = 10^{-8\pm1}\text{cm}^2\ \text{s}^{-1}$, is five orders of magnitude lower than typical experimental and theoretical value for metal and semiconductor systems [63]. Similar diminished prefactors have previously been associated with correlated motion involving multiple atoms [63]. Here, it might be associated with stoichiometric

mass transfer of Sr-containing and Ti-containing species.

In summary, we have presented time-resolved x-ray reflectivity and diffuse scattering measurements obtained during PLD. Our results constitute direct observations of island nucleation as little as 200 ms after the pulse, and direct evidence of island coarsening occurring between laser pulses for temperatures as low as 695°C. Quantitative analysis of our results allow us to independently estimate the inter- and intra-layer diffusivity (prefactor and activation barrier) of mobile species between pulses and to place an upper bound on the ES barrier. Our measurements significantly impact prior estimates of the thermal diffusivity involved in $SrTiO_3$ growth, and place specific constraints on energetic smoothing mechanisms that have been proposed to occur during complex oxide PLD.

Acknowledgments

We thank Jack Blakely, Yongsam Kim, and David Muller for discussions, and Mark Tate for invaluable assistance. This work was supported by the Cornell Center for Materials Research (CCMR) with funding from the Materials Research Science and Engineering Center program of the National Science Foundation (cooperative Agreement 0520404) and by the National Science Foundation (DMR-0317729). Additionally, this work is based upon research conducted in part at the Cornell High Energy Synchrotron Source (CHESS), which is supported by the National Science Foundation and the National Institutes of Health/National Institute of General Medical Sciences under award DMR-0225180.

Experimental Details

For these experiments, a monochromatic (ΔE/E=1%) 10.0 keV x-ray beam with 8×10^{13} photons/sec/mm^2 was slit down to produce a 1.0 mm $\times$ 0.5 mm beam at the sample. The in-plane diffuse surface scattering was monitored using a CCD area detector operating as a linear detector in streak mode. The time resolution of the experiment is limited by both the readout time of the detector ($\approx$ 78 ms) and by the incident x-ray flux ($100 - 200$ ms). For these growth, we are able to collect 18 images between laser pulses. The depositions were performed by laser ablating a single crystal $SrTiO_3$ target using a 100 MW/cm^2 KrF excimer laser (248 nm). The target is located 6 cm from the substrate. The area of the laser spot on the target was approximately 3.7 mm^2 with a fluence of 1.9 J/cm^2. This configuration deposited $\approx$0.09 ML/pulse at a laser repetition rate of 0.2 Hz, with a 2×10^{-4} Torr partial pressure of O_2. The substrate temperature was measured using an optical pyrometer ($\lambda = 4.8-5.3\mu$m, emissivity=0.8). The substrate preparation procedure employed [41, 42] produced a TiO_2 terminated surface, and AFM confirmed the presence of single unit cell high steps separating large atomically flat terraces.

CHAPTER 4

THICKNESS DEPENDENCE ON SURFACE DIFFUSION IN EPITAXIAL LANTHANUM ALUMINATE ON STRONTIUM TITANATE

We now apply the results of the previous chapter to a heteroepitaxial materials system. The results of this chapter are in preparation to be submitted to *Physical Review Letters*[1]. We reproduce the article below with the abstract beginning in the first paragraph.

The $LaAlO_3/SrTiO_3\langle 001\rangle$ thin film materials system was studied using in situ, simultaneous x-ray diffuse scattering and specular reflectivity during pulsed laser deposition. Using this method, we are able to measure the time dependence of the characteristic surface length scale and the characteristic time for both in-plane and downhill diffusion. These data allow for the determination of the activation energy for various diffusion processes as a function of $LaAlO_3$ thickness. Additionally, we show that the downhill diffusion rate of the first monolayer is distinctly different than subsequent layers. These results are directly compared to previous experimental observations seen during the deposition of homoepitaxial $SrTiO_3\langle 001\rangle$.

Complex oxides possess a vast range of materials properties encompasing electrical insulators, high-T_c superconductors, semiconductors, dielectrics, ferromagnetics, and multiferroics. In the last six years, the $LaAlO_3/SrTiO_3\langle 001\rangle$ complex oxide system has received considerable attention due to the fascinating properties discovered at its interface [1, 18, 19, 64]. One interesting property of this system is

[1]Reprinted article with permission from: J.D. Ferguson, Y. Kim, A. R. Woll, and J.D. Brock, "Thickness dependence of surface diffusion in epitaxial $LaAlO_3$ on $SrTiO_3\langle 001\rangle$."

the presence of a conducting, quasi-two-dimensional electron gas at the interface of these two wide-bandgap insulating materials [1, 19, 64]. The formation of the conducting layer is highly dependent on the number of $LaAlO_3$ layers deposited [17], which has led to the possibility of new device architectures [21]. The deposition technique of choice for the $LaAlO_3/SrTiO_3$ system is pulsed laser deposition (PLD). While much attention has been given to the materials properties of this system, there is a lack of a fundamental understanding of the surface kinetics during PLD of $LaAlO_3$ on $SrTiO_3$. The ability to manipulate and understand the surface kinetics that occur during PLD is essential to controlling the interface roughness, the surface roughness, and the formation of defects. In this letter, time-resolved, simultaneous diffuse and specular x-ray scattering data are used to determine the rate of various surface diffusion processes during the PLD of $LaAlO_3$ on $SrTiO_3\langle 001\rangle$. We find that the barrier for in-plane diffusion of $LaAlO_3$ on $SrTiO_3$ is substantially larger than the rate-limiting barrier for downhill transport from an $LaAlO_3$ island to the $SrTiO_3$ substrate. Additionally, the diffusion energy barrier is measured as a function of $LaAlO_3$ film thickness, up to six unit cells.

We grew all films in the dual PLD/x-ray diffraction chamber in the G3 hutch and the Cornell High Energy Synchrotron Source (CHESS). The supplemental documents of Ref. [65] contain the experimental details. In this letter, A 1-D diode array detector (pixel size 0.125×5 mm) was used to acquire the diffuse scattering data at the quarter-Bragg position on the crystal truncation rod (CTR) with a 9.6 keV x-ray beam. An excimer laser, focused down to a 7.4 mm^2 spot, was used to ablate the single crystal $LaAlO_3$ target. The laser fluence was 1.6 J cm^{-2} for all films, producing a deposition flux of approximately twelve pulses-per-monolayer. Here, a monolayer (ML) refers to a one unit cell thick layer. The laser was fired at a repetition rate of 0.19 Hz. The substrate was held at controlled

temperatue in a background pressure of 7.5×10^{-6} Torr O_2. All films were grown in a layer-by-layer growth mode to a thickness of six MLs, which is well below the critical thickness for strain relaxation [66].

In layer-by-layer deposition, islands nucleate, grow in radius, and then begin to coalesce. At high coverage, the surface is best described by a series of pits that fill as more material is deposited. During deposition, a characteristic length scale L_{isl}, is present on the surface. This length scale is the result of correlations between island or pits, depending on the layer coverage, and is associated with the average distance between these surface features [32]. In our previous work we showed that, at low coverage, in situ x-ray diffuse scattering measures both L_{isl} and the characteristic time for in-plane (intra-layer) mass transfer, τ_{isl} [65]. Additionally, by monitoring the surface roughness using the specularly reflected x-rays, the characteristic diffusion time for downhill (inter-layer) transport, τ_{spec}, may be determined [28,29,34,38,65]. By combining τ_{isl} and τ_{spec} with the associated diffusion length, $L_d = L_{isl}/2$ (half the distance between islands or pits), the intra- and inter-layer diffusion rates may be calculated by invoking the Einstein relation: $D = L_d^2/4\tau$ [60].

The measured x-ray line shape contains both a specular component I_{spec}, and a diffuse component I_{diff}. These two components may be isolated by fitting the data to a sum of functions that take the form:

$$I(q_{||}) = I_0/[1 + \xi^2(q_{||} - q_0)^2]^{3/2}, \tag{4.1}$$

where $q_{||}$ is the in-plane scattering vector, and q_0 is the peak position [65]. For I_{diff}, q_0 is directly related to the distance between islands or pits by the equation: $q_0 \approx 2\pi/L_{isl}$ [48]. The behavior of I_{spec} and I_{diff} depends on the surface morphology. Specifically, during homoepitaxial layer-by-layer deposition, I_{spec} will

oscillate due to the continuous roughening and smoothening of the surface. Each local intensity maximum corresponds to the completion of ≈1 ML [34, 38, 65]. An interface is present in heteroepitaxial growth; therefore, reflected beams from the film surface and the film/substrate interface interfere, resulting in modulated intensity oscillations. These interference effects are known as "Kiessig" fringes, and their periodicity is dependent on the out-of-plane scattering vector, q_z [67]. For our scattering geometry, the envelope of I_{spec} has a periodicity of ≈4 MLs, and the roughness oscillations within this envelope have maxima corresponding to the completion of ≈1 ML.

To aid in the interpretation of the diffusely scattered x-ray intensity during heteroepitaxial deposition, we write the total in-plane surface scattering as:

$$I_{tot} = I_{spec} + I_{isl} + I_{sm}, \tag{4.2}$$

where I_{isl} is total diffuse scattering in the x-y plane[2], and I_{sm} accounts for scattering by features with correlations below our detection limit. Since our maximum measurable value of $q_{||}$ is $q_{max} \approx 0.2$ Å^{-1}, we are insensitive to scattering from surface features with correlations smaller than 31 Å. Consequently, if the coverage is low and the I_{spec} is constant, a time dependent I_{isl} results from mass transfer between islands with small correlations to islands measurable by our experiment. Therefore, I_{isl} is a direct measurement of the time scale for intra-layer mass transport [65]. We note that our experiments do not allow us to explicitly state which atoms/particles on the surface are determine the measured surface diffusion rates. Therefore, we shall generically refer to the rate-limiting diffusing species through-

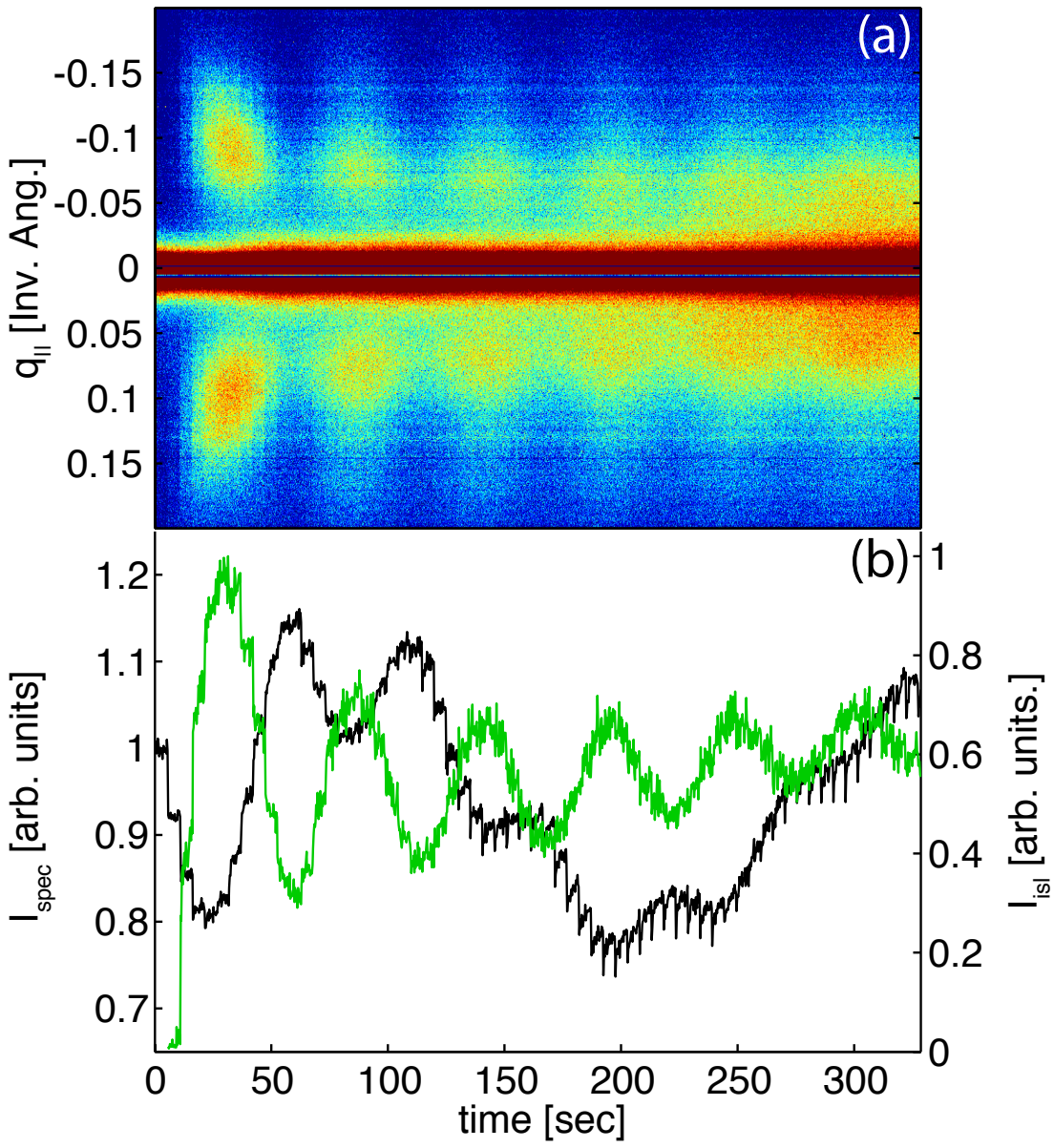

Figure 4.1: (a) X-ray scattering data for the PLD of $LaAlO_3$ on $SrTiO_3\langle 001\rangle$ at 781°C. The intensity measured at $q_{||} \neq 0$ is the diffuse x-ray scattering. The diffuse scattering is directly related to the $LaAlO_3$ island distribution. (b) The corresponding fit results for I_{spec} (black) and I_{isl} (green).

out this letter.

Figure 4.1(a) shows a false color image of the scattered x-ray intensity, as a function of time and $q_{||}$, during the deposition of six MLs of $LaAlO_3$ on $SrTiO_3$. Each 260-msec time slice, represents intensity vs. $q_{||}$ (see Ref. [65] for details). The intensity seen at $q_{||} \neq 0$ is a result of the Henzler ring of diffuse scattering [47] and, as mentioned above, the size and shape of this ring is determined by the $LaAlO_3$ island distribution on the surface [32]. As observed during PLD of homoepitaxial $SrTiO_3$ [65], q_0 decreases as each additional layer of the $LaAlO_3$ film is deposited, representing a systematic decrease in the island density with increasing layer number. To decompose I_{spec} and I_{isl}, each time slice is fit to our model; the results are shown in Fig. 4.1(b). In this figure, I_{isl} oscillates with the period of 1 ML, and is out of phase with I_{spec}. As discussed above, both the roughness and Kiessig components to I_{spec} are visible in Fig. 4.1(b). The periodicity seen in I_{spec} that is π out of phase with I_{isl} is the roughness component, and it results from the scattering of x-rays by the $LaAlO_3$ islands [59]. The minimum in the envelope of I_{spec} at around 200 seconds is a signature of the Kiessig component, therefore, the $^1/_4$ Bragg position sets a 4:1 ratio between the diffuse and Kiessig periods.

To examine the influence of temperature on the $LaAlO_3$ deposition, we show false color images of the scattering data obtained during the deposition of the first ML at 1000°C and 858°C in Figs. 4.2(a) and 4.2(b), respectively. Immediately noticeable in the data is the increase in q_0 as the surface temperature is decreased. This implies that the island density increaseds with decreasing temperature, consistent with classical nucleation theory. These data were fit to our model, and the

[2] I_{isl} is obtained by integrating the fit to the diffuse line, Eqn. 4.2, over the x-y plane: $I_{isl} = 2\pi \int_0^\infty q\, I_{diff}(q)\, dq$

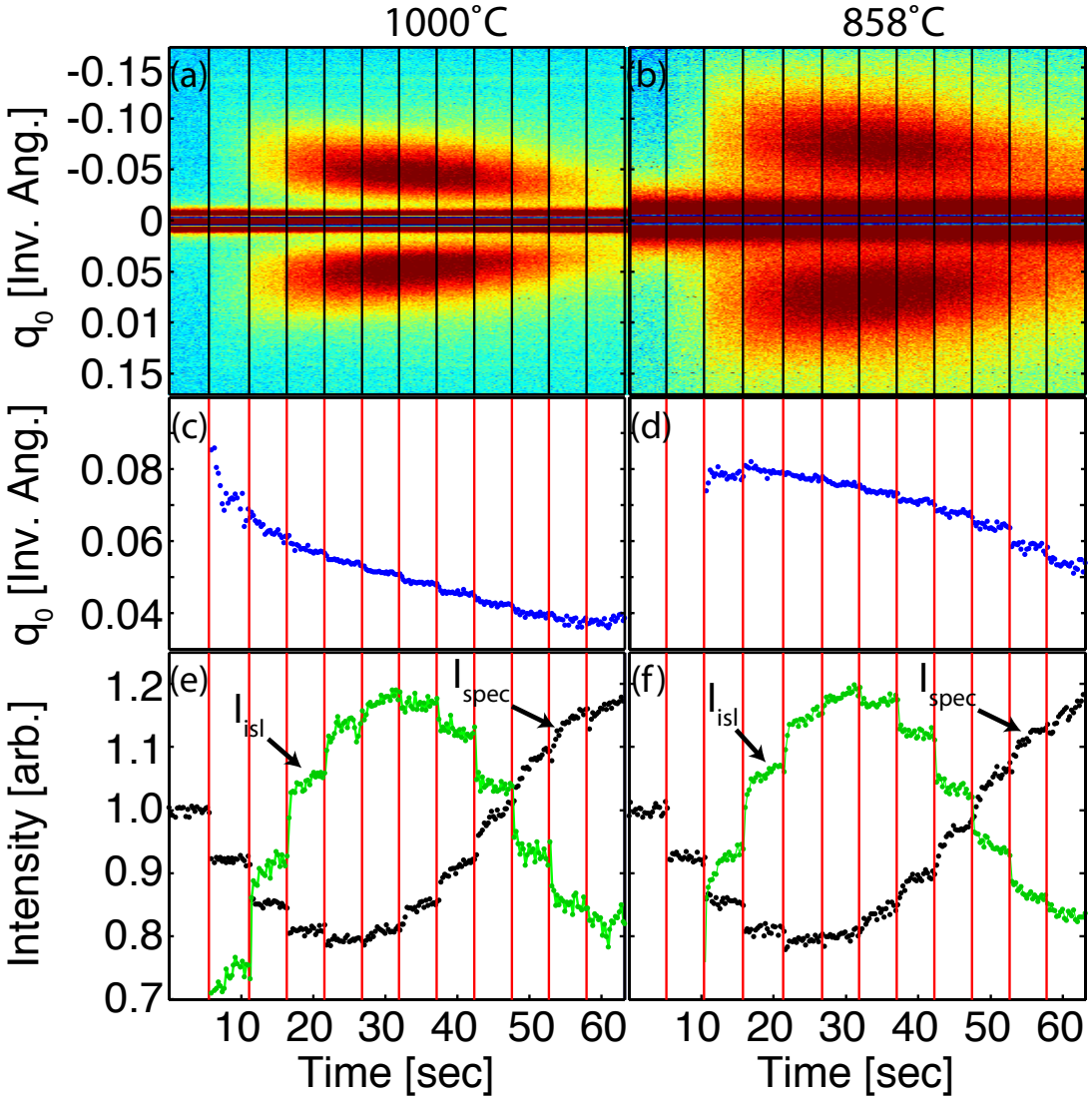

Figure 4.2: Diffuse scattering data and the corresponding fit results for the first ML of $LaAlO_3$ at 1000°C and 858°C. The vertical lines represent the times when the laser was fired. (a), (c) and (e) correspond to the 1000°C growth and (b), (d) and (f) show the 858°C results. The arrows annotate the data points used to determine τ_{isl} and τ_{spec}.

results are shown in Figs. 4.2(c)-4.2(f). As seen in Fig. 4.2(c), q_0 monotonically decreases both inter- and intra- pulse at 1000°C. This behavior is attributed to coarsening of the $LaAlO_3$ island distribution on the surface [32,57,65]. Fig. 4.2(d) shows q_0 for the 858°C deposition. At, and below, this temperature, the low diffuse intensity precluded an accurate fit before the second laser pulse. An interesting feature of Fig. 4.2(d) is the slight increase in q_0 just after the third laser pulse. The best fit estimates for the peak positions just before and after the third laser pulses are $q_0 = 0.078 \pm 0.001\text{Å}^{-1}$ and $q_0 = 0.081 \pm 0.001\text{Å}^{-1}$, respectively. This increase in q_0, as additional material arrives indicates an increase in island density. Therefore, island nucleation may be occurring up to this coverage at 858°C.

Figures 4.2(e) and 4.2(f) show I_{spec} and I_{isl} for the data presented in Figs. 4.2(a) and 4.2(b), respectively. Following the third laser pulse, a constant I_{spec} accompanies the slow rise in I_{isl}. As discussed previously, this temporal dependence of I_{isl} corresponds to the timescale for in-plane mass transfer. Additionally, the time dependence of I_{spec} at high coverage is a direct measurement of the timescale for downhill diffusion. Fitting both I_{isl} and I_{spec} to a simple exponential function allows for the determination of these characteristic diffusion times.

Conceptually, the deposition of the first layer in heteroepitaxy is distinctly different than deposition of subsequent layers. For example, the diffusion rate for $LaAlO_3$ species on the $SrTiO_3$ substrate need not be the same as diffusing $LaAlO_3$ species on the $LaAlO_3$ film. Additionally, a mobile species diffusing on top of the first $LaAlO_3$ ML might interact with the $SrTiO_3$ substrate during downhill diffusion. Therefore, one might expect a film thickness dependence of the diffusion rate until the $LaAlO_3$ film reaches a critical thickness for substrate interaction effects. To examine this possibility, the inset to Fig. 4.3 shows a plot of L_d^2 vs.

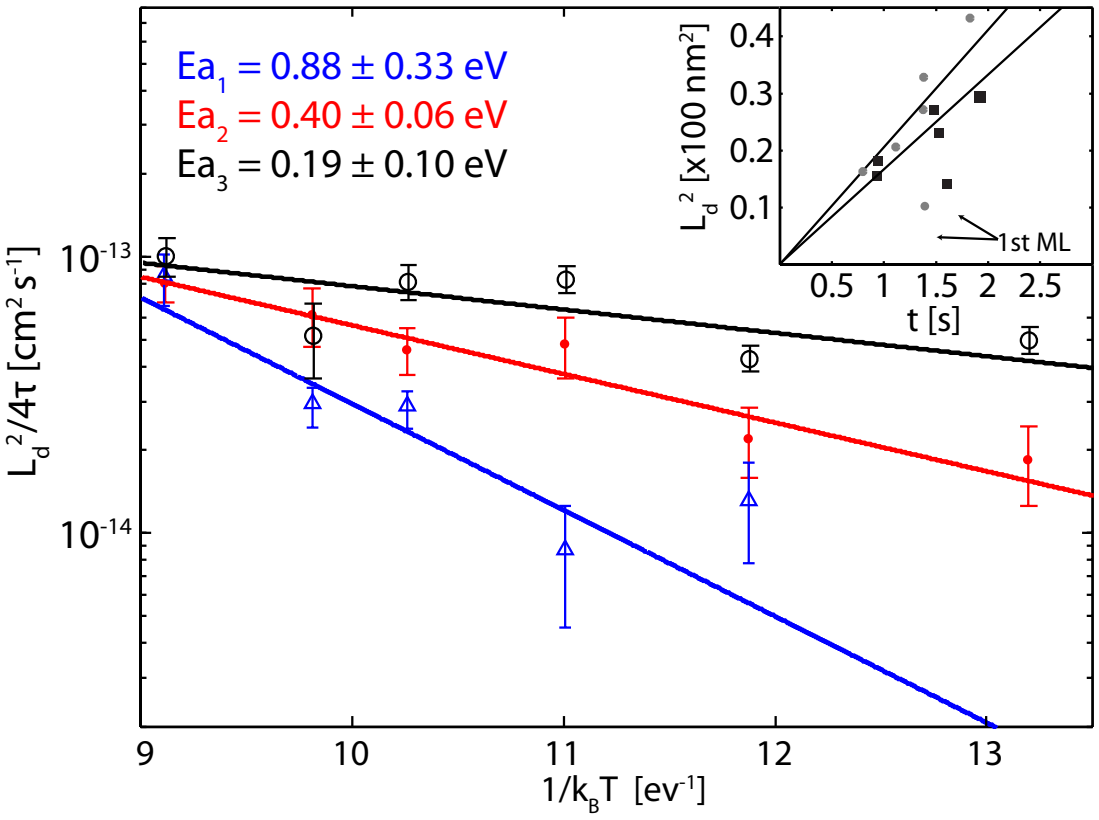

Figure 4.3: Arrhenius plot of the diffusion rate for $LaAlO_3$ species during three different processes: in-plane diffusion on the $SrTiO_3$ substrate (blue, triangles), downhill diffusion from the first $LaAlO_3$ ML to the substrate (red, points), and downhill diffusion from a $LaAlO_3$ ML to the $LaAlO_3$ film (black, circles). The inset shows the dependence of L_d on τ_{spec} for each ML at 704°C (squares) and 606°C (circles). The arrows point to the data points for the first MLs.

τ_{spec} for each of the 6 ML deposited at two substrate temperatures: 606°C and 704°C. We note that after the first ML, L_d^2 and τ_{spec} show a linear relationship, where the slope of the line is related to the diffusion rate by: $L_d^2 = 4D\tau_{spec}$. The fact that the first data point is inconsistent with the remaining points suggests that the interlayer transport for the first layer is distinctly different than that of

subsequent layers.

To further examine the diffusion behavior in the $LaAlO_3$ films, an Arrhenius plot is shown in Fig. 4.3 for three data sets: the intra-layer diffusion rate for the first ML, the inter-layer diffusion rate for the first ML, and the average of the inter-layer diffusion rates in the second through sixth MLs. The intra-layer diffusion barrier for $LaAlO_3$ species on $SrTiO_3$ was determined to be $E_{a1} = 0.88 \pm 0.33$ eV. The noise in I_{isl} precluded the determination of τ_{isl} for subsequent MLs, therefore, the intra-layer diffusion rate for $LaAlO_3$ species on $LaAlO_3$ could not be measured. Fitting the inter-layer diffusion data to an Arrhenius model yielded activation energies of $E_{a2} = 0.40 \pm 0.06$ eV and $E_{a3} = 0.19 \pm 0.10$ eV for the first ML and second-sixth ML, respectively. These data illustrate the layer dependence of the activation barrier, showing that the largest energy barrier corresponds to the diffusion of $LaAlO_3$ species on the $SrTiO_3$ substrate.

The various diffusion processes measured from our data are presented schematically in Fig. 4.4. The diffusion barrier, E_{a1}, corresponds to in-plane mass transfer of $LaAlO_3$ species on the $SrTiO_3$ substrate. The activation barrier, E_{a2}, corresponds to the inter-layer diffusion from the top of the first $LaAlO_3$ layer down to the substrate. E_{a3} corresponds to the downhill diffusion of the second-sixth MLs to the underlying $LaAlO_3$ layer. Our measurements do not allow us to determine if the inter-layer activation barriers are the Ehrlich-Schwoebel (ES) barrier, the surface diffusion barrier, or the sum of the two.

Our results explicitly demonstrate the contrast between heteroepitaxial and homoepitaxial diffusion processes. Specifically, previous work measuring diffusion rates for PLD of homoepitaxial $SrTiO_3$ showed that the energy barriers for inter- and intra-layer diffusion were the same: $E_a = 0.97 \pm 0.07$ eV [65]. It was also

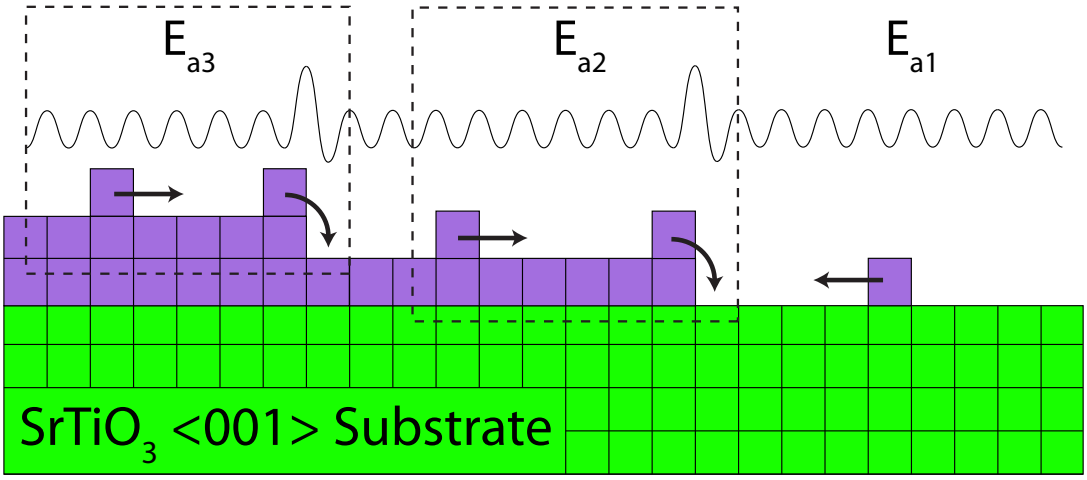

Figure 4.4: Schematic description of the activation barriers measured in Fig. 4.3. The oscillations show the various activation energies across the surface, with the large increase at the step edge representing the ES barrier. E_{a1} is the in-plane diffusion barrier for $LaAlO_3$ species on the substrate. E_{a2} is the energy barrier for $LaAlO_3$ species diffusing down to the $SrTiO_3$ substrate. E_{a3} represents the downhill activation barrier for layers 2-6. The dotted outline illustrates which set of diffusion processes determine E_{a2} and E_{a3}.

shown that the inter-layer diffusion rate is the same for all MLs during $SrTiO_3$ homoepitaxial deposition (see Fig. 3 of ref. [65]). Here, the measured intra-layer diffusion barrier of the first $LaAlO_3$ ML is found to be larger than the downhill activation barrier. Additionally, the inter-layer diffusion of the first ML of $LaAlO_3$ on $SrTiO_3$ was found to differ from subsequent layers, illustrating a distinct difference between homoepitaxy and heteroepitaxy.

Our data may be used to explain the persistent layer-by-layer growth mode for the $LaAlO_3/SrTiO_3$ depositions. To do this, it is useful to consider the Volmer-Weber (3D) growth mode. In Volmer-Weber growth, the lower diffusion barrier of the film/substrate interface, when compared to the film/film diffusion barrier,

results in the sticking of adatoms to the top of nucleated islands. This behavior has been seen in Fe_3Si growth on GaAs$\langle 001 \rangle$, where the growth mode was directly correlated to the surface diffusion barriers [68]. For $LaAlO_3/SrTiO_3$, $E_{a1} > E_{a2}$, providing the proper condition for inter-layer transport, a prerequisite for layer-by-layer growth. Therefore, diffusing species will tend to absorb to the substrate rather than the film. Additionally, this physical description may be applied to the deposition of the second ML of $LaAlO_3$, since $E_{a2} > E_{a3}$.

In conclusion, we have shown that simultaneous, time-resolved surface diffuse and specular scattering can be used to measure the surface diffusivity during the pulsed laser deposition of $LaAlO_3$ on $SrTiO_3\langle 001 \rangle$. We have used this data to measure energy barriers for three different surface diffusion processes: in-plane diffusion of $LaAlO_3$ on $SrTiO_3$, downhill diffusion of $LaAlO_3$ to the $SrTiO_3$ substrate, and downhill diffusion of $LaAlO_3$ to the $LaAlO_3$ film. The activation barriers were found to decrease, respectively, for each of these processes, which was used to explain the persistent layer-by-layer growth mode. Additionally, we have shown that all diffusion barriers for $LaAlO_3$ on $SrTiO_3$ are small compared to homoepitaxial $SrTiO_3$.

Acknowledgments

We would like to thank D. Muller, D. Schlom, and D. Dale for useful conversations. This work was supported in part by the National Science Foundation (NSF) (DMR-0705361) and in part by the Cornell Center for Materials Research (CCMR) with funding from the Materials Research Science and Engineering Center program of the National Science Foundation (cooperative agreement DMR-0520404) and is based upon research conducted at the Cornell High Energy Synchrotron Source

which is supported by the NSF and the National Institutes of Health/National Institute of General Medical Sciences under NSF award DMR-0225180.

CHAPTER 5

EPITAXIAL OXYGEN GETTER FOR A BROWNMILLERITE PHASE TRANSFORMATION IN MANGANITE FILMS

We now use in-situ x-ray scattering to monitor the phase transformation of a buried layer in a complex oxide heterostructure. These results were submitted to *Advanced Materials*.[1] We reproduce the submitted article below, beginning in the first paragraph with the article abstract.

Complex oxide systems are promising candidates for materials in solid oxide fuel cells, oxygen sensors, and other applications requiring oxygen anion diffusion. [25, 69, 70] In particular, mixed mode conductors such as the manganite oxides, have been of much interest as cathode materials for solid oxide fuel cells. [23,25,71] One interesting property of some complex oxides is their ability to form distinct, oxygen-deficient ordered phases with high ionic conductivity. [69, 72–74] Here, we report the discovery, using in situ synchrotron-based x-ray techniques, of a new method for creating oxygen vacancy ordered phases in epitaxial manganite thin films. The method involves depositing an oxygen deficient complex oxide film on top of a stoichiometric manganite film to act as an oxygen getter. Once the getter layer exceeds a critical thickness, a phase transition to an oxygen vacancy ordered superlattice occurs in the manganite film. We demonstrate the use of oxygen deficient $SrTiO_{3-\delta}$ (STO) and $LaAlO_{3-\delta}$ (LAO) as getter layers and superlattice formation in four manganite systems: $La_{0.7}Sr_{0.3}MnO_3$ (LSMO), $Pr_{0.7}Ca_{0.3}MnO_3$ (PCMO), $La_{0.7}Ca_{0.3}MnO_3$ (LCMO), and $LaMnO_3$ (LMO). The superlattices may

[1]Reprinted article with permission from: J.D. Ferguson, Y. Kim, L Fitting Kourkoutis, A. Vodnick, A. R. Woll, D. A. Muller, and J.D. Brock, "Epitaxial Oxygen Getter for a Brownmillerite Phase Transformation in Manganite Films," submitted to *Advanced Materials*.

be maintained at ambient conditions if quenched to room temperature following growth. This growth technique constitutes a new procedure for preparing such structures, and may lead to the discovery of new, technologically diverse phases of complex oxide materials that cannot be grown by traditional deposition techniques.

Reflected high energy electron diffraction (RHEED) and x-ray scattering are commonly employed to monitor thin film thickness, roughness, morphology, and structure during deposition. [43, 51, 65, 75–77] The penetrating power of x-rays makes them uniquely suited for structural studies of the buried layers in heterostructures. To monitor film thickness during deposition, the intensity at surface-sensitive, anti-Bragg positions may be monitored in real time. [34, 38, 52] During homoepitaxial, layer-by-layer growth, this intensity oscillates with the period corresponding to the deposition of 1 unit cell, hereafter referred to as a monolayer (ML). For heteroepitaxial growth, the anti-Bragg intensity oscillates with a period of either 1 or 2 MLs, depending on the details of the system. [52, 67] Here, we use this method by measuring the intensity of specularly reflected x-rays at the $(0\frac{1}{2}0)$ position on the crystal truncation rod of the substrate ([010] is the surface normal).

The Anti-Bragg intensity measured during the pulsed laser deposition (PLD) of a LSMO/STO/LAO heterostructure on $SrTiO_3\langle 010\rangle$ is shown in Fig. 5.1a. The oscillations during the LSMO deposition are shown in green, and the time between local maxima corresponds to deposition of 1 ML. The [21.2 ML] LSMO film was grown in 100 mTorr of O_2 so that the film is (nearly) fully oxygenated. Next, approximately 6 MLs of oxygen deficient STO were deposited on top of the LSMO. The intensity oscillations corresponding to the STO deposition are shown in red. The oxygen deficient STO was deposited in 1×10^{-5} Torr of O_2. Low angle annular

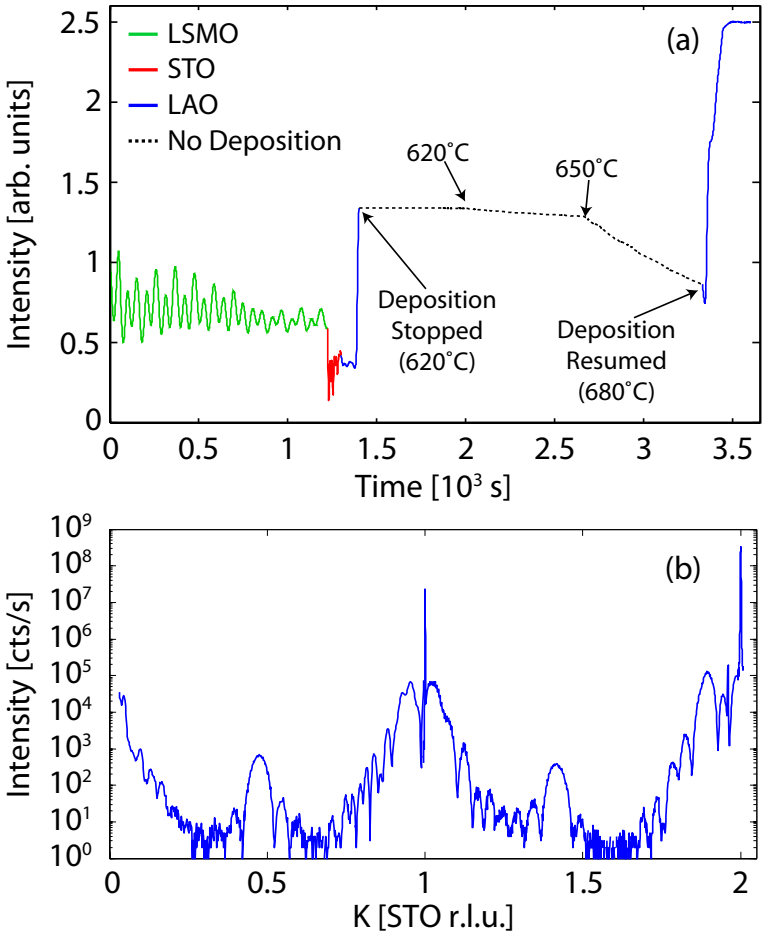

Figure 5.1: a) Anti-Bragg intenisty oscillations for the deposition of a LSMO/STO/LAO heterostructure. The large intensity increase during the LAO deposition is the result of a Bragg peak forming due to oxygen vacancy ordering in the buried LSMO film. b) The post deposition x-ray reflectivity.

dark field scanning transmission electron microscopy (STEM) of films grown under these conditions [in our PLD system] show that the resulting strain fields are similar to those reported previously, [78] confirming that the films are oxygen deficient. The film was then capped with LAO (blue line), again in 1×10^{-5} Torr of O_2. After $\approx$ 6MLs of LAO are deposited, the intensity increases abruptly. As shown below, the sharp rise in intensity is due to the formation of a superlattice, resulting in a

Bragg reflection near the $(0\frac{1}{2}0)$. Subsequent diffraction and microscopy measurements demonstrate that the superlattice forms in the buried LSMO film, rather than in the capping layer(s) or the bulk STO substrate.

As illustrated in Fig. 5.1a, the formation of the superlattice is dependent upon the continuous deposition of LAO. When the deposition of the LAO is halted, the superlattice formation ceases and the intensity remains constant. If the sample is then heated, the intensity begins to decrease. When the LAO deposition is resumed, the intensity begins to rise again, until approximately 3600 s. At this point, the intensity saturates. As discussed below, we interpret this saturation as corresponding to near-complete conversion of the LSMO layer from its as-deposited form to the new phase. Following the deposition, the sample was cooled in vacuum to room temperature in $\approx$1.5 hours.

The superlattice structure was determined by ex situ x-ray specular reflectivity. The specular intensity is plotted as a function of STO reciprocal lattice units (r.l.u.) in Fig. 5.1b. In addition to sharp (010) and (020) Bragg peaks from the STO substrate, thin-film peaks and Kiessig thickness fringes are clearly visible. Fitting the $(0\frac{1}{2}0)$ region to a simple finite-size line-shape, we obtain a perioditicy of 8.2 Å and a film thickness of 77.5 Å. This thickness is about three LSMO unit cells less than the thickness obtained by counting the number of LSMO growth oscillations, suggesting that most, but not all of the LSMO is transformed. The observed thickness is not consistent with either the STO or the LAO layers. Thus, we conclude that the $\frac{1}{2}$-order peak corresponds to a superlattice in the LSMO layer.

We note that, because the superlattice forms in a buried layer rather than the surface, the transition beginning at $t \approx 1400$ s would not have been observed using conventional RHEED, which probes only the near surface region. [30] Thus, x-ray

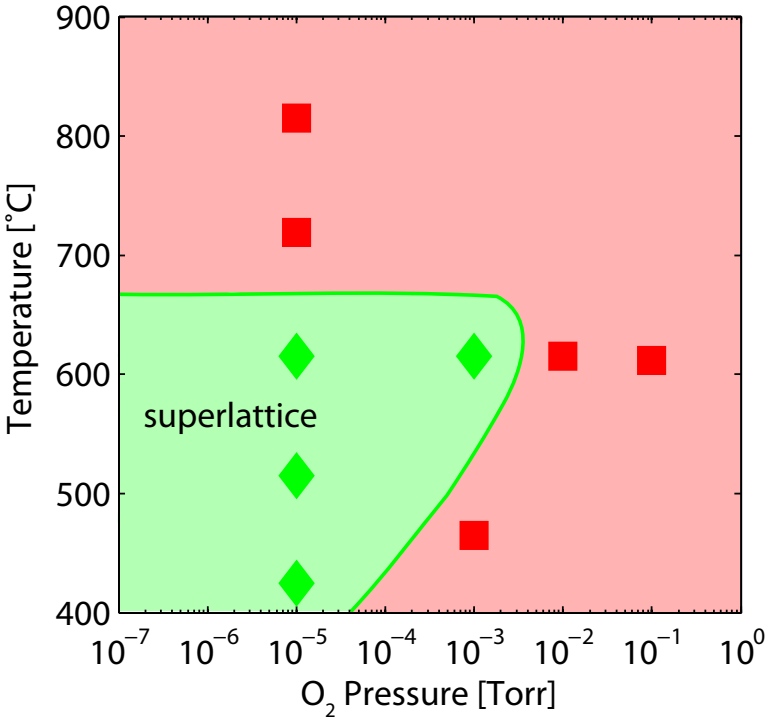

Figure 5.2: Phase diagram for the deposition condition of the STO getter layer used to induce a superlattice formation. The green region (diamonds) illustrates the pressure/temperature regime where the LSMO phase transforms into a superlattice, while no phase transform occurs in the red region (squares).

scattering was critical for identifying this transition.

The superlattice shown in Fig. 5.1 was formed with both oxygen deficient LAO and STO as capping layers; however the transformation may also be induced using only one film of either LAO or STO. To further investigate the conditions required to form the superlattice, a series of identical LSMO films were grown (615°C, 100 mTorr O_2) and capped with STO, grown under varying conditions. The results are shown in Fig. 5.2. In this phase diagram, the green region represents the pressure/temperature regime where a getter layer induces the superlattice phase transition. The boundaries in the phase diagram represent approximate midpoints

between data points. The superlattice forms at temperatures as low as 415°C in 1×10^{-5} Torr of O_2 and as high as 615°C in 1 mTorr of O_2.

In addition to the growth conditions for the capping layer indicated in Fig. 5.2, two additional conditions are necessary to form and stabilize this type of buried superlattice structure in the LSMO film:

1. The LSMO film must be grown under oxygen rich conditions, presumably to form a (nearly) stoichiometric layer. LSMO films deposited in 1×10^{-5} Torr O_2, followed by the deposition of the getter layer, do not exhibit superlattice peaks.

2. After growth, increasing the partial pressure of oxygen while still at growth temperature destroys the superlattice within seconds. Thus, the post-deposition anneal in oxygen frequently applied to oxide films eliminates the structure.

To examine the nature of the superlattice, Fig. 5.3a shows a STEM image of the film grown in Fig. 5.1. The high-angle annular dark field STEM image clearly shows a superlattice of dark planes in the LSMO layer, confirming the x-ray measurements. These dark planes coincide with the position of MnO_2 layers in a stoichiometric LSMO film, suggesting that the film is either manganese or oxygen deficient. These low density planes appear in the LSMO film with a period of 2 perovskite unit cells. Since the superlattice structure is highly dependent upon the oxygen partial pressure (see Fig. 5.2), and annealing in a high oxygen environment destroys the superlattice, we conclude that the dark planes result from missing oxygen rather than missing manganese cations. Evidently, since the phase transition occurs during deposition of an oxygen-deficient over layer, the formation of the structure is driven by oxygen diffusion from the LSMO film into

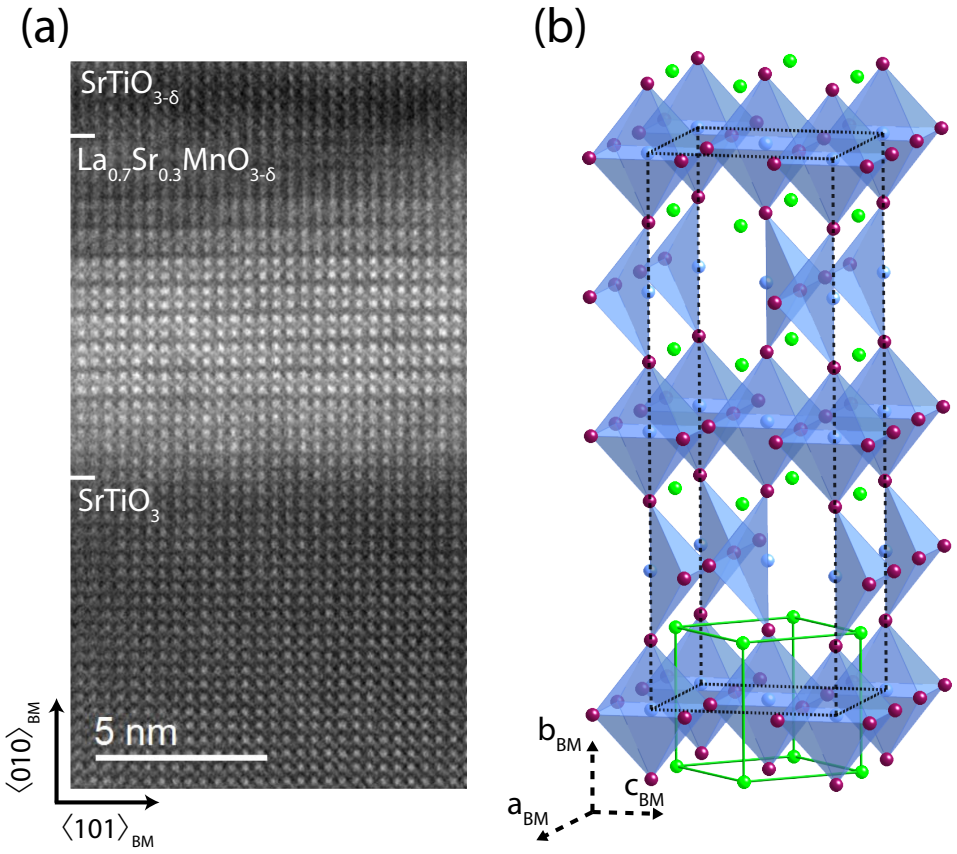

Figure 5.3: a) Scanning transmission electron microscopy image of the film grown in Fig. 5.1. The oxygen vacancies have ordered into a brownmillerite type structure. b) The idealized brownmillerite unit cell, $ABO_{2.5}$, with the corresponding perovskite unit cell shown in green. A site atoms are green spheres, B site blue spheres, and oxygen atoms are shown as red spheres.

the capping layer. Therefore the capping layer is acting as an oxygen getter. This picture is consistent with the results of Takahashi et al. [79], in which $LaAlO_3$ and $LaTiO_3$ overlayers were shown to remove oxygen from a buried anatase TiO_2 layer on STO. They found that oxygen gettering decreased the ordering in their system. In contrast, in this case, oxygen gettering results in increased ordering in the manganite layers.

Fig. 5.3a strongly resembles other high resolution STEM images of brownmillerite systems. [80,81] The brownmillerite family of crystal structures is associated with oxygen vacancy ordering in a perovskite lattice. [80–82] The idealized brownmillerite crystal structure is orthorhombic, has space group Pcmn, and is shown in Fig. 5.3b with the corresponding cubic perovskite unit cell outlined in green. [73,83] The two unit cells are rotated 45° from each other, and the cell parameters are related by: $a_{BM} = c_{BM} \approx \sqrt{2}a_{PV}$ and $b_{BM} \approx 4a_{PV}$. In this notation, the surface normal is in the [010] direction, the BM subscript refers to the brownmillerite crystal system, and the PV subscript refers to the perovskite crystal system.

The brownmillerite structure has BO_6 octahedra at the unit cell corners, with the oxygen vacancies ordering into missing rows oriented in the $[100]_{BM}$ direction, causing the unit cell to alternate between oxygen octahedra and oxygen tetrahedral centered on the B cation sites. The missing rows of oxygen are shifted by a half unit cell in the c_{BM} direction for each half unit cell translation in the b_{BM} direction. Small rotations of the oxygen tetrahedra and octahedra can further distort the unit cell. Many of the resulting variants of the brownmillerite structure have been reported in bulk $La_{1-x}Sr_xMnO_3$ samples. [82] The $(110)_{BM}$ Bragg peak corresponds approximately to $(\frac{1}{2}\frac{1}{4}\frac{1}{2})_{PV}$ — the difference is due to the lattice mismatch between the STO substrate and LSMO. Ex situ x-ray diffraction measurements (not shown) exhibit a weak reflection near $(\frac{1}{2}\frac{1}{4}\frac{1}{2})_{PV}$ with fourfold rotation symmetry about the surface normal, strongly supporting the brownmillerite structure. The measured out-of-plane lattice parameter is $b_{BM} = 16.47 \pm 0.01$ Å. Since the in-plane lattice parameters are locked to the STO substrate, the measured lattice constant should not be identified as the equilibrium value.

To investigate the applicability of this growth technique to other material systems, heterostructures were grown with LSMO, PCMO, LCMO, and LMO. The intensity oscillations during the deposition of these heterostructures are shown in Fig. 5.4a. The deposition of the $AMnO_3$ films are represented with a white background, while the dark background represents the deposition of a STO getter layer. The growth temperatures of the $AMnO_3$ films were 615°C, 850°C, 615°C, and 830°C for the LSMO, PCMO, LCMO, and LMO, respectively. All four $AMnO_3$ films where grown to a thickness of ≈20 MLs, with a background oxygen pressure of 100 mTorr for the LSMO, PCMO, and the LCMO. The LMO film was grown at 300 mTorr O_2. For each heterostructure, the STO getter layer was deposited at 615°C in 1×10^{-5} Torr of O_2. All the manganite materials investigated exhibited the dramatic increase of the anti-Bragg intensity. After cooling to room temperature, ex situ x-ray reflectivity measurements on all four samples (Fig. 5.4b) exhibit the $(0\frac{1}{2}0)$ superlattice peak. The LMO film shows an additional peak near $(0\frac{3}{4}0)$, indicating a further reduction in symmetry.

An interesting feature seen in Fig. 5.4a is that the phase transition occurs at approximately the same getter layer thickness (≈ 12 MLs) for all $AMnO_3$ films. A possible explanation for this critical thickness is that the number of oxygen vacancies must reach a critical density to induce the transition. Specifically, if the oxygen affinity of the capping film is larger than that of the manganite layer, one would expect oxygen to diffuse into the getter throughout the deposition, which is consistent with Takahashi, et al. [79] Although no vacancy ordering was found in their system, it was shown that oxygen was removed for getter layers grown as thin as 1 unit cell. Additionally, since STO did not act as a getter, the difference in oxygen affinity was determined to be the diffusional driving force, rather than an energetic effect due to PLD. Our data alone does not allow us to determine

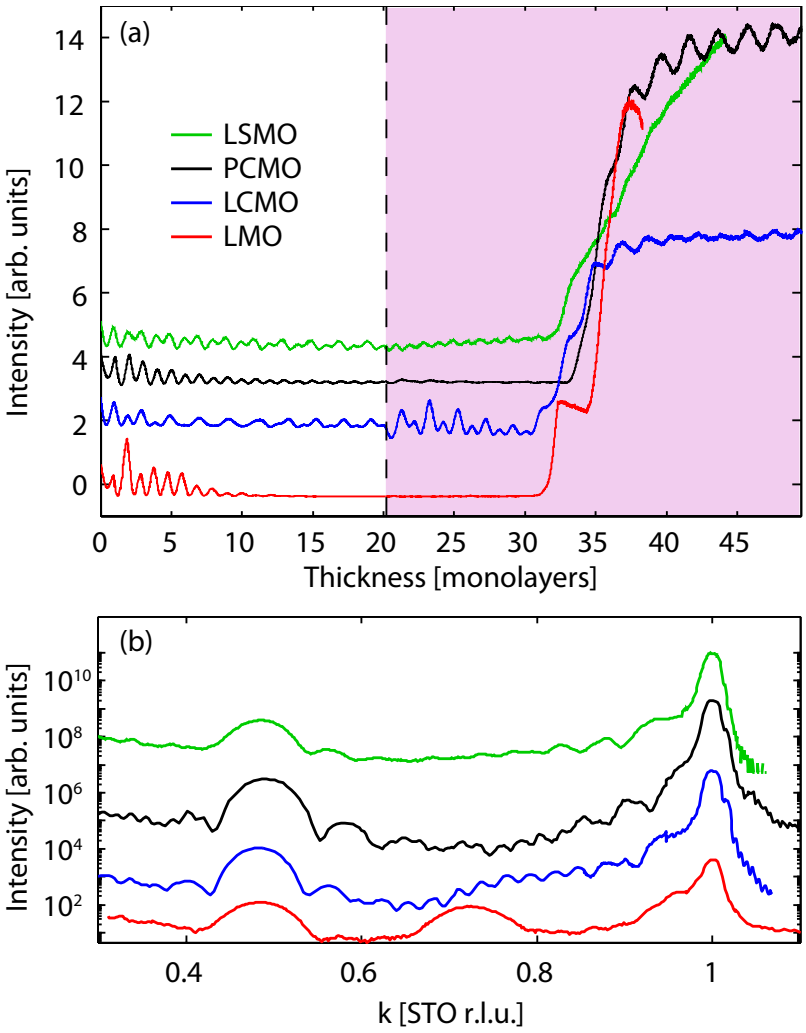

Figure 5.4: a) Anti-Bragg intensity oscillation for the deposition of four manganite films (white region), followed by the deposition of a STO getter layer (colored region). All four films show the sharp intensity increase associated with the superlattice formation. b) The x-ray reflectivity for each film.

if the diffusion of oxygen is occurring throughout the getter layer deposition or if diffusion begins when the phase transition occurs at $\approx$ 12 MLs. Additionally, we note that the multiple valence states of manganese does allow for oxygen vacancies to form while still preserving the charge neutrality of the film. This property may

be a prerequisite for using a getter layer to induce a perovskite to brownmillerite phase transition.

Our data also exemplifies the difficulty of growing stoichiometric, ABO_3 complex oxide heterostructures. Specifically, if a layer is grown oxygen deficient, the difference in affinity may drive the inter-diffusion of oxygen between adjacent layers. Therefore, the commonly used post deposition anneal in a high oxygen environment may be necessary to assure that all films in the heterostructure are fully oxygenated.

In conclusion, we have shown that an epitaxial oxygen getter layer can be used to induce an oxygen vacancy ordered superlattice in buried manganite films and have tentatively identified the superlattice structure as a brownmillerite crystal phase. The phase transition is mediated by the diffusion of oxygen from the buried film into the getter layer, presumably due to a difference in oxygen affinity. The process is demonstrated with LSMO, PCMO, LCMO, and LMO. A growth phase diagram for superlattice formation is presented for LSMO. The large temperature/pressure regime where the superlattice formation occurs exemplifies the difficulty of growing stoichiometric phases in oxide heterostructures. While we demonstrated this technique for manganite films, the method may be applicable to other materials systems and lead to the discovery of new, useful phases of complex oxide materials. Finally, this work clearly demonstrates the utility of real-time x-ray structural studies during thin film deposition.

Acknowledgments

We thank R. Chopdekar, D.S. Dale, M. Liberati, R. Misra, B. Nelson-Cheeseman, P. Schiffer, D. Schlom and Y. Suzuki for their help with this work. This work was supported in part by the National Science Foundation (DMR-0705361) and in part by the Cornell Center for Materials Research (CCMR) with funding from the Materials Research Science and Engineering Center program of the National Science Foundation (cooperative agreement DMR-0520404) and is based upon research conducted at the Cornell High Energy Synchrotron Source (CHESS) which is supported by the National Science Foundation and the National Institutes of Health/National Institute of General Medical Sciences under NSF award DMR-0225180.

Experimental Details

All thin films were grown by PLD using a KrF excimer laser (248 nm) at a repetition rate of 1 Hz. The target was 6 cm from the substrate. The substrate temperature was measured using an optical pyrometer (λ=4.8-5.3μm, ϵ=0.8). To regulate the O_2 pressure, oxygen was inserted into the chamber atmosphere. The laser spots size on the target was 7.4 cm^2 for all films, with a fluence of 1.2 J cm^{-2} for the LSMO, PCMO and LCMO films. The laser fluence was 1.6 J cm^{-2} for LMO. The STO and LAO getter layers were deposited with a fluence of 0.8 J cm^{-2} and 1.6 J cm^{-2}, respectively. All films were grown on $SrTiO_3\langle 010\rangle$ substrates, prepared to have TiO_2 terminated surfaces [42] and AFM ensured the substrates had unit cell high steps separated by large terraces. The depositions were performed in the PLD/x-ray diffraction system in the G3 experimental hutch at CHESS. The x-ray

reflectivity shown in Fig. 5.1b was performed at the G2 hutch ($\Delta E/E = 0.2\%$), while the data shown in Fig. 5.4b was collected at G3($\Delta E/E = 1.5\%$).

CHAPTER 6

CONCLUSION

6.1 Summary

The research presented in this thesis provides an in-depth understanding of many physical mechanisms operant during pulsed laser deposition of complex oxide thin films. In Chapter 1 and Appendix A, we outlined our method to produce atomically flat, single surface terminated $SrTiO_3\langle 001\rangle$ substrates. In Chapter 3, we presented simultaneous surface diffuse and specular x-ray scattering measurements on a model homoepitaxial system: $SrTiO_3\langle 001\rangle$. These measurements revealed that island coarsening was a pervasive mechanism during PLD. Additionally, we measured the surface length scale as a function of time, during growth. Combining this length scale with the characteristic surface relaxation time constant we calculated the diffusion rates for both inter- and intra-layer transport.

Next, we applied the method of surface diffuse and specular x-ray scattering during PLD to a heteroepitaxial system: $SrTiO_3\langle 001\rangle/LaAlO_3$. These data were presented in Chapter 4. This method allowed us to measure the activation energy for surface diffusion as a function of $LaAlO_3$ thickness. Specifically, we were able to measure energy barrier for three distinct processes: in-plane diffusion of $LaAlO_3$ species on the $SrTiO_3$ substrate, downhill diffusion of $LaAlO_3$ species from the top of the first monolayer to the $SrTiO_3$ substrate, and downhill diffusion of the subsequent monolayers of $LaAlO_3$ species to the $LaAlO_3$ film. We showed that the downhill diffusion barriers are significantly less than the diffusion barrier for $LaAlO_3$ on $SrTiO_3$, which promotes layer-by-layer growth.

In Chapter 5 we shifted away from fundamental PLD studies. Here, we used the penetrating power of x-rays to probe the structural phase transition of buried manganite films to an oxygen vacancy ordered superlattice. The phase transition was driven by the diffusion of oxygen from the manganite layer into an epitaxial over layer. This transition was demonstrated with four manganite compounds: $La_{0.7}Sr_{0.3}MnO_3$, $Pr_{0.7}Ca_{0.3}MnO_3$, $La_{0.7}Ca_{0.3}MnO_3$ (LCMO), and $LaMnO_3$.

While the the work here has contributed tremendously to the fundamental understanding of PLD, our results have also inspired additional ideas for other experiments. We outline these experiments in Section 6.2.

6.2 Future Directions

Our work in Chapters 3 and 4 revealed that coarsening is a fundamental mechanism in PLD. Of the various types of coarsening mechanism known [32, 57, 58, 84–87], the most common in epitaxial systems is Ostwald ripening [87]. The ripening mechanism may be determined by examining at the asymptotic dependence of the surface length scale, L_{isl}. For Ostwald ripening, the dynamic scaling law $L_{isl} \propto t^n$ applies, where t is time and n is the scaling exponent. Ostwald ripening is typically characterized as being in one of two regimes: attachment limited or diffusion limited coarsening kinetics [32]. In attachment limited Ostwald ripening, an extra barrier for an atom to attach to an existing island is the rate limiting mechanism and the scaling exponent is given by $n = {}^1/_2$. If there is no barrier for an adatom to attach to islands, the ripening is considered diffusion limited, and the scaling exponent is $n = {}^1/_3$.

Diffuse scattering measurements are ideal for measuring late-time coarsening

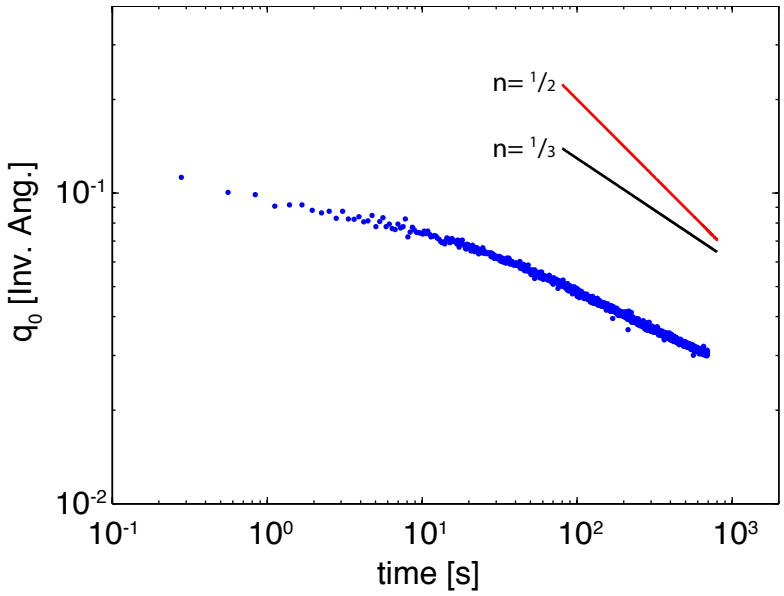

Figure 6.1: Late time behavior of q_0 for homoepitaxial $SrTiO_3\langle 001\rangle$. The surface coverage is ≈0.3 MLs. For reference, the lines for n=$-1/2$ and n=$-1/3$ are shown.

kinetics during PLD. Specifically, since the peak position of the diffuse scattering, q_0, is a direct measurement of the characteristic surface length scale ($L_{isl} \approx 2\pi/q_0$), the asymptotic scaling law becomes: $q_0 \propto t^{-n}$. Fig 6.1 shows a data set for the late time behavior of q_0 in homoepitaxial $SrTiO_3\langle 001\rangle$. For this data, the laser was fired three times at 50 Hz. Each laser pulse delivered approximately 0.1 MLs. The surface was then monitored using diffuse x-ray scattering. Since q_0 is decreasing continuously and no material is being added to the system, we conclude that the decreasing value of q_0 is the direct result of island coarsening.

Interestingly, two different regimes are visible in Fig. 6.1. For reference, the scaling exponents for both diffusion limited and attachment limited coarsening kinetics are plotted in the upper right corner, and neither exponent accurately describes the data. Additionally, preliminary analysis [not shown here] demonstrates that the line shapes are not self similar until ≈ 300 seconds, and therefore scaling

analysis should not be applied at early time, during PLD. This thesis address the early time behavior, and future experiments could address the late time scaling behavior of PLD. The data presented in Fig. 6.1 suggests that there may be two time regimes. An initial transient state may be due the the large supersaturation, caused by the 50 Hz repetition rate, producing an unusually high nucleation density compared to typical growth conditions. For future experiments on late time coarsening, this experiment should be performed at lower laser repetition rates. Additionally, monitoring the coarsening behavior for different epitaxial films my yield interesting results.

Another suggestion for future experiments involves a different materials system: $EuTiO_3$ on $SrTiO_3\langle 001\rangle$. When performing the surface diffusivity measurement outlined in Chapter 4 on $EuTiO_3$, an interesting feature was noticed in the growth mechanism. Fig. 6.2a shows the surface diffuse x-ray scattering data during the pulsed laser deposition of $EuTiO_3$ on $SrTiO_3\langle 001\rangle$. The corresponding specular intensity is presented in Fig. 6.2b.

This growth was performed at a substrate temperature of 785°C and a background pressure of 2×10^{-4} Torr O_2. The laser parameters were set with a laser repetition rate of 0.2 Hz, a laser spot size of 7.4mm^2, and a laser fluence of 1.2 J cm^{-2}. Interestingly, both the diffuse and specular intensity oscillations indicate that the $EuTiO_3$ film begins in a layer-by-layer growth mode. However, after approximately three monolayers, the growth changes to step-flow. This is realized by knowing that the periodicity seen in the specular intensity after $t \approx 250$ seconds are Kiessig oscillations [67]. Additionally, since the average specular intensity remains constant, the surface roughness is not changing. A very interesting part of this data is the presence of a finite surface length scale during the step-flow growth

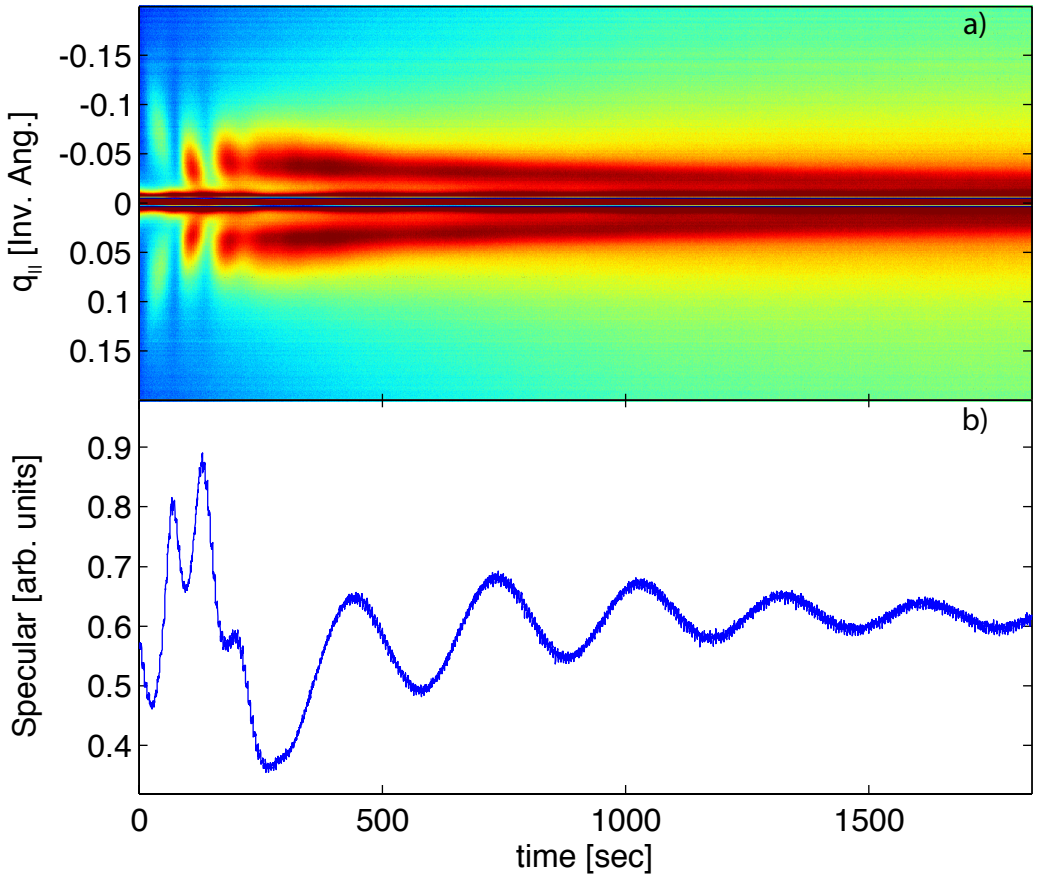

Figure 6.2: (a) Surface diffuse scattering and (b) the specular intensity as a function of time for the PLD of $EuTiO_3$ on $SrTiO_3\langle 001\rangle$ at 785°C. The first 3 monolayers grow in a layer-by-layer mode which then transitions to step-flow growth.

mode. In step-flow growth, islands do not nucleate on the surface, and therefore no surface length scale should be present.

In Chapter 4 we showed that the surface diffusivity is dependent on the number of $LaAlO_3$ monolayers deposited. The same behavior may be responsible for the behavior of the $EuTiO_3$ system. Specifically, there may be a large increase in the surface diffusivity when the substrate is no longer "visible" to the diffusing species. Although this model explains the specular behavior, it does not explain

the presence of the finite surface length scale seen in Fig. 6.2a. Typically, in step-flow growth, when material is added to the surface it diffuses to a terrace before any island nucleation occurs. Therefore, since the sample is oriented such that the terraces are perpendicular to the incident x-ray beam, no surface length scale should be seen by the diffuse scattering. One possible explanation for the presence of the length scale may be that the miscut steps on the surface are no longer strait. If the step-edges became "wavy," they would produce a peak in $q_{||}$. Another possible mechanism to explain this data, is the formation of deep pits on the surface. If these pits form in the layer-by-layer regime, they would still be present on the surface during the step flow portion of the growth.

While there are many models that may explain Fig. 6.2, it is clear that a distinct change in surface kinetics occurs around 3 MLs. The ideal way to investigate this behavior is to perform the analysis shown in Chapter 4 on the layer-by-layer region. It is possible that this same analysis may be applied to the step-flow portion of the growth, however, the relationship between the surface length scale ($L \propto q_0^{-1}$), the terrace width [due to the surface miscut], and the characteristic specular relaxation time must be corroborated. This will most likely be a collaborative effort between atomic force microscopy and x-ray scattering. One may also want to measure the distance between terraces during deposition. This may be accomplished by orienting the terraces such that they are parallel to the incident x-ray beam, i.e. rotate the sample 90° relative to the orientation seen in Fig. 2.1.

Another research project involves applications of our getter layer method presented in Chapter 5. From our experiments, we know that $SrTiO_3$ and $LaAlO_3$ will both act as an oxygen getter for the manganite films. The results published by Takahashi, et al. [79] suggest that $LaTiO_3$ will also function as an oxygen getter.

While this is interesting, the range of materials that can act as oxygen getters must be explored further. Specifically, for this method to be useful in solid oxide fuel cells (SOFC), heterostructures must be made using electrolyte materials as an oxygen getter. The functional description of a SOFC was shown in Fig. 1.2. This research project would involve growing numerous new materials, and testing their ability to act as a getter. The results in Chapter 5 suggest that the diffusional driving force is the difference in oxygen affinity between the getter and manganite layers. Some preliminary research may be done by comparing the oxygen affinity of electrolytic materials to that of $SrTiO_3$ and $LaAlO_3$. If the oxygen affinity is the driving force, materials with affinities comparable to or larger than that of $SrTiO_3$ should also act as a getter for the manganite films.

APPENDIX A

SUBSTRATE ETCHING PROCEDURE FOR STRONTIUM TITANATE $\langle 001 \rangle$

Here I list the step-by-step process that was used to treat each $SrTiO_3\langle 001 \rangle$ substrate prior to deposition. Etching the surface ensures a TiO_2 termination, and the anneal produces atomically flat terraces separated by unit cell high steps. This process was adopted from the publication by Koster, et al. [42], but has been altered slightly for our substrates. The procedure is as follows:

1. When handling the substrates prior to the etch be sure to never let them come in contact with metals of any kind.
2. Clean the glassware to be used for etching, along with the Teflon tweezers.
   (a) Rinsing the utensils in ultra pure water about ten times.
   (b) Next, fill the 1000mL beaker to the 1000mL mark with ultra-pure H20. Fill 50% of the remaining volume of the beaker with the Hydrogen Peroxide 30%.
   (c) Fill the remaining volume of the beaker with the Ammonium Hydroxide.
   (d) Put the solution on the hotplate (100°C) and let boil for a minimum of 15 minutes.
   (e) Pour about 1/4 of the solution into the waste beaker.
   (f) Fill to the top with the ultra-pure H_2O.
   (g) Pour out the solution, making sure not to pour out any of the utensils.
   (h) Rinse in ultra-pure H_2O about ten times.

(i) Remove the glassware in the 1000mL beaker being careful not to touch the inside of any containers.

(j) Let dry, or spray with argon gas to dry.

3. Fill each glass container with ≈1 cm of ultra pure H_2O.

4. Place each substrate to be etched in different glassware.

5. Sonicate the substrates for 15 minutes in ultra-pure H_2O.

6. While the substrates are sonicating, prepare the etch solution.

   (a) Place the weighing paper down in the fume hood where you plan to work.

   (b) Clean the Teflon sheet with Alconox and rinse in ultra-pure H_2O and place on the weighing paper in the fume hood. This Teflon insures that none of the salts from the fume hood tabletop get onto your substrates. Place the Teflon dish on the Teflon sheet.

   (c) You will be etching in a 5:1 solution of Buffered Oxide Etch.

   (d) Place a small amount of the etch solution (just enough such that the substrate can be covered) in the Teflon dish and cover with the 1000mL beaker that you cleaned in step 1.

   (e) Take extra care to insure that NOTHING touches the fume hood tabletop.

7. When the substrates are done sonicating, remove them one by one and etch using the following procedure:

   (a) Remove the substrate from the water and very quickly place it in the B.O.E. If the substrate drops during this procedure, do not contaminate

the B.O.E. and glassware with this substrate.

(b) Allow the substrate to etch in the B.O.E. for 25 seconds.

(c) Promptly remove the substrate from the B.O.E. and place in the beaker of ultra-pure H2O for about 15 seconds.

(d) Remove the substrate from the water, place it on the Teflon sheet, and spray off with argon very quickly. This assures that the water does not dry on the substrate.

8. Now you can anneal the sample.

(a) To make sure that nothing happened to the sample during the etch, you should AFM one of the samples to look for etch pits.

(b) Anneal the substrates in the tube furnace under O_2 flow using the following ramping parameters:

i. SP1=1000°C

ii. Time1=4.5 hours (Ramp Time)

iii. SP2=1000°C

iv. Time2=2.5 hours (Anneal Time)

v. SP3=400°C

vi. Time3=4 hours (Ramp Time)

vii. SP4=20°C

viii. Time4=off

9. If desired, you can now repeat the etching process.

APPENDIX B

DATA ANALYSIS CODES

Here I present the Matlab codes used to perform the non-linear least squares fitting routines throughout this thesis. A flow chart to help visualize the software is shown in Fig. B.1. The main code for fitting is Lfit_DA_v2c.m. This code calls four other functions: pre_pulse_fit_v9.m, L3fit9vm, L5fitv9.m, and Lfit_DA_plots_v2c.m. The pre_pulse_fit_v9.m function fits the data before the laser has fired, to obtain a starting point for the specular lineshape. L3fitv9.m is used to fit the line shape to three power Lorentzian functions: one for the specular and one for each diffuse lobe. L5fitv9.m is used to fit the line shape to five power Lorentzian functions: one for the specular and two for each diffuse lobe. L5fitv9.m must be used for some of the higher temperature depositions, where a second order reflection in the diffuse scattering is seen. The Lfit_DA_plots_v2c.m function is used to plot the fit results in real time, and export the plots to an AVI file. The function Lfit_DA_v2c.m may be called at the command line, or through a graphical user interface. The Lfit_GUI.m code allows the user to easily choose the fit constraints, without the need of using the command line. A screenshot of the graphical user interface is shown in Fig. B.2.

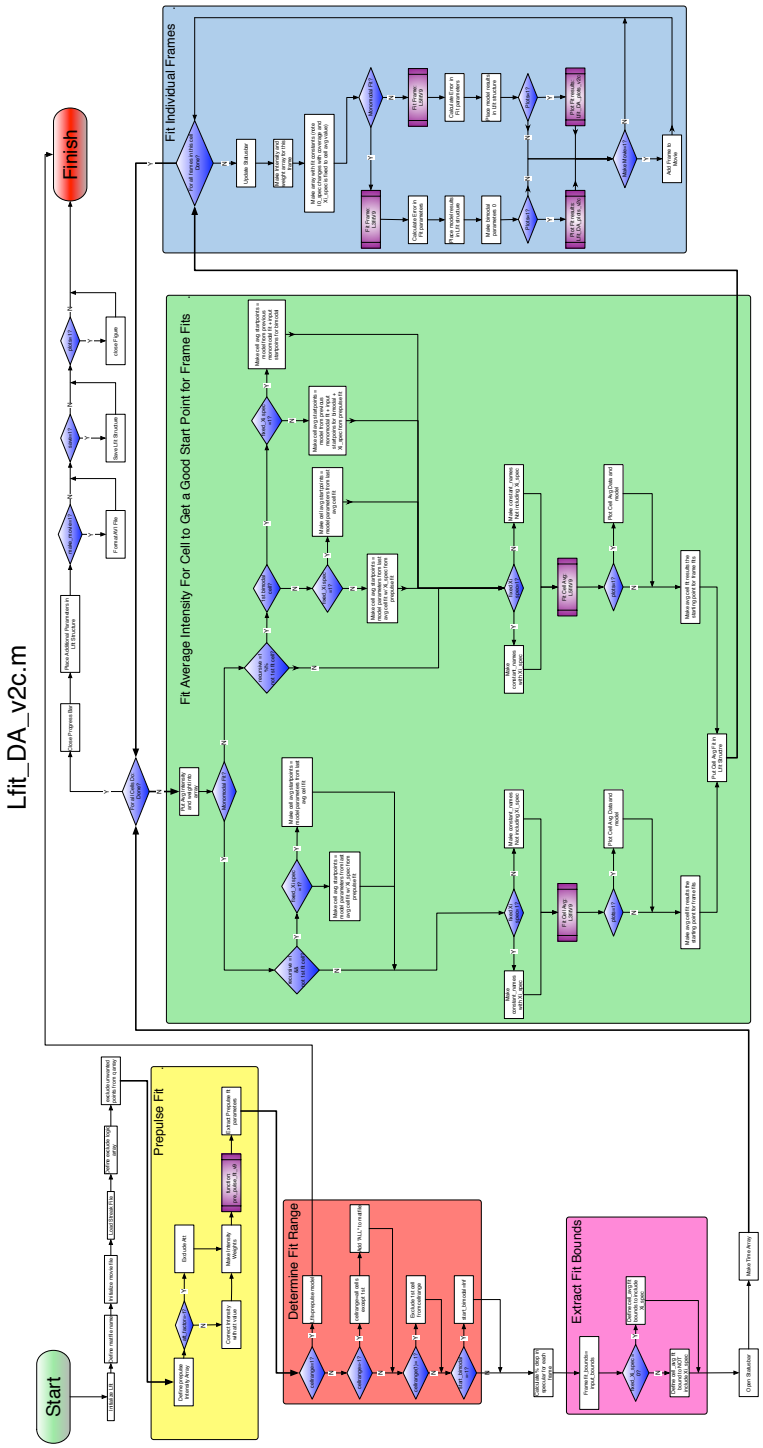

Figure B.1: A flow chart of the Lfit_DA_v2c.m fit routine. To examine the details, use the electronic version of this thesis to zoom in.

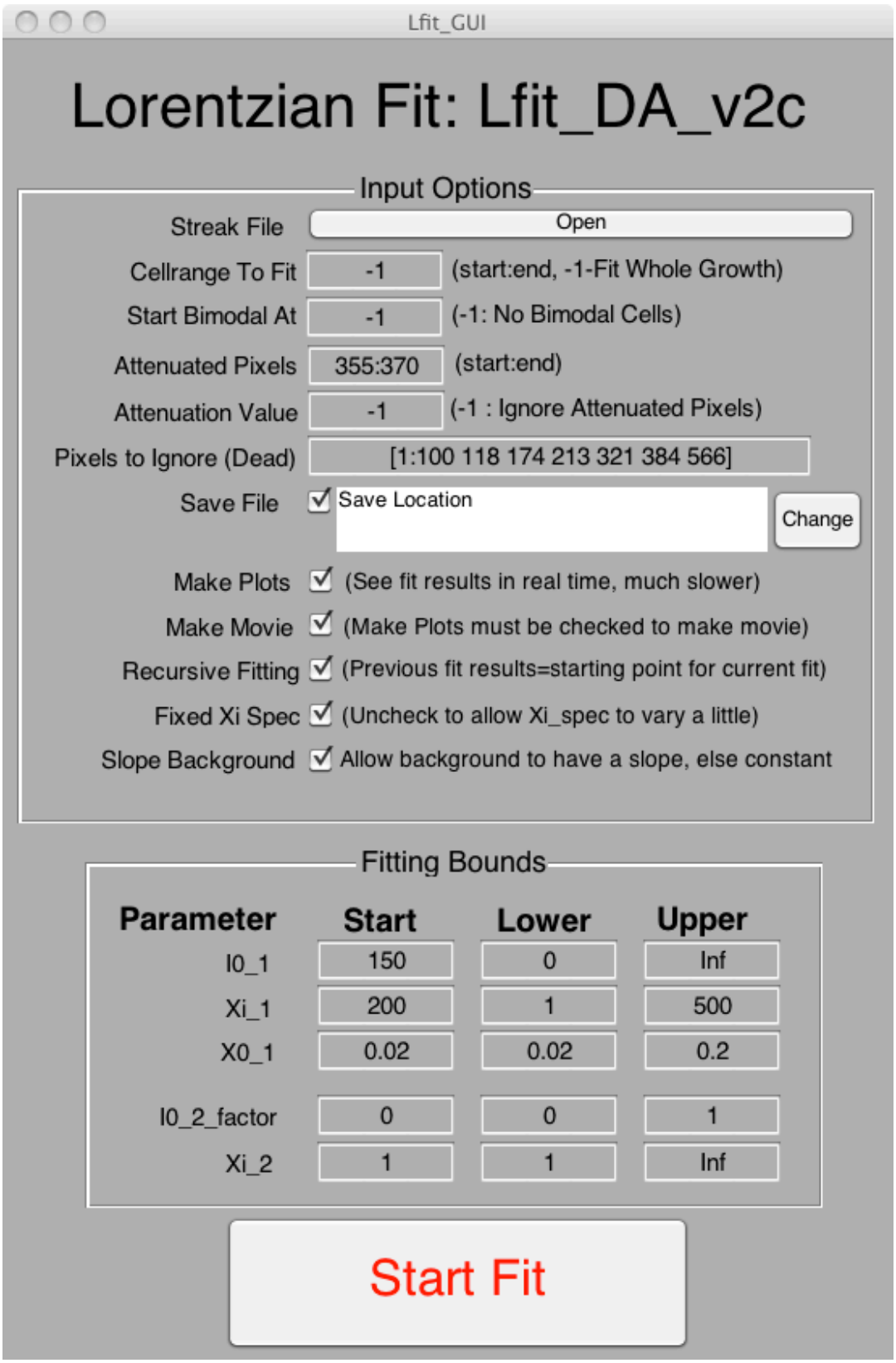

Figure B.2: A screenshot of the GUI to execute Lfit_DA_plots_v2c.m.

B.1 Lfit_DA_v3.m

```
function Lfit = Lfit_DA_v2c(file,cellrange,start_bimodal,...
    att_factor,attrange,corr_range,bounds,plots,auto_save,...
    ccd_cut,make_movie,recursive,fixed_Xi_spec,slope_bkg)
%Usage: Lfit = Lfit_DA_v2c(file,cellrange,start_bimodal,...
%    att_factor,attrange,corr_range,bounds,plots,auto_save,...
%    ccd_cut,make_movie,recursive,fixed_Xi_spec,slope_bkg)
%
% Requirements: pre_pulse_fit_v9.m
%               L3fitv9.m
%               L5fitv9.m
%               Lfit_DA_plots_v2c
%
% "file" must be a .mat file from openstreak_DA.m
%
% Improvements to make:
%   1. Be able to define specific cells that have a bimodal
%   fit instead of just starting one.
%   2. Optimize code. There are a few things that could be
%   improved that I saw in the flow chart.
%   3. Add ability to remove zingers.
%% LFit Version
Lfit_version='Lfit_DA_v2c';
ID=randi(1e9);% number used to correlated the .mat and .avi files
%% Perform Preliminary functions
Lfit=struct;% Make Lfit structure
matfile = strrep(file, 'streak.mat', sprintf('%s.mat',...
    Lfit_version)); %filename to save Lfit

if make_movie==1 % Initialize movie file
    if plots==0
        disp('Plots must be on to make the movie')
        disp('Exiting Lfit')
        return
    end
    if cellrange==-1 %Define movie name
        movie_name=strrep(file,'streak.mat','Lfit_ALL.avi');
    else
        movie_name=strrep(file,'streak.mat','Lfit.avi');
    end
    if exist(movie_name,'file')==2
```

```
        delete(movie_name);
        Lfit=0;
    end
    aviobj = avifile(movie_name,'Fps',15);
end
load(file)
error_im=sqrt(streak.im);   % Calculate Error Image
q1=streak.q;    % Get q
% get logic arrays for indices of att and exclude_points
att=zeros(size(q1));    %create attenuator logic array
att(attrange)=1;        %set appropriate logic position high
ccd_exclude=zeros(size(q1));%create dead pixel logic array
ccd_exclude(ccd_cut)=1;     %set appropriate logic position high
exclude=att|ccd_exclude;%put att and ccd_exclude in 1 logic array
q=q1(~exclude);%create q array that excludes att and dead pixels

%% Fit Pre Pulse Data
% prepulse_status=waitbar(0,'Fitting Prepulse Data');
prepulse_status=msgbox('Fitting Prepulse Data');

% Get Intensity for pre pulse frames
I_pre_pulse_raw=mean(streak.im(streak.frames{1},:));

if att_factor==-1% if att_factor=-1 don't correct att portion
    I_pre_pulse=I_pre_pulse_raw(~exclude);
    q_pre_pulse=q;
else        % Correct attenuated portion for fit
    I_pre_pulse_raw(corr_range)=I_pre_pulse_raw(...
        corr_range)*att_factor;
    q_pre_pulse=q1(~ccd_exclude);
    I_pre_pulse=I_pre_pulse_raw(~ccd_exclude);
end

I_pre_pulse_wt=I_pre_pulse;% get Weights
model1=pre_pulse_fit_v9(q_pre_pulse,I_pre_pulse,...
    I_pre_pulse_wt,plots,slope_bkg);% Fit pre_pulse_data
if plots==1 %Display Lfit version
    title_str=strrep(sprintf('%s,  %s , ID = %1.0f',...
        strrep(file,'_streak.mat',''),Lfit_version,ID),'_','\_');
    annotation('textbox',[0.3,.95,.05,.05],'string',title_str,...
        'FitBoxToText','on','LineStyle','none','FontSize',14);
end
    % Extract Fit parameters
I0_spec=model1.I0;
```

```
Xi_spec=model1.Xi;
x0_spec=model1.x0;
n=model1.n;
bkg_const=model1.bkg_const;
bkg_sl=model1.bkg_sl;
delete(prepulse_status);

%% Define Cell range to Fit
if cellrange==1 %if celrange=1just do prepulse data
    Lfit.pre_pulse_model=model1;
    figure(1)
    clf
    semilogy(q_pre_pulse,I_pre_pulse,'.')
    hold on
    plot(model1)
    hold off
    xlabel('q [Inv. Ang.]')
    ylabel('Int. [cts/s]')
    title('Pre-pulse Fit')
    legend off
    return
elseif cellrange==-1 % if cellrange=-1 do whole image
    cellrange=2:size(streak.frames,2);
    matfile = strrep(file, 'streak.mat',...
        sprintf('%s_ALL.mat',Lfit_version));
end

if cellrange(1)==1%ignore cell 1,was just done with pre_pulse_fit
    cellrange=2:cellrange(end);
end

if start_bimodal==-1 % don't do bimodal fit if start_bimodal=-1
    start_bimodal=Inf;
end

%% Now do the Fitting

%% Define the specular value for each frame to confine fit
spec_raw=sum(streak.im(:,attrange),2);
spec_factor=spec_raw/sum(I_pre_pulse_raw(attrange));

%% Set cell average fitting bounds
%   (different, b/c Xi_spec can vary in cell avg fit)
% Get user specified fitting bounds from input
```

```
sp1=bounds.sp1;
low1=bounds.low1;
up1=bounds.up1;
sp2=bounds.sp2;
low2=bounds.low2;
up2=bounds.up2;
% Alter fit bound based upon if Xi_spec is constant
if fixed_Xi_spec==1
    sp1_cell_avg=sp1;
    low1_cell_avg=low1;
    up1_cell_avg=up1;
    sp2_cell_avg=sp2;
    low2_cell_avg=low2;
    up2_cell_avg=up2;
else
    sp1_cell_avg=[sp1(1:2) Xi_spec sp1(3:end)];
    low1_cell_avg=[low1(1:2) 0.9*Xi_spec low1(3:end)];
    up1_cell_avg=[up1(1:2) 2*Xi_spec up1(3:end)];

    sp2_cell_avg=[sp2(1:4) Xi_spec sp2(end)];
    low2_cell_avg=[low2(1:4) 0.9*Xi_spec low2(end)];
    up2_cell_avg=[up2(1:4) 2*Xi_spec up2(end)];
end

%% Get values used to calculate percent done and open status bar
fr1=streak.frames{cellrange(1)}(1);
div=(streak.frames{cellrange(end)}(end)-...
    streak.frames{cellrange(1)}(1));
status=waitbar(0,'0.0 %','Name','Running Lfit',...
    'CreateCancelBtn','setappdata(gcbf,''canceling'',1)');
pause(2) %pause so that you can move waitbar if desired

%% Make time array
t=streak.t; %put time into array
% Get last time value for plotting specular
tf=t(streak.frames{cellrange(end)}(end));

%% Start Fitting Frames
for cell=cellrange;% Fit the frames after the 1st pulse
    %% Put average intensity and weight into array
    I_mean_raw=mean(streak.im(streak.frames{cell},:));
    I_mean_er=mean(error_im(streak.frames{cell},:));
    I_mean=I_mean_raw(~exclude);
    I_mean_wt=1./I_mean_er(~exclude).^2;
```

```
%% Fit cell average intensity
if cell<start_bimodal
    %% Perform Monomodal Avg Cell Fit
    if recursive==1 && cell~=cellrange(1)
        if fixed_Xi_spec==1
            sp1_cell_avg=sp1;
        else
            sp1_cell_avg=[sp1(1:2) Xi_spec sp1(3)];
        end
    end
    % if fixed_Xi_spec=1 put Xi_spec into constant names/vals
    if fixed_Xi_spec==1
        constant_names={'I0_spec','Xi_spec','x0_spec',...
            'n','bkg_const','bkg_sl'};
        constant_vals ={I0_spec*mean(spec_factor(...
            streak.frames{cell})),Xi_spec,x0_spec,n,...
            bkg_const,bkg_sl};
    % if fixed_Xi_spec==0 don't put Xi_spec into constant
    % names/vals
    else
        constant_names={'I0_spec','x0_spec','n',...
            'bkg_const','bkg_sl'};
        constant_vals ={I0_spec*mean(spec_factor(...
            streak.frames{cell})),x0_spec,n,bkg_const,...
            bkg_sl};
    end
    cell_avg_model=L3fitv9(q,I_mean,I_mean_wt,...
        sp1_cell_avg,low1_cell_avg,up1_cell_avg,...
        constant_names,constant_vals);
    if(plots==1)
        figure(1);
        subplot(5,3,[1 4])
        semilogy(q,I_mean,'.')
        hold on
        plot(cell_avg_model)
        hold off
        title(sprintf('Average Intensity for Cell %1.0f',...
            cell))
        legend off
        axis([min(q) max(q) .9*min(I_mean) 10*max(I_mean)])
        xlabel('q [Inv. Ang.]')
        ylabel('Int. [cts/s]')
    end
    sp1=[cell_avg_model.I0_1,cell_avg_model.Xi_1,...
```

```
        cell_avg_model.x0_1];%use avg cell pars as stpoints
else
    %% Perform Bimodal Avg Cell Fit
    if recursive==1 && cell~=cellrange(1)
        if cell==start_bimodal
            if fixed_Xi_spec==1
                sp2_cell_avg=[sp1(1) bounds.sp2(2) sp1(2)...
                    bounds.sp2(4) sp1(3)];
            else
                sp2_cell_avg=[sp1(1) bounds.sp2(2) sp1(2)...
                    bounds.sp2(4) Xi_spec sp1(3)];
            end
        else
            if fixed_Xi_spec==1
                sp2_cell_avg=sp2;
            else
                sp2_cell_avg=[sp2(1:4) Xi_spec sp2(5)];
            end
        end
    end
   % if fixed_Xi_spec=1 put Xi_spec into constant names/vals
    if fixed_Xi_spec==1
        constant_names={'I0_spec','Xi_spec','x0_spec','n',...
            'bkg_const','bkg_sl'};
        constant_vals ={I0_spec*mean(spec_factor(...
            streak.frames{cell})),Xi_spec,x0_spec,n,...
            bkg_const,bkg_sl};
    else%if fixed_Xi_spec=0 no Xi_spec in constant names/vals
        constant_names={'I0_spec','x0_spec','n',...
            'bkg_const','bkg_sl'};
        constant_vals ={I0_spec*mean(spec_factor(...
           streak.frames{cell})),x0_spec,n,bkg_const,bkg_sl};
    end
    cell_avg_model=L5fitv9(q,I_mean,I_mean_wt,...
        sp2_cell_avg,low2_cell_avg,up2_cell_avg,...
        constant_names,constant_vals);
    if(plots==1)
        figure(1);
        subplot(5,3,[1 4])
        semilogy(q,I_mean,'.')
        hold on
        plot(cell_avg_model)
        hold off
        title(sprintf('Average Intensity for Cell %1.0f',...
```

```
                cell))
            legend off
            axis([min(q) max(q) .9*min(I_mean) 10*max(I_mean)])
            xlabel('q [Inv. Ang.]')
            ylabel('Int. [cts/s]')
        end
        sp2=[cell_avg_model.I0_1,cell_avg_model.I0_2_factor,...
            cell_avg_model.Xi_1,cell_avg_model.Xi_2,...
            cell_avg_model.x0_1];%use avgcell as startpoints
    end
    %% Put cell_avg_model into Lfit Structure
    Lfit.cell_avg_model{cell}=cell_avg_model;
    %% Fit individual frames
    for i=streak.frames{cell}
        %% Update Status Bar
        if getappdata(status,'canceling')% if cancel, quit.
            Lfit=0;
            disp 'Fitting Aborted'
            delete(status)
%             close(1)
            if make_movie==1 && exist(movie_name,'file')==2
                delete(movie_name);
            end
            return
        end
        waitbar((i-fr1)/div,status,sprintf('%1.1f %s',...
            (i-fr1)/div*100,'%'));

        %% Make Intensity and Weight Arrays
        clear Int1 Int1error I weight options model gof output
        % Get intensity arrays
        Int1=streak.im(i,:);
        Int1error=error_im(i,:);
        I=Int1(~exclude);
        weight=1./Int1error(~exclude).^2;

        %% Make array with fit constants
        %  (note I0_spec changes with coverage)
        constant_names={'I0_spec','Xi_spec','x0_spec','n',...
            'bkg_const','bkg_sl'};
        constant_vals ={I0_spec*spec_factor(i),...
            cell_avg_model.Xi_spec,x0_spec,n,bkg_const,bkg_sl};

        %% Perform fits
```

```
if cell<start_bimodal
    %% Perform Monomodal fits
    [model,gof,output,ci]=L3fitv9(q,I,weight,...
        sp1,low1,up1,constant_names,constant_vals);
    % Calculate error in fitting parameters
    I0_1_error=abs(model.I0_1-max(ci(:,1)));
    Xi_1_error=abs(model.Xi_1-max(ci(:,2)));
    x0_1_error=abs(model.x0_1-max(ci(:,3)));

    % Place the model and fit parameters in a structure
    Lfit.I0_1(i)=model.I0_1;
    Lfit.I0_1_er(i)=I0_1_error;
    Lfit.Xi_1(i)=model.Xi_1;
    Lfit.Xi_1_er(i)=Xi_1_error;
    Lfit.x0_1(i)=model.x0_1;
    Lfit.x0_1_er(i)=x0_1_error;
    Lfit.I0_2_factor(i)=0;
    Lfit.I0_2_factor_er(i)=0;
    Lfit.Xi_2(i)=0;
    Lfit.Xi_2_er(i)=0;
    Lfit.model{i}=model;
    Lfit.gof{i}=gof;
    Lfit.output{i}=output;
    if(plots==1) %plot data if desired
        Lfit_DA_plots_v2c(model,gof,spec_factor,q1,q,...
            I,cell,i,t,tf,0)
    end
else
    %% Perform Bimodal fits
    [model,gof,output,ci]=L5fitv9(q,I,weight,sp2,...
        low2,up2,constant_names,constant_vals);
    % Calculate error in fitting parameters
    I0_1_error=abs(model.I0_1-max(ci(:,1)));
   I0_2_factor_error=abs(model.I0_2_factor-max(ci(:,2)));
    Xi_1_error=abs(model.Xi_1-max(ci(:,3)));
    Xi_2_error=abs(model.Xi_2-max(ci(:,4)));
    x0_1_error=abs(model.x0_1-max(ci(:,5)));

    % Place the model and fit parameters in a structure
    Lfit.I0_1(i)=model.I0_1;
    Lfit.I0_1_er(i)=I0_1_error;
    Lfit.Xi_1(i)=model.Xi_1;
    Lfit.Xi_1_er(i)=Xi_1_error;
    Lfit.x0_1(i)=model.x0_1;
```

```
            Lfit.x0_1_er(i)=x0_1_error;
            Lfit.I0_2_factor(i)=model.I0_2_factor;
            Lfit.I0_2_factor_er(i)=I0_2_factor_error;
            Lfit.Xi_2(i)=model.Xi_2;
            Lfit.Xi_2_er(i)=Xi_2_error;
            Lfit.model{i}=model;
            Lfit.gof{i}=gof;
            Lfit.output{i}=output;
            if(plots==1) %plot data if desired
                Lfit_DA_plots_v2c(model,gof,spec_factor,q1,q,...
                    I,cell,i,t,tf,1)
            end
        end
        %% Put results into movie file
        if make_movie==1 %export plots to a movie, if desired
            aviobj = addframe(aviobj,getframe(figure(1)));
        end
    end
end

delete(status); %close status bar

%% Place Remaining parameters into Lfit Structure
% Place other parameters into Structure
Lfit.q=q1;
Lfit.im=streak.im;
Lfit.time=streak.t(1:streak.frames{cellrange(end)}(end));
Lfit.specular=spec_raw';
Lfit.att=attrange;
Lfit.pre_pulse_model=model1;
% Place input parameter into structure
Lfit.input.file=file;
Lfit.input.cellrange=cellrange;
Lfit.input.start_bimodal=start_bimodal;
Lfit.input.att_factor=att_factor;
Lfit.input.attrange=attrange;
Lfit.input.corr_range=corr_range;
Lfit.input.bounds=bounds;
Lfit.input.plots=plots;
Lfit.input.auto_save=auto_save;
Lfit.input.ccd_cut=ccd_cut;
Lfit.input.make_movie=make_movie;
Lfit.input.recursive=recursive;
Lfit.input.fixed_Xi_spec=fixed_Xi_spec;
```

```
Lfit.input.slope_bkg=slope_bkg;
Lfit.version=Lfit_version;
Lfit.ID=ID;
%% build movie if desired
if make_movie==1
    avi_status=msgbox(...
        'Formatting AVI. Box will close when process completes');
    aviobj=close(aviobj);
    delete(avi_status);
end

%% save Lfit structure
if(auto_save==1)
    save(matfile,'Lfit');
    disp('Lfit Structure Saved')
else
    disp('Lfit Structure NOT Saved')
end
%% Close figure and beep
if plots==1
    close(1)
end
beep

return
```

B.2 pre_pulse_fit_v9.m

```
function [model,conf_int] = pre_pulse_fit_v9(q,I,I_wt,plots,...
    slope_bkg)
% Usage:[model,conf_int] = pre_pulse_fit_v9(q,I,I_wt,plots,...
%    slope_bkg)


%% Get estimate for bkg_const
bkg_ind=([find(q<-0.1) find(q>0.1)]);
bkg_const_est=mean(I(bkg_ind));
bkg_sl_est=(I(end)-I(1))/(q(end)-q(1));

%% Fit prepulse Data
if slope_bkg==1
    options=fitoptions('Weights',I_wt(:),'Method',...
        'NonlinearLeastSquares','maxfunevals',10000,...
        'StartPoint',[6000,600,bkg_const_est,bkg_sl_est,1.5,0],...
        'lower',[0,0,0,-Inf,1,-0.1],'upper',...
        [Inf,Inf,Inf,Inf,3,0.01]);
    f=fittype('(I0*Xi*(1+Xi^2*(x - x0)^2)^-n)/2 +...
    bkg_sl*x + bkg_const','options',options);
    model=fit(q(:),I(:),f);
else
    options=fitoptions('Weights',I_wt(:),'Method',...
        'NonlinearLeastSquares','maxfunevals',10000,...
    'StartPoint',[6000,80,bkg_const_est,1.5,0],'lower',...
    [0,0,0,1,-0.1],'upper',[Inf,Inf,Inf,3,0.01]);
    constant_names={'bkg_sl'};
    constant_vals ={0};
    f=fittype('(I0*Xi*(1+Xi^2*(x - x0)^2)^-n)/2 +...
    bkg_sl*x + bkg_const','problem',constant_names,...
        'options',options);
    model=fit(q(:),I(:),f,'problem',constant_vals);
end
conf_int=confint(model,0.667);
%% Plot prepulse fit results
if(plots==1)
    f=figure(1);
    clf
    subplot(5,3,[10 13])
    semilogy(q,I,'.')
```

```
    hold on
    plot(model)
    hold off
    title('Pre-pulse Fit')
    legend off
    axis([min(q) max(q) 0.9*min(I) Inf])
    xlabel('q [Inv. Ang.]')
    ylabel('Int. [cts/s]')
    set(f,'Position',[25,200,960,720]);
end
return
```

B.3 L3fitv9.m

```
function [model,gof,output,ci] = L3fitv9(q,I,weight,sp1,low1,...
    up1,constant_names,constant_vals)

options=fitoptions('Weights',weight,'Method',...
    'NonlinearLeastSquares','maxfunevals',10000,'StartPoint',...
    sp1,'lower',low1,'upper',up1);

f=fittype('(I0_spec*Xi_spec*(1+...
    Xi_spec^2*(x - x0_spec)^2)^-n)/2 +...
    (I0_1*Xi_1*(1+Xi_1^2*(x-(x0_spec-x0_1))^2)^(-1.5))/2 +...
    (I0_1*Xi_1*(1+Xi_1^2*(x-(x0_spec+x0_1))^2)^(-1.5))/2 +...
    bkg_sl*x+bkg_const',...
    'problem',constant_names,'options',options);

[model,gof,output]=fit(q(:),I(:),f,'problem',constant_vals);

% Determine Error
conf=0.667;
ci=confint(model,conf);

return
```

B.4 L5fitv9.m

```
function [model,gof,output,ci] = L5fitv7(q,I,weight,sp2,low2,...
    up2,constant_names,constant_vals)

options=fitoptions('Weights',weight,'Method',...
    'NonlinearLeastSquares','maxfunevals',10000,'StartPoint',...
    sp2,'lower',low2,'upper',up2);

f=fittype('(I0_spec*Xi_spec*(1+...
Xi_spec^2*(x - x0_spec)^2)^-n)/2 +...
    (I0_1*Xi_1*(1+Xi_1^2*(x-(x0_spec-x0_1))^2)^(-1.5))/2 +...
    (I0_1*Xi_1*(1+Xi_1^2*(x-(x0_spec+x0_1))^2)^(-1.5))/2 +...
    (I0_2_factor*I0_1*Xi_2*(1+...
    Xi_2^2*(x-(x0_spec-2*x0_1))^2)^(-1.5))/2 +...
    (I0_2_factor*I0_1*Xi_2*(1+...
    Xi_2^2*(x-(x0_spec+2*x0_1))^2)^(-1.5))/2 +...
    bkg_sl*x+bkg_const',...
    'problem',constant_names,'options',options);

[model,gof,output]=fit(q(:),I(:),f,'problem',constant_vals);

% Determine Error
conf=0.667;
ci=confint(model,conf);

return
```

B.5 Lfit_DA_plots_v2c.m

```
function [] = Lfit_DA_plots_v2c(model,gof,spec,q1,q,I,cell,i,...
    t,tf,bimodal)

%% put individual fits into array
y1=(model.I0_spec*model.Xi_spec*(1+model.Xi_spec^2*(q1 -...
    model.x0_spec).^2).^-model.n)/2;
if bimodal==0
    y2=(model.I0_1*model.Xi_1*(1+model.Xi_1^2*(q1-...
        (model.x0_spec-model.x0_1)).^2).^(-1.5))/2 +...
   (model.I0_1*model.Xi_1*(1+model.Xi_1^2*(q1-...
   (model.x0_spec+model.x0_1)).^2).^(-1.5))/2;
elseif bimodal==1
    y2=(model.I0_1*model.Xi_1*(1+model.Xi_1^2*(q1-...
        (model.x0_spec-model.x0_1)).^2).^(-1.5))/2 +...
        (model.I0_1*model.Xi_1*(1+model.Xi_1^2*(q1-...
        (model.x0_spec+model.x0_1)).^2).^(-1.5))/2+...
        (model.I0_2_factor*model.I0_1*model.Xi_2*(1+...
        model.Xi_2^2*(q1-...
        (model.x0_spec-2*model.x0_1)).^2).^(-1.5))/2 +...
        (model.I0_2_factor*model.I0_1*model.Xi_2*(1+...
        model.Xi_2^2*(q1-...
        (model.x0_spec+2*model.x0_1)).^2).^(-1.5))/2;
else
    disp('Bimodal must be 0 or 1')
    return
end

figure(1)
%% Plot on log scale
subplot(5,3,[2:3 5:6])
semilogy(q,I,'.');
axis([min(q) max(q) 0.5*model.bkg_const 50e3])
hold on
plot(model);
hold off
title(sprintf('Cell %1.0f, Frame %1.0f',cell,i))
xlabel('Q [Inv. Ang.]')
ylabel('Int. [cts/s]')
text(0.05,10000,sprintf('Chi^2 = %0.2f',gof.sse/gof.dfe),...
    'FontSize',16)
```

```
legend('off')
%% Plot on linear scale
subplot(5,3,[8:9 11:12])
plot(q,I/1e3,'.',q1,y2/1e3,'k',q1,y1/1e3,'r')
axis([min(q) max(q) 0 max(I)/1e3])
xlabel('Q [Inv. Ang.]')
ylabel('Int. [10^3 cts/s]')
%% plot specular oscillation
subplot(5,3,14:15)
plot(t(1:i),spec(1:i),'.-')
xlabel('Time [s]')
ylabel('Specular')
axis([0 tf 0.9*min(spec) 1.1*max(spec)])

return
```

B.6 Lfit_GUI.m

```
function varargout = Lfit_GUI(varargin)


% Begin initialization code - DO NOT EDIT
gui_Singleton = 1;
gui_State = struct('gui_Name',       mfilename, ...
                   'gui_Singleton',  gui_Singleton, ...
                   'gui_OpeningFcn', @Lfit_GUI_OpeningFcn, ...
                   'gui_OutputFcn',  @Lfit_GUI_OutputFcn, ...
                   'gui_LayoutFcn',  [] , ...
                   'gui_Callback',   []);
if nargin && ischar(varargin{1})
    gui_State.gui_Callback = str2func(varargin{1});
end

if nargout
    [varargout{1:nargout}] = gui_mainfcn(gui_State, varargin{:});
else
    gui_mainfcn(gui_State, varargin{:});
end
% End initialization code - DO NOT EDIT

% --- Executes just before Lfit_GUI is made visible.
function Lfit_GUI_OpeningFcn(hObject, eventdata, handles,...
    varargin)

% Choose default command line output for Lfit_GUI
handles.output = hObject;

% Update handles structure
guidata(hObject, handles);

% --- Outputs from this function are returned to the command line.
function varargout = Lfit_GUI_OutputFcn(hObject, eventdata,...
    handles)

% Get default command line output from handles structure
varargout{1} = handles.output;
```

```
% --- Executes on button press in startfit.
function startfit_Callback(hObject, eventdata, handles)

file = get(handles.openfile,'String');
cellrange=str2num(get(handles.cellrange,'String'));
start_bimodal=str2double(get(handles.start_bimodal,'String'));
attrange=str2num(get(handles.edit25,'String'));
corr_range=attrange;
att_factor=str2double(get(handles.att_factor,'String'));
ccd_cut=str2num(get(handles.ccd_cut,'String'));
force_save=get(handles.save_file,'Value');
plots=get(handles.plots,'Value');
make_movie=get(handles.make_movie,'Value');
recursive=get(handles.recursive,'Value');
fixed_Xi_spec=get(handles.fixed_Xi_spec,'Value');
slope_bkg=get(handles.slope_bkg,'Value');



% Define StartPoints
start_I0_1=str2double(get(handles.start_I0_1,'String'));
start_Xi_1=str2double(get(handles.start_Xi_1,'String'));
start_x0_1=str2double(get(handles.start_x0_1,'String'));
start_I0_2=str2double(get(handles.start_I0_2,'String'));
start_Xi_2=str2double(get(handles.start_Xi_2,'String'));
% Define Lower Bounds
low_I0_1=str2double(get(handles.low_I0_1,'String'));
low_Xi_1=str2double(get(handles.low_Xi_1,'String'));
low_x0_1=str2double(get(handles.low_x0_1,'String'));
low_I0_2=str2double(get(handles.low_I0_2,'String'));
low_Xi_2=str2double(get(handles.low_Xi_2,'String'));
% Define Upper Bounds
upper_I0_1=str2double(get(handles.upper_I0_1,'String'));
upper_Xi_1=str2double(get(handles.upper_Xi_1,'String'));
upper_x0_1=str2double(get(handles.upper_x0_1,'String'));
upper_I0_2=str2double(get(handles.upper_I0_2,'String'));
upper_Xi_2=str2double(get(handles.upper_Xi_2,'String'));

% Put bounds into structure
bounds.sp1=[start_I0_1,start_Xi_1,start_x0_1];
bounds.sp2=[start_I0_1,start_I0_2,start_Xi_1,start_Xi_2,...
    start_x0_1];
bounds.low1=[low_I0_1,low_Xi_1,low_x0_1];
bounds.low2=[low_I0_1,low_I0_2,low_Xi_1,low_Xi_2,low_x0_1];
```

```
bounds.up1=[upper_I0_1,upper_Xi_1,upper_x0_1];
bounds.up2=[upper_I0_1,upper_I0_2,upper_Xi_1,upper_Xi_2,...
    upper_x0_1];

warning off
% Excecute Lfit
Lfit_DA_v2c(file,cellrange,start_bimodal,att_factor,attrange,...
    corr_range,bounds,plots,force_save,ccd_cut,make_movie,...
    recursive,fixed_Xi_spec,slope_bkg);


% Button Callbacks from here down

function file_Callback(hObject, eventdata, handles)

function file_CreateFcn(hObject, eventdata, handles)

if ispc && isequal(get(hObject,'BackgroundColor'),...
        get(0,'defaultUicontrolBackgroundColor'))
    set(hObject,'BackgroundColor','white');
end

function cellrange_Callback(hObject, eventdata, handles)

function cellrange_CreateFcn(hObject, eventdata, handles)
if ispc && isequal(get(hObject,'BackgroundColor'),...
        get(0,'defaultUicontrolBackgroundColor'))
    set(hObject,'BackgroundColor','white');
end

function start_bimodal_Callback(hObject, eventdata, handles)

function start_bimodal_CreateFcn(hObject, eventdata, handles)
if ispc && isequal(get(hObject,'BackgroundColor'),...
        get(0,'defaultUicontrolBackgroundColor'))
    set(hObject,'BackgroundColor','white');
end

function edit25_Callback(hObject, eventdata, handles)

function edit25_CreateFcn(hObject, eventdata, handles)
if ispc && isequal(get(hObject,'BackgroundColor'),...
        get(0,'defaultUicontrolBackgroundColor'))
    set(hObject,'BackgroundColor','white');
```

```
end

function att_factor_Callback(hObject, eventdata, handles)

function att_factor_CreateFcn(hObject, eventdata, handles)
if ispc && isequal(get(hObject,'BackgroundColor'),...
        get(0,'defaultUicontrolBackgroundColor'))
    set(hObject,'BackgroundColor','white');
end

function ccd_cut_Callback(hObject, eventdata, handles)

function ccd_cut_CreateFcn(hObject, eventdata, handles)
if ispc && isequal(get(hObject,'BackgroundColor'),...
        get(0,'defaultUicontrolBackgroundColor'))
    set(hObject,'BackgroundColor','white');
end

function force_save_old_Callback(hObject, eventdata, handles)

function force_save_old_CreateFcn(hObject, eventdata, handles)
if ispc && isequal(get(hObject,'BackgroundColor'),...
        get(0,'defaultUicontrolBackgroundColor'))
    set(hObject,'BackgroundColor','white');
end

function plots_Callback(hObject, eventdata, handles)

function plots_CreateFcn(hObject, eventdata, handles)
if ispc && isequal(get(hObject,'BackgroundColor'),...
        get(0,'defaultUicontrolBackgroundColor'))
    set(hObject,'BackgroundColor','white');
end

function make_movie_Callback(hObject, eventdata, handles)

function make_movie_CreateFcn(hObject, eventdata, handles)
if ispc && isequal(get(hObject,'BackgroundColor'),...
        get(0,'defaultUicontrolBackgroundColor'))
    set(hObject,'BackgroundColor','white');
end

function recursive_Callback(hObject, eventdata, handles)
```

```
function recursive_CreateFcn(hObject, eventdata, handles)
if ispc && isequal(get(hObject,'BackgroundColor'),...
        get(0,'defaultUicontrolBackgroundColor'))
    set(hObject,'BackgroundColor','white');
end

function fixed_Xi_spec_Callback(hObject, eventdata, handles)

function fixed_Xi_spec_CreateFcn(hObject, eventdata, handles)
if ispc && isequal(get(hObject,'BackgroundColor'),...
        get(0,'defaultUicontrolBackgroundColor'))
    set(hObject,'BackgroundColor','white');
end

function slope_bkg_Callback(hObject, eventdata, handles)

function slope_bkg_CreateFcn(hObject, eventdata, handles)
if ispc && isequal(get(hObject,'BackgroundColor'),...
        get(0,'defaultUicontrolBackgroundColor'))
    set(hObject,'BackgroundColor','white');
end

function start_Xi_1_Callback(hObject, eventdata, handles)

function start_Xi_1_CreateFcn(hObject, eventdata, handles)
if ispc && isequal(get(hObject,'BackgroundColor'),...
        get(0,'defaultUicontrolBackgroundColor'))
    set(hObject,'BackgroundColor','white');
end

function start_I0_1_Callback(hObject, eventdata, handles)

function start_I0_1_CreateFcn(hObject, eventdata, handles)
if ispc && isequal(get(hObject,'BackgroundColor'),...
        get(0,'defaultUicontrolBackgroundColor'))
    set(hObject,'BackgroundColor','white');
end

function start_x0_1_Callback(hObject, eventdata, handles)

function start_x0_1_CreateFcn(hObject, eventdata, handles)
if ispc && isequal(get(hObject,'BackgroundColor'),...
        get(0,'defaultUicontrolBackgroundColor'))
    set(hObject,'BackgroundColor','white');
```

```
end

function start_Xi_2_Callback(hObject, eventdata, handles)

function start_Xi_2_CreateFcn(hObject, eventdata, handles)
if ispc && isequal(get(hObject,'BackgroundColor'),...
        get(0,'defaultUicontrolBackgroundColor'))
    set(hObject,'BackgroundColor','white');
end

function start_I0_2_Callback(hObject, eventdata, handles)

function start_I0_2_CreateFcn(hObject, eventdata, handles)
if ispc && isequal(get(hObject,'BackgroundColor'),...
        get(0,'defaultUicontrolBackgroundColor'))
    set(hObject,'BackgroundColor','white');
end

function start_x0_2_Callback(hObject, eventdata, handles)

function start_x0_2_CreateFcn(hObject, eventdata, handles)
if ispc && isequal(get(hObject,'BackgroundColor'),...
        get(0,'defaultUicontrolBackgroundColor'))
    set(hObject,'BackgroundColor','white');
end

function low_Xi_1_Callback(hObject, eventdata, handles)

function low_Xi_1_CreateFcn(hObject, eventdata, handles)
if ispc && isequal(get(hObject,'BackgroundColor'),...
        get(0,'defaultUicontrolBackgroundColor'))
    set(hObject,'BackgroundColor','white');
end

function low_I0_1_Callback(hObject, eventdata, handles)

function low_I0_1_CreateFcn(hObject, eventdata, handles)
if ispc && isequal(get(hObject,'BackgroundColor'),...
        get(0,'defaultUicontrolBackgroundColor'))
    set(hObject,'BackgroundColor','white');
end

function low_x0_1_Callback(hObject, eventdata, handles)
```

```
function low_x0_1_CreateFcn(hObject, eventdata, handles)
if ispc && isequal(get(hObject,'BackgroundColor'),...
        get(0,'defaultUicontrolBackgroundColor'))
    set(hObject,'BackgroundColor','white');
end

function low_Xi_2_Callback(hObject, eventdata, handles)

function low_Xi_2_CreateFcn(hObject, eventdata, handles)
if ispc && isequal(get(hObject,'BackgroundColor'),...
        get(0,'defaultUicontrolBackgroundColor'))
    set(hObject,'BackgroundColor','white');
end

function low_I0_2_Callback(hObject, eventdata, handles)

function low_I0_2_CreateFcn(hObject, eventdata, handles)

if ispc && isequal(get(hObject,'BackgroundColor'),...
        get(0,'defaultUicontrolBackgroundColor'))
    set(hObject,'BackgroundColor','white');
end

function low_x0_2_Callback(hObject, eventdata, handles)

function low_x0_2_CreateFcn(hObject, eventdata, handles)

if ispc && isequal(get(hObject,'BackgroundColor'),...
        get(0,'defaultUicontrolBackgroundColor'))
    set(hObject,'BackgroundColor','white');
end

function upper_Xi_1_Callback(hObject, eventdata, handles)

function upper_Xi_1_CreateFcn(hObject, eventdata, handles)

if ispc && isequal(get(hObject,'BackgroundColor'),...
        get(0,'defaultUicontrolBackgroundColor'))
    set(hObject,'BackgroundColor','white');
end

function upper_I0_1_Callback(hObject, eventdata, handles)

function upper_I0_1_CreateFcn(hObject, eventdata, handles)
```

```
if ispc && isequal(get(hObject,'BackgroundColor'),...
        get(0,'defaultUicontrolBackgroundColor'))
    set(hObject,'BackgroundColor','white');
end

function upper_x0_1_Callback(hObject, eventdata, handles)

function upper_x0_1_CreateFcn(hObject, eventdata, handles)

if ispc && isequal(get(hObject,'BackgroundColor'),...
        get(0,'defaultUicontrolBackgroundColor'))
    set(hObject,'BackgroundColor','white');
end

function upper_Xi_2_Callback(hObject, eventdata, handles)

function upper_Xi_2_CreateFcn(hObject, eventdata, handles)
if ispc && isequal(get(hObject,'BackgroundColor'),...
        get(0,'defaultUicontrolBackgroundColor'))
    set(hObject,'BackgroundColor','white');
end

function upper_I0_2_Callback(hObject, eventdata, handles)

function upper_I0_2_CreateFcn(hObject, eventdata, handles)
if ispc && isequal(get(hObject,'BackgroundColor'),...
        get(0,'defaultUicontrolBackgroundColor'))
    set(hObject,'BackgroundColor','white');
end

function upper_x0_2_Callback(hObject, eventdata, handles)

function upper_x0_2_CreateFcn(hObject, eventdata, handles)
if ispc && isequal(get(hObject,'BackgroundColor'),...
        get(0,'defaultUicontrolBackgroundColor'))
    set(hObject,'BackgroundColor','white');
end

function openfile_Callback(hObject, eventdata, handles)
path(pwd,path)
[filename,pathname]=uigetfile;
if filename==0
    return
```

```
end
path(pathname,path)
if pathname~=0
    cd(pathname);
    set(handles.save_location,'String',pathname)
    set(handles.openfile,'String',filename)
end

function save_file_Callback(hObject, eventdata, handles)


function change_save_location_Callback(hObject, eventdata,...
    handles)
pathname2=uigetdir;
if pathname2 ~=0
    cd(pathname2)
    set(handles.save_location,'String',pathname2)
end

function save_location_Callback(hObject, eventdata, handles)

function save_location_CreateFcn(hObject, eventdata, handles)

% Hint: edit controls usually have a white background on Windows.
%       See ISPC and COMPUTER.
if ispc && isequal(get(hObject,'BackgroundColor'),...
        get(0,'defaultUicontrolBackgroundColor'))
    set(hObject,'BackgroundColor','white');
end


function edit35_Callback(hObject, eventdata, handles)


function edit35_CreateFcn(hObject, eventdata, handles)

% Hint: edit controls usually have a white background on Windows.
%       See ISPC and COMPUTER.
if ispc && isequal(get(hObject,'BackgroundColor'),...
        get(0,'defaultUicontrolBackgroundColor'))
    set(hObject,'BackgroundColor','white');
end
```

BIBLIOGRAPHY

[1] A. Ohtomo and H. Y. Hwang. A high-mobility electron gas at the $LaAlO_3/SrTiO_3$ heterointerface. *Nature*, 427(6973):423–426, 2004.

[2] Francis S. Galasso. *Structure, properties, and preparation of perovskite-type compounds.* Pergamon Press, Oxford, New York, 1969.

[3] Helen D Megaw. Crystal structure of double oxides of the perovskite type. *Proceedings of the Physical Society*, 58(2):133, 1946.

[4] Elbio Dagotto, Takashi Hotta, and Adriana Moreo. Colossal magnetoresistant materials: the key role of phase separation. *Physics Reports*, 344(1-3):1 – 153, 2001.

[5] Hiroshi Maeda, Yoshiaki Tanaka, Masao Fukutomi, and Toshihisa Asano. A new high-T_c oxide superconductor without a rare earth element. *Japanese Journal of Applied Physics*, 27(Part 2, No. 2):L209–L210, 1988.

[6] M. K. Wu, J. R. Ashburn, C. J. Torng, P. H. Hor, R. L. Meng, L. Gao, Z. J. Huang, Y. Q. Wang, and C. W. Chu. Superconductivity at 93 K in a new mixed-phase Y-Ba-Cu-O compound system at ambient pressure. *Physical Review Letters*, 58(9):908–910, 1987.

[7] R. von Helmolt, J. Wecker, B. Holzapfel, L. Schultz, and K. Samwer. Giant negative magnetoresistance in perovskitelike $La_{2/3}Ba_{1/3}MnO_x$ ferromagnetic films. *Physical Review Letters*, 71(14):2331–2333, 1993.

[8] H. Y. Hwang, S-W. Cheong, P. G. Radaelli, M. Marezio, and B. Batlogg. Lattice effects on the magnetoresistance in doped $LaMnO_3$. *Physical Review Letters*, 75(5):914–917, 1995.

[9] P. Schiffer, A. P. Ramirez, W. Bao, and S-W. Cheong. Low temperature magnetoresistance and the magnetic phase diagram of $La_{1-x}Ca_xMnO_3$. *Physical Review Letters*, 75(18):3336–3339, 1995.

[10] R. E. Cohen. Origin of ferroelectricity in perovskite oxides. *Nature*, 358(6382):136–138, 1992.

[11] James F. Scott and Carlos A. Paz de Araujo. Ferroelectric memories. *Science*, 246(4936):1400–1405, 1989.

[12] G. H. Jonker and J. H. Van Santen. Ferromagnetic compounds of manganese with perovskite structure. *Physica*, 16(3):337 – 349, 1950.

[13] Clarence Zener. Interaction between the *d*-shells in the transition metals. ii. ferromagnetic compounds of manganese with perovskite structure. *Physical Review*, 82(3):403–405, 1951.

[14] W. Eerenstein, N. D. Mathur, and J. F. Scott. Multiferroic and magnetoelectric materials. *Nature*, 442(7104):759–765, 2006.

[15] Craig J. Fennie and Karin M. Rabe. Magnetic and electric phase control in epitaxial $EuTiO_3$ from first principles. *Physical Review Letters*, 97(26):267602, 2006.

[16] T. Kimura, T. Goto, H. Shintani, K. Ishizaka, T. Arima, and Y. Tokura. Magnetic control of ferroelectric polarization. *Nature*, 426(6962):55–58, 2003.

[17] S. Thiel, G. Hammerl, A. Schmehl, C. W. Schneider, and J. Mannhart. Tunable Quasi-Two-Dimensional Electron Gases in Oxide Heterostructures. *Science*, 313(5795):1942–1945, 2006.

[18] A. Brinkman, M. Huijben, M. van Zalk, J. Huijben, U. Zeitler, J. C. Maan, W. G. van der Wiel, G. Rijnders, D. H. A. Blank, and H. Hilgenkamp. Magnetic effects at the interface between non-magnetic oxides. *Nature Materials*, 6(7):493–496, 2007.

[19] N. Reyren, S. Thiel, A. D. Caviglia, L. Fitting Kourkoutis, G. Hammerl, C. Richter, C. W. Schneider, T. Kopp, A.-S. Ruetschi, D. Jaccard, M. Gabay, D. A. Muller, J.-M. Triscone, and J. Mannhart. Superconducting Interfaces Between Insulating Oxides. *Science*, 317(5842):1196–1199, 2007.

[20] C. Cen, S. Thiel, G. Hammerl, C. W. Schneider, K. E. Andersen, C. S. Hellberg, J. Mannhart, and J. Levy. Nanoscale control of an interfacial metal-insulator transition at room temperature. *Nat Mater*, 7(4):298–302, 04 2008.

[21] Cheng Cen, Stefan Thiel, Jochen Mannhart, and Jeremy Levy. Oxide nanoelectronics on demand. *Science*, 323(5917):1026–1030, 2009.

[22] Dave H. A. Blank and Guus Rijnders. Nanoelectronics: Oxides offer the write stuff. *Nat Nano*, 4(5):279–280, 05 2009.

[23] Subhash C. Singhal and Kevin Kendall. *High-temperature solid oxide fuel cells: fundamentals, design, and applications*. Elsevier Advanced Technology, New York, 2003.

[24] S. C. Singhal. Advances in solid oxide fuel cell technology. *Solid State Ionics*, 135(1-4):305–313, 11 2000.

[25] Brian C. H. Steele and Angelika Heinzel. Materials for fuel-cell technologies. *Nature*, 414(6861):345–352, 2001.

[26] Douglas B. Chrisey and G. K. Hubler. *Pulsed laser deposition of thin films*. J. Wiley, New York, 1994.

[27] Aaron Fleet. *Time resolved X-ray scattering during strontium titanate homoepitaxy by pulsed laser deposition*. PhD thesis, Cornell University, Ithaca, NY, 2005.

[28] D. H. A. Blank, G. Koster, G. Rijnders, E. van Setten, P. Slycke, and H. Rogalla. Imposed layer-by-layer growth by pulsed laser interval deposition. *Applied Physics A*, 69:S17–S22, 1999.

[29] M. Lippmaa, N. Nakagawa, M. Kawasaki, S. Ohashi, and H. Koinuma. Growth mode mapping of $SrTiO_3$ epitaxy. *Applied Physics Letters*, 76(17):2439–2441, 2000.

[30] Andrew Zangwill. *Physics At Surfaces*. Cambridge University Press, Cambridge [Cambridgeshire]; New York, 1988.

[31] J. Als-Nielsen and Des. McMorrow. *Elements of modern X-ray physics*. Wiley, New York, 2001.

[32] J.W. Evans, P.A. Thiel, and M.C. Bartelt. Morphological evolution during epitaxial thin film growth: Formation of 2D islands and 3D mounds. *Surface Science Reports*, 61(1-2):1 – 128, 2006.

[33] Michael J. Aziz. Film growth mechanisms in pulsed laser deposition. *Applied Physics A: Materials Science & Processing*, 93(3):579–587, 2008.

[34] A. Fleet, D. Dale, Y. Suzuki, and J. D. Brock. Observed effects of a changing step-edge density on thin-film growth dynamics. *Physical Review Letters*, 94(3):36102, 2005.

[35] Aaron Fleet, Darren Dale, A. R. Woll, Y. Suzuki, and J. D. Brock. Multiple time scales in diffraction measurements of diffusive surface relaxation. *Physical Review Letters*, 96(5):055508, 2006.

[36] P. O. Jubert, O. Fruchart, and C. Meyer. Nucleation and surface diffusion in pulsed laser deposition of Fe on Mo(110). *Surface Science*, 522(1-3):8 – 16, 2003.

[37] M. Lippmaa, M. Kawasaki, A. Ohtomo, T. Sato, M. Iwatsuki, and H. Koinuma. Observation of $SrTiO_3$ step edge dynamics by real-time high-temperature STM. *Applied Surface Science*, 130-132:582 – 586, 1998.

[38] J. Tischler, G. Eres, B. Larson, C. M. Rouleau, P. Zschack, and D. H. Lowndes. Nonequilibrium interlayer transport in pulsed laser deposition. *Physical Review Letters*, 96(22):226104, 2006.

[39] P. R. Willmott, R. Herger, C. M. Schlepütz, D. Martoccia, and B. D. Patterson. Energetic surface smoothing of complex metal-oxide thin films. *Physical Review Letters*, 96(17):176102, 2006.

[40] A. Cuenat, H.B. George, K.-C. Chang, J.M. Blakely, and M.J. Aziz. Lateral templating for guided self-organization of sputter morphologies. *Advanced Materials*, 17(23):2845–2849, 2005.

[41] Masashi Kawasaki, Kazuhiro Takahashi, Tatsuro Maeda, Ryuta Tsuchiya, Makoto Shinohara, Osamu Ishiyama, Takuzo Yonezawa, Mamoru Yoshimoto, and Hideomi Koinuma. Atomic control of the $SrTiO_3$ crystal surface. *Science*, 266(5190):1540–1542, 1994.

[42] Gertjan Koster, Boike L. Kropman, Guus J. H. M. Rijnders, Dave H. A. Blank, and Horst Rogalla. Quasi-ideal strontium titanate crystal surfaces through formation of strontium hydroxide. *Applied Physics Letters*, 73(20):2920–2922, 1998.

[43] I. K. Robinson and D. J. Tweet. Surface x-ray-diffraction. *Reports on Progress in Physics*, 55(5), 1992.

[44] S. J. L. Billinge and M. F. Thorpe. *Local structure from diffraction*. Plenum Press, New York, 1998.

[45] Michael Kotlarchyk and Sow-Hsin Chen. Analysis of small angle neutron scattering spectra from polydisperse interacting colloids. *The Journal of Chemical Physics*, 79(5):2461–2469, 1983.

[46] J. D. Brock, J. D. Ferguson, and A. R. Woll. X-ray scattering studies of the surface structure of complex oxide films during layer-by-layer growth via pulsed laser deposition. *Metallurgical and Materials Transactions A*, 41(5):1162–1166, 2010.

[47] P. Hahn, J. Clabes, and M. Henzler. Leed-investigations and work-function measurements of the first stages of epitaxy of tungsten on tungsten (110). *Journal of Applied Physics*, 51(4):2079–2084, 1980.

[48] E. Dulot, B. Kierren, and D. Malterre. Determination of kinetic parameters in layer-by-layer growth from RHEED profile analysis. *Thin Solid Films*, 423(1):64–69, 2003.

[49] H L Marsh, D S Deak, F Silly, A I Kirkland, and M R Castell. Hot STM of nanostructure dynamics on $SrTiO_3$ (001). *Nanotechnology*, 17(14):3543, 2006.

[50] Darren Dale, Aaron Fleet, Y. Suzuki, and J. D. Brock. X-ray scattering from real surfaces: Discrete and continuous components of roughness. *Physical Review B*, 74(8):085419, 2006.

[51] S. K. Sinha, E. B. Sirota, S. Garoff, and H. B. Stanley. X-ray and neutron scattering from rough surfaces. *Physical Review B*, 38(4):2297–2311, 1988.

[52] Darren Dale, Y Suzuki, and J D Brock. In situ x-ray reflectivity studies of dynamics and morphology during heteroepitaxial complex oxide thin film growth. *Journal of Physics: Condensed Matter*, 20(26):264008, 2008.

[53] M.C. Bartelt and J.W. Evans. Nucleation and growth of square islands during deposition: Sizes, coalescence, separations and correlations. *Surface Science*, 298(2-3):421 – 431, 1993.

[54] Harald Brune, G. Steven Bales, Joachim Jacobsen, Corrado Boragno, and Klaus Kern. Measuring surface diffusion from nucleation island densities. *Physical Review B*, 60(8):5991–6006, 1999.

[55] P. Debye, Jr. H. R. Anderson, and H. Brumberger. Scattering by an inhomogeneous solid. II. the correlation function and its application. *Journal of Applied Physics*, 28(6):679–683, 1957.

[56] Ronald N. Bracewell. *The Fourier transform and its applications*. McGraw-Hill, New York, 1965.

[57] N. C. Bartelt, W. Theis, and R. M. Tromp. Ostwald ripening of two-dimensional islands on Si(001). *Physical Review B*, 54(16):11741–11751, 1996.

[58] J. M. Wen, J. W. Evans, M. C. Bartelt, J. W. Burnett, and P. A. Thiel. Coarsening mechanisms in a metal film: From cluster diffusion to vacancy ripening. *Physical Review Letters*, 76(4):652–655, 1996.

[59] S. K. Sinha, Y. P. Feng, C. A. Melendres, D. D. Lee, T. P. Russell, S. K. Satija, E. B. Sirota, and M. K. Sanyal. Off-specular x-ray scattering studies of the morphology of thin films. *Physica A: Statistical and Theoretical Physics*, 231(1-3):99 – 110, 1996.

[60] R Gomer. Diffusion of adsorbates on metal surfaces. *Reports on Progress in Physics*, 53(7):917, 1990.

[61] Joachim Jacobsen, B. H. Cooper, and James P. Sethna. Simulations of energetic beam deposition: From picoseconds to seconds. *Physical Review B*, 58(23):15847–15865, 1998.

[62] Joshua M. Pomeroy, Joachim Jacobsen, Colin C. Hill, Barbara H. Cooper, and James P. Sethna. Kinetic monte carlo–molecular dynamics investigations of hyperthermal copper deposition on Cu(111). *Physical Review B*, 66(23):235412, 2002.

[63] Efthimios Kaxiras and Jonah Erlebacher. Adatom diffusion by orchestrated exchange on semiconductor surfaces. *Physical Review Letters*, 72(11):1714–1717, 1994.

[64] J. Mannhart and D. G. Schlom. Oxide Interfaces–An Opportunity for Electronics. *Science*, 327(5973):1607–1611, 2010.

[65] J. D. Ferguson, G. Arikan, D. S. Dale, A. R. Woll, and J. D. Brock. Measurements of surface diffusivity and coarsening during pulsed laser deposition. *Physical Review Letters*, 103(25):256103, 2009.

[66] C. Merckling, M. El-Kazzi, G. Delhaye, V. Favre-Nicolin, Y. Robach, M. Gendry, G. Grenet, G. Saint-Girons, and G. Hollinger. Strain relaxation and critical thickness for epitaxial $LaAlO_3$ thin films grown on $SrTiO_3(001)$ substrates by molecular beam epitaxy. *Journal of Crystal Growth*, 306(1):47 – 51, 2007.

[67] Heinz Kiessig. Bemerkungen zu einer arbeit von h. w. edwards ber totalreflexion von rntgenstrahlen (comments on a work from H. W. Edwards, "On total reflection of X-rays."). *Annalen Der Physik*, 403(5), 1931.

[68] Vladimir M. Kaganer, Bernd Jenichen, Roman Shayduk, Wolfgang Braun, and Henning Riechert. Kinetic optimum of volmer-weber growth. *Physical Review Letters*, 102(1):016103, 2009.

[69] J. B. Goodenough. Oxide-ion electrolytes. *Annual Review of Materials Research*, 33, 2003.

[70] Zongping Shao and Sossina M. Haile. A high-performance cathode for the next generation of solid-oxide fuel cells. *Nature*, 431(7005):170–173, 2004.

[71] Stephen J. Skinner. Recent advances in perovskite-type materials for solid oxide fuel cell cathodes. *International Journal of Inorganic Materials*, 3(2):113 – 121, 2001.

[72] J. B. Goodenough, J. E. Ruiz-Diaz, and Y. S. Zhen. Oxide-ion conduction in $Ba_2In_2O_5$ and $Ba_3In_2MO_8$ (M=Ce, Hf, or Zr). *Solid State Ionics*, 44(1-2), 1990.

[73] Kurt R. Kendall, Carlos Navas, Julie K. Thomas, and Hans-Conrad zur Loye. Recent developments in perovskite-based oxide ion conductors. *Solid State Ionics*, 82(3-4), 1995.

[74] B. C. H. Steele. Oxygen ion conductors and their technological applications. *Materials Science and Engineering: B*, 13(2), 1992.

[75] R. Feidenhansl. Surface-structure determination by x-ray-diffraction. *Surface Science Reports*, 10(3), 1989.

[76] J. H. Neave, B. A. Joyce, P. J. Dobson, and N. Norton. Dynamics of film growth of GaAs by MBE from RHEED observations. *Applied Physics A: Materials Science & Processing*, 31(1), 1983.

[77] A. Ohtomo and H. Y. Hwang. Growth mode control of the free carrier density in $SrTiO_{3-\delta}$ films. *Journal of Applied Physics*, 102(8):083704, 2007.

[78] David A. Muller, Naoyuki Nakagawa, Akira Ohtomo, John L. Grazul, and Harold Y. Hwang. Atomic-scale imaging of nanoengineered oxygen vacancy profiles in $SrTiO_3$. *Nature*, 430(7000), 2004.

[79] K. S. Takahashi and H. Y. Hwang. Carrier doping in anatase TiO_2 film by perovskite overlayer deposition. *Applied Physics Letters*, 93(8):082112, 2008.

[80] Dmitri O. Klenov, Wolfgang Donner, Brendan Foran, and Susanne Stemmer. Impact of stress on oxygen vacancy ordering in epitaxial $(La_{0.5}Sr_{0.5})CoO_{3-\delta}$ thin films. *Applied Physics Letters*, 82(20), 2003.

[81] M. D. Rossell, O. I. Lebedev, G. Van Tendeloo, N. Hayashi, T. Terashima, and M. Takano. Structure of epitaxial $Ca_2Fe_2O_5$ films deposited on different perovskite-type substrates. *Journal of Applied Physics*, 95(9), 2004.

[82] Thomas G. Parsons, Hans D'Hondt, Joke Hadermann, and Michael A. Hayward. Synthesis and structural characterization of $La_{1-x}A_xMnO_2.5$ (A = Ba, Sr, Ca) phases: Mapping the variants of the brownmillerite structure. *Chemistry of Materials*, 21(22), 2009.

[83] E. F. Bertaut, P. Blum, and A. Sagnieres. Structure du ferrite bicalcuque et de la brownmillertie (structure of calcium ferrite and of brownmillerite). *Acta Crystallographica*, 12(2), 1959.

[84] W. Braun, V. M. Kaganer, B. Jenichen, and K. H. Ploog. Non-ostwald coarsening of the gaas(001) surface. *Physical Review B*, 69(16):–, 2004.

[85] H. J. Ernst, F. Fabre, and J. Lapujoulade. Observation of dynamic scaling in spinodal decomposition in 2 dimensions. *Physical Review Letters*, 69(3):458–461, 1992.

[86] F. Haußer and A. Voigt. Ostwald ripening of two-dimensional homoepitaxial islands. *Physical Review B*, 72(3):035437, 2005.

[87] P. W. Voorhees. The theory of ostwald ripening. *Journal of Statistical Physics*, 38(1-2):231–252, 1985.

[88] Yoshinori Tokura and Harold Y. Hwang. Condensed-matter physics: Complex oxides on fire. *Nat Mater*, 7(9):694–695, 09 2008.

[89] V. M. Kaganer, W. Braun, B. Jenichen, and K. H. Ploog. Two stages of post-growth recovery in molecular beam epitaxy: a surface x-ray diffraction study. *Surface Science*, 560(1-3):88–102, 2004.

[90] A. Ohtomo, D. A. Muller, J. L. Grazul, and H. Y. Hwang. Artificial charge-modulationin atomic-scale perovskite titanate superlattices. *Nature*, 419(6905):378–380, 2002.

[91] J. W. Reiner, F. J. Walker, and C. H. Ahn. Materials science: Atomically engineered oxide interfaces. *Science*, 323(5917):1018–1019, 2009.

[92] L. Ranno, A. Llobet, R. Tiron, and E. Favre-Nicolin. Strain-induced magnetic anisotropy in epitaxial manganite films. *Applied Surface Science*, 188(1-2), 2002.

[93] Joachim Rosler, H. Harders, and M. Baker. *Mechanical behaviour of engineering materials metals, ceramics, polymers, and composites*. Springer, Berlin; New York, 2007.

[94] M. Zhang, X. L. Ma, and D. X. Li. Crystallographic study of the rhombohedral-oriented domains in a la0.7sr0.3mno3 film. *Philosophical Magazine*, 85(15), 2005.

[95] Philippe Lacorre, Francois Goutenoire, Odile Bohnke, Richard Retoux, and Yvon Laligant. Designing fast oxide-ion conductors based on $La_2Mo_2O_9$. *Nature*, 404(6780), 2000.

[96] John B. Goodenough. Ceramic solid electrolytes. *Solid State Ionics*, 94(1-4), 1997.

[97] P Berastegui, S Hull, FJ Garcia-Garcia, and SG Eriksson. The crystal structures, microstructure and ionic conductivity of $Ba_2In_2O_5$ and $Ba(In_xZr_{1-x})O_{3-x/2}$. *Journal of Solid State Chemistry*, 164(1), 2002.

[98] Thomas Courtney. *Mechanical Behavior of Materials*. Waveland Press, Long Grove, IL, 2000.

[99] Alexey Kalabukhov, Robert Gunnarsson, Johan Börjesson, Eva Olsson, Tord Claeson, and Dag Winkler. Effect of oxygen vacancies in the $SrTiO_3$ substrate on the electrical properties of the $LaAlO_3/SrTiO_3$ interface. *Physical Review B*, 75(12):121404, 2007.

[100] Naoyuki Nakagawa, Harold Y. Hwang, and David A. Muller. Why some interfaces cannot be sharp. *Nature Materials*, 5(3):204–209, 2006.

[101] P. R. Willmott, S. A. Pauli, R. Herger, C. M. Schlepütz, D. Martoccia, B. D. Patterson, B. Delley, R. Clarke, D. Kumah, C. Cionca, and Y. Yacoby. Structural basis for the conducting interface between $LaAlO_3$ and $SrTiO_3$. *Physical Review Letters*, 99(15):155502, 2007.